Durham E-Theses

Implementation of trace element behaviour in the numerical modelling of magmatic processes

CORNET, JULIEN,RENE,DENIS

How to cite:

Use policy

Implementation of trace element behaviour in the numerical modelling of magmatic processes

Julien Cornet

Supervisors:

Dr Jeroen van Hunen

Dr Pierre Bouilhol

Dr Nicolas Riel

A dissertation presented for the degree of

Master by Research

June 2017

Department of Earth Sciences

University of Durham

England

"Nature is a vast tablet, inscribed with signs, each of which has its own significancy, and becomes poetry in the mind when read; and geology is simply the key by which myriads of these signs, hitherto indecipherable, can be unlocked and perused, and thus a new province added to the poetical domain."

Hugh Miller

Lecture Third, collected in Popular Geology: A series of Lectures Read Before the Philosophical Institution of Edinburgh, with Descriptive Sketches from a Geologist's Portfolio (1859), 131

Implementation of trace element behaviour in the numerical modelling of magmatic processes

Julien Cornet

Abstract

Trace element analysis of rocks and minerals can provide valuable insight in the petrogenesis of the crust and therefore may offer fundamental constraints into geodynamical processes. But crustal building involves a multitude of magmatic/metamorphic processes, and the trace element behaviour during each of these processes is complex, which makes the interpretation of trace element composition of the final crustal product non-unique. Therefore, a thorough investigation of trace element systematics between mineral and melt is required to trace the implication of important stable phases in crustal building processes. This can be given using forward numerical modelling and trace element modelling. However, while numerical models simulating thermodynamic reactions are available, a numerical tool for the prediction of trace element behaviour is missing. Such tool would be of key interest to capture the subtle exchanges during magmatic reactions.

Therefore, this thesis presents the building of a novel numerical tool able to predict the variation in trace element partition coefficients between 6 mafic minerals and melt (e.g., garnet, olivine, pyroxene, plagioclase and amphibole). To develop such tool, the state-of-the-art predictive models available in the literature are compiled. These predictive models are of two different kinds. First, the lattice strain model (LSM) is based on the energy exchange of trace elements between mineral and melt. Second, multiple regressions analyses are based on the most accurate fit against various chemical/physical parameters and natural data. In addition, this thesis builds predictive models by applying statistical regressions on large dataset of trace element partition coefficients in the case no models are available in the literature.

While the stand-alone version of this tool reproduces well the experimental data, coupling with the numerical code Perple_X, which calculates stable mineral assemblages using Gibbs free energy minimization, allows calculation of a full P-T catalogue of trace element behaviour in the partial melting of an amphibolite. The catalogue gives insights in the assimilation processes in a lower crust in arc settings. This coupling offers a new perspective for future, more complex coupling with numerical codes of melt genesis, transfer and emplacement.

List of Figures

List of Tables

List of Abbreviations and important data

Element Abbreviation	Element Name	Ionic Radius CN8 (Å)	Ionic Radius CN6 (Å)	Element Abbreviation	Element Name	Ionic Radius CN8 (Å)	Ionic Radius CN6 (Å)
Cs	Cesium	1.74	1.67	Dy	Dysprosium	1.027	0.912
Rb	Rubidium	1.61	1.52	Y	Yttrium	1.019	0.9
K	Potassium	1.15	1.38	Ho	Holmium	1.015	0.901
Na	Sodium	1.18	1.02	Er	Erbium	1.004	0.89
Ba	Barium	1.42	1.35	Tm	Thulium	0.994	0.88
Sr	Strontium	1.26	1.18	Yb	Ytterbium	0.985	0.868
Ca	Calcium	1.12	1	Lu	Lutetium	0.977	0.861
Mg	Magnesium	0.89	0.72	Sc	Scandium	0.870	0.745
La	Lanthanum	1.16	1.032	Ti	Titanium	0.74	0.605
Ce	Cerium	1.143	1.01	Si	Silicon	0.26 (CN4)	n/a
Pr	Praesodynium	1.126	0.99	Hf	Hafnium	0.83	0.71
Nd	Neodymium	1.09	0.983	Zr	Zirconium	0.84	0.72
Sm	Samarium	1.079	0.958	U	Uranium	1	0.89
Eu	Europium	1.066	0.947	Th	Thorium	1.05	0.94
Gd	Gadolinium	1.053	0.938	Ta	Tantalum	0.7295	0.6295
Tb	Terbium	1.04	0.923	Nb	Niobium	0.74	0.64

Acknowledgments

always, always make me believe in myself. I would also thank Vili Grigorova, my pal. We were both the baby masters in a research group made of genius. I always felt better to have her accompliced look during the meetings when things were too complicated. Above that, I would thank her for always been there for me for my personal or professional problems (and also for the numerous treats!). I am also thankful for having shared with experience with other pals: Giacomo, Ines, Tom, Jack, Ali, Aylin that gave me every day joy. A special thanks for Erin Scott who invited me on her field work project in Chile. Erin is also a great scientist and I look forward to working with her again.

I am also thankful to my family who always understood my needs and let me do what I like the most.

Finally, life is easier with friends and family but it is even easier with the blind support of a partner. For that, I am deeply thankful to Ilaria Gaiani. She has been a pillar ever since the beginning on which I have relied to grow both personally and professionally. She understands everything of what I am and she literally projects me toward success that I hope will come soon.

1. Introduction

Trace elements are widely used to understand magmatic processes as they record the mechanisms of melt formation and evolution during partial melting and crystallization. They constrain the conditions by which a melt was formed, transferred and emplaced in the crust, and are also used to infer information about the melt source in many geodynamical environments. As for major elements, trace elements record the magmatic processes, but are much more sensitive to the physico-chemical characteristics of the system considered, hence providing petrologist and geochemist a mean to accurately track Earth processes. However, the complex variability of magmatic reactions often blurs the trace element signature, which makes it difficult to unravel the initial conditions of melt genesis or the conditions in which a melt was transferred and differentiated. In this case, it is necessary to employ a tool able to predict the conditions of melt genesis, melt pathways and the conditions of differentiation in order to have a complete picture of magmatic processes. The use of forward numerical modelling is therefore of great interest. Numerical tools to simulate physical processes like fluid or melt flow (Riel et al, in review, Tirone et al, 2012) can be coupled to numerical tools to predict stable phases, chemical compositions, and other properties (Bouilhol et al, 2011). Thanks to recent advances in the understanding of trace element behaviour (Blundy and Wood, 1994; Wood and Blundy, 1997) and the numerous studies proposing predictive models on this matter (Chapter 3 and reference therein), it is now possible to create a numerical tool of trace element behaviour in magmatic environments. In further studies, this can be implemented in numerical models of melt migration to propose a complete image of magmatic reactions in a complex geodynamical system.

In magmatic environments, there are many parameters that control the behaviour of trace elements and it is the first task of this thesis to list and explore these parameters. First of all, this Chapter 1 introduces and provides general information about trace elements in magmatic processes. Then, it focuses on the parameters controlling trace element behaviour. Finally, this chapter will present the outline and aims of this thesis. Chapter 2 presents the methods used to predict trace element behaviour in magmatic processes, i.e., the lattice strain model and multiple regression analyses. Then, Chapter 3 presents the results for trace element predictive models of partition coefficients that are used in the building of a numerical tool presented and tested in Chapter 4.

1.1 General Background on trace elements behaviour in melting processes

Trace elements are natural elements that can be classified within any period and group in the Mendeleev periodic table. The Goldschmidt classification (Goldschmidt, 1937) stipulates that natural elements are divided in four classes, namely lithophile, siderophile, chalcophile and

atmophile. Atmophile elements are more present in the atmosphere and gas. Chalcophiles (such as Cu, Zn) are preferably bonding with sulphur. For siderophile elements (e.g., Fe, Ni, Ag, Au), the bonds between them and oxygen or sulphur are too weak to form compounds and prefer to stay in their pure state by forming metallic bonds with other siderophile elements. In this study, only lithophile elements will be considered as they are more profoundly involved in crustal and upper mantle processes due to their affinity to form compounds with oxygen. They are also called rock forming elements. Within the lithophile class, trace elements are divided in several sub-groups such as high field strength elements (HFSE: Ta^{5+}, Nb^{5+}, Ti^{4+}, Zr^{4+}, Hf^{4+}), large ions lithophile elements (LILE: Cs^+, Rb^+, K^+, Sr^{2+}, Ba^{2+}), rare earth elements (REE: isovalent series from La^{3+} to Lu^{3+}), actinides (U^{4+}, Th^{4+}) and transition metals (Sc^{3+}, Y^{3+}). Those listed here are the elements used in the study and this does not provide with an exhaustive list of all the lithophile trace elements. As indicated by their name, these trace elements are often found to be at really low concentration in rock samples. From their rarity, high valences and/or large sizes, trace elements have the tendency to favour liquids since they cannot easily enter mineral structures that favour the incorporation of major elements (e.g., Ca, Fe, Mg, Si, Na, Al). They are therefore called refractory or incompatible elements. As an analogue, trace elements can be seen as pentagonal bricks in a wall made of rectangular bricks.

1.2 Trace element in magmatic processes

The understanding of magmatic processes and the geological domain in which they occur is essential to characterize hand samples and to find out the conditions of rock formation. From field to experimental petrographic and geochemical studies, numerous interpretations are done on the way magma evolves from genesis to emplacement. Trace elements have a main role in this understanding and are always used to decipher the complex history of magmatic mechanisms.

1.2.1   An introduction to the magmatic contexts covered by this thesis

In the frame of this thesis that is to present a numerical tool of trace element behaviour in magmatic processes, it is of importance to shortly present the context in which the tool is or could be applicable (cf. Chapter 4 for more detailed explanation).

Earth is a thermodynamic machinery able to bring materials under various pressure and temperature conditions involving complex series of melting/crystallisation events that hugely alter the trace elements evolution (Turcotte and Schubert, 2014). The applicability range of the tool presented thereafter covers most of the mafic magmatic processes in the upper mantle and lower crust. Those magmatic processes are, for example, related to Arc building, MOR as well as the apex of mantle plume.

Subduction zones are thought to be the main site of continental crust production (e.g. Taylor and

McLennan, 1995), through a complex physico-chemical processes (Jagoutz and Kelemen, 2015). Slab devolatilisation fuels mantle wedge melting and the production of primary arc magmas that will construct the arc. Within the uppermost arc mantle and crust, these primary arc magmas will differentiate, inducing large scale processes that ultimately lead to a segregated lower and upper crust of different composition. As they impinge in the arc crust, primary magmas will start their evolution towards more evolved, silicic-rich melts, and interact with the pre-existing lower crust, leading to the formation of a MASH (Melting Assimilation Segregation and Hybridisation) zone (e.g., Hildreth and Morbath, 1988), or hot-zone (Annen et al, 2006), where most melt evolution takes place during their transfer towards higher crustal levels (Bouilhol et al, 2015).

Other geological context is magmatic processes related to the Mid Ocean Ridge processes that creates oceanic crust via partial melting of the upwelling mantle and migration of melts in a narrow concentrated zone at the axis via dunite channels (Kelemen et al, 1995; MacDonald, 1982; Hebert and Montesi, 2010, Lissenberg and McLeod, 2016; Connolly et al, 2009; Lizarralde et al, 2004; Salters and Hart, 1989) Figure 1.1. Also related to mantle dynamics, mantle plumes are important as well since they can destabilize the lower crust and imply intracrustal magmatic processes referred to as hotspot (Smith et al, 2009; Lassiter, 1999; Zhao, 2004).
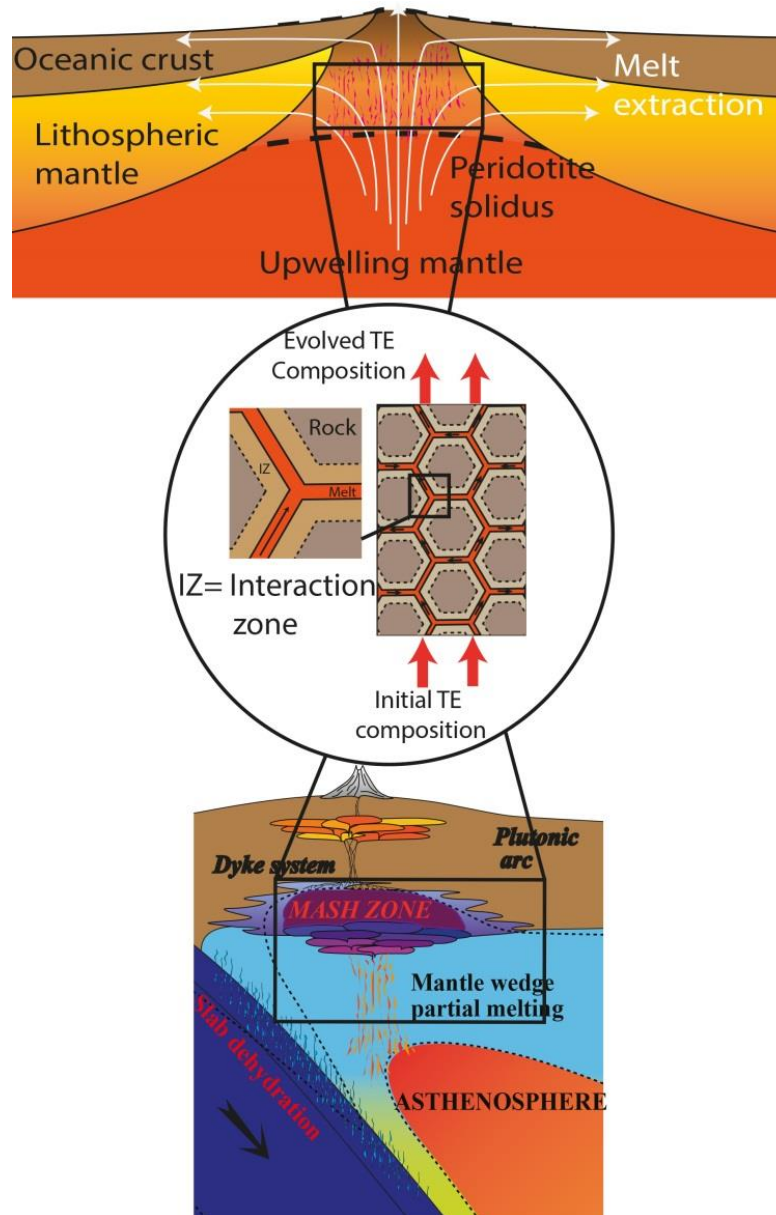
Figure 1-1: *Top and bottom figures: Schematic view of two geologic settings known to play an important role in the evolution of traces elements, mid ocean ridges and subduction zones. Middle figure: Schematic view of magma transfer through a porous media, which represents one magmatic process that greatly affects the distribution of trace elements between solid and melt.*

1.2.2   A brief introduction to magmatic reactions

Magmatic reactions are the mechanisms by which solids and liquids interact in a magmatic environment. This interaction is controlled by the dynamics of melting/crystallisation itself, and depends on the physical forces applied to the system (temperature, pressure, melt influx).

Figure 1.1 displays reactive melt flow (McKenzie, 1984) as one kind of magmatic reaction that is thought to represent magmatism in partially molten domains, in which upcoming melt is reacting with the crystal mush via an interaction zone. The interaction zone represents either a fraction of solid melting, or a fraction of melt crystallising, or both in case of peritectic reactions (Zou and Reid, 2001). The trace element behaviour is affected by these complex melting/crystallisation

processes, which leads to the evolution of the trace element concentrations. Reactive melt flow is a complex process that requires the knowledge of various properties intrinsic to the geological environment such as melt-induced porosities as well as the densities of the fluid and the solid (Reiners, 1998).

There are many other types of magmatic reactions that are thought to occur in nature such as open dynamic melting (Zou, 1998, Ozawa, 2001), continuous melting (Shaw, 2000), incongruent dynamic melting (Zou and Reid, 2001) or batch and fractional melting (Shaw, 1970; Hertogen and Gijbels, 1976).

These magmatic reactions can be implemented in trace element modelling studies. Indeed, the previously quoted authors offer mathematical models to calculate the exchanges of trace element between solid and melt, i.e., mass balance equations (cf. Chapter 4). In this study, only the batch melting reaction will be explored.

1.2.3   Trace elements fractionation

As stated by Bowen (1915), magmatic reactions create different minerals during solidification or melting, and each of the involved crystals have a specific effect on the trace element budget. This effect is usually seen as a fractionation behaviour in which two elements that are incompatible (i.e., preferably entering the liquid phase) are decoupled due to one element having more affinity for a mineral than another.

Magma genesis, migration and crystallisation create various magmatic minerals during the melting/crystallisation reactions that will enhance fractionation between elements. For example, one of the most known signatures is the fractionation between the light REE (LREE) Lanthanum (La) and the heavy REE (HREE) Ytterbium (Yb) (typically illustrated as the La/Yb ratio). The mineral garnet, common in high pressure magmatic and metamorphic environment, is well known to be enriched in HREE (van Westrenen and Draper, 2007 and references therein) and, therefore, control the La/Yb ratio. A melt in equilibrium with garnet will thus have a high La/Yb ratio. Other examples are amphibole that can be enriched with HREE or HFSE (Nandedkar et al, 2016; Tiepolo et al, 2007, Botazzi et al,1999), or plagioclase that can incorporate large amounts of strontium (Chiaradia, 2015; Blundy and Wood, 1991) or the reduced mid REE (MREE) europium Eu^{2+} (Weill and Drake, 1973). These minerals, ubiquitous in the lithosphere and especially in the crust will highly modify the trace element signature of the final melt and solid products. Their various effects on the trace elements budget will facilitate the deciphering of magmatic series of reaction. Hence, these signatures are providing the community with a tool to trace the evolution of an igneous rock from the formation, to the migration and crystallisation of magma.

1.3 The main factors controlling trace elements

1.3.1   Temperature and Pressure

Temperature (T) and pressure (P) control the capacity of rock materials to melt or crystallise, and, therefore, are the drivers for specific minerals to be involved in suprasolidus conditions. They are called intensive parameters in thermodynamic as they do not depend on the chemistry of the system. Generally, the amount of melt is strongly related to temperature and melt fraction also affect the trace element concentration in melt and solid. An incompatible trace element will increase in concentration in the melt when the melt fraction is decreasing and reciprocally. When temperature is falling, the partition coefficient will increase due to the enthalpy of exchange reaction (White, 2007) leading to a progressive decrease of extent of enrichment in the melt. However, while T and P are controlling the state of the system and then the concentration of trace elements in melt/solid, other parameters, such as the chemistry of the system, play a major role in the determination of the extent of enrichment of trace elements in the melt.

1.3.2   Melt composition and polymerisation

Melt composition has also a major effect on trace element behaviour, with more differentiated magmas incorporating more trace elements than primitive magmas (Sisson, 1991; Hart and Dunn, 1993).

Strongly correlated to the melt differentiation is the polymerisation state of the melt that has also a strong effect on the trace element partitioning between melt and solid. The two main chemical component affecting the degree of melt polymerisation are silica and water (Gaetani, 2004, Tiepolo et al, 2007; Blundy and Wood, 2001; van Westrenen and Draper, 2007). Melt polymerisation was first defined by Mysen et al (1982) and refers to the quantification of quasi-lattices present in the melt, i.e., partially crystallised minerals that increase the viscosity of the melt (Mysen et al, 1982; Mysen and Toplis, 2007; Nielsen, 1985; Nielsen and Dungan, 1983).There are two notations available in the bibliography that allows calculating the amount of quasi-lattices. In this study, the method of Nielsen and Dungan (1983) will be used following the recommendation of Tiepolo et al (2007).

1.3.3   Mineral composition

The mineral composition will also be a major controlling factor on the behaviour of trace elements. Indeed, the incorporation of trace elements will largely depends on the incorporation of other major elements in the structure. Since mineral compositions vary and depend on the type of mineral, the effect of mineral composition on trace element behaviour is complex, and will be fully detailed in Chapter 2 and 3.

1.3.4 Accessory phases

Accessory phases are defined by a low amount of these phases in the geochemical system of interest. In most of the magmatic processes involving the differentiation of a mafic melt to a more evolved melt in large scale geological processes, the accessory phases are usually oxides of Fe, Ti, Zr or Mg such as magnetite, ilmenite, rutile, titanite, zircon or periclase. In some cases, phosphate minerals can form such as monazite or apatite. Also, alumina silicates are common such as kyanite, sillimanite or andalousite. Whereas alumina-silicates or iron and magnesium oxides do not affect the trace element behaviour (Luhr and Carmichael, 1980; Nielsen and Beard, 2000), the presence of iron titanium oxides, titanium oxides, zircons or phosphate minerals greatly affect the behaviour of trace elements such as HFSE and Act for titanium oxides and zircons (Foley et al, 2000; Klemme et al, 2005) and REE for phosphate minerals (Fujimaki, 1986; Dawson and Hinton, 2003). Abnormal concentrations of trace elements, forming ore deposits due to a large concentration of these minerals is outside the scope of this study and is not addressed.

1.3.5 Redox conditions

The redox conditions, referring to the chemical potential of O_2 in the system, and commonly expressed as its fugacity (f_{O_2}), also play a main role in the behaviour of trace elements. They define the conditions in which the oxidation state of an element changes. Therefore, redox conditions affect both major and trace elements and change the trace element behaviour for two reasons. First, the change of oxidation state of major elements, such as Fe^{2+} for Fe^{3+}, will change the intrinsic properties of elements affecting the incorporation processes in minerals. These properties, as explained in more detail in Chapter 2, will affect the incorporation mechanisms of trace elements. Second, the change of oxidation state can control the compatible/incompatible behaviour of trace elements themselves. The most well-known example is the change in oxidation state between Eu^{3+} and Eu^{2+}. The reduction applied to this element also involves an increase in ionic radius. As a consequence, Eu^{2+} has a similar ionic radius to Ca and can incorporate more easily the structure of crystals than Eu^{3+} (cf., Chapter 3) (Aigner-Torres et al, 2007; Drake and Weill, 1975).

1.4 Motivations and limitations

The aim of this thesis is to propose a practical way of calculating the behaviour of trace elements in magmatic systems by taking into account the varying controlling parameters listed in the section above. This can be used in numerical modelling studies in which the trace element evolution would provide insights on dynamic magmatic processes. This can offer a practical means to decipher series of magmatic reactions in different geological systems (Sun and Liang, 2013a, 2013b; Yao et al, 2013). Such trace element modelling using variable partition coefficients

would therefore improve the capture of the variation of trace element behaviour in comparison to studies that do not consider these variations (e.g. Laurie and Stevens, 2012; Zhang et al, 2013).

This thesis is based on the advances in our understanding of the partition coefficients systematics between minerals and silicate melts (Blundy and Wood, 1991; Blundy and Wood, 1994), which have enabled the community to constrain predictive models of trace element behaviour for various minerals (see Chapter 3 and reference therein).

The predictive models take into account the chemical variations of the associated minerals and melt, while the understanding of other controlling parameters such as the effect of accessory phases and the redox conditions are still subject to improvement (Aigner-Torres et al, 2007; Laubier et al, 2014; Timm et al, 2010; Foley et al, 2000; Klemme et al, 2005), and will provide limitations to the range of applications of the tool. I focused on the partitioning mechanisms between six major minerals thought to be the main stable phases in large scale geological processes (plagioclase, orthopyroxene, clinopyroxene, amphibole, garnet and olivine, Rudnick and Gao, 1995; Condie and Selverstone, 1999). Other important phases, such as micas or potassic feldspar representative of shallow metamorphic conditions or late stage crystallisation of magma, are not taken into account.

These predictive models provide the stepping stones on which this study relies to create a numerical tool of trace element behaviour between minerals and melt, thereby significantly improving the current trace element modelling methods. The present study allows forward modelling of trace elements in magmatic processes. The tool will be applied to two examples: amphibolite partial melting presented in Chapter 4 and peridotite partial melting presented in appendix A. For the two examples, I will present different examples of outputs created by the tool and will focus on different trace element ratio such as La/Yb, Dy/Yb and Sr/Y. These elements ratio are important in geochemical studies since they can provide information on the mode and nature of source magma in Arc or MOR systems (Profeta et al, 2015; Davidson et al, 2007; Bouilhol et al, 2015; Smith, 2014; Chiaradia, 2015; Moyen and Stevens, 2006).

2. Methods for partition coefficients prediction

In this chapter, I will present different methods that predict trace element partition coefficients in melting environments ranging from 0 to 5 GPa and $700 - 1300\,^{\circ}$C. The first part of the chapter will develop the theory and the concepts associated with partition coefficients that are important to understand the basics of the Lattice Strain Model (LSM). Since the LSM is dependent on various minerals and melt parameters, a thorough understanding of the particularities of this model is necessary for further parametrization in a numerical model. While the LSM is a powerful tool for the prediction of trace element behaviour, the parametrization is often limited by the lack of experimental data for lattice conditions in minerals and trace element partitioning between minerals and melt. As such, regression analyses will be used for these circumstances.

2.1 Definition of partition coefficient D_i

As a simple definition, Di is the measure of the ratio of concentration of elements between supposedly two immiscible solutions as stated by the distribution law expressed by Nernst (1891):

$$D_i = \frac{X_i^A}{X_i^B} \qquad\qquad \text{Eq.2.1}$$

with X_i^A and X_i^B referring to the concentration of a trace element in the phase A and B respectively. In this study, we will consider only the exchange between a mineral and a melt. The partition coefficient Di is a term that encapsulates multiple assumptions. First of all, the system is considered at equilibrium and the solution is ideal (White, 2007), so that the chemical potential of a trace element in the mineral μ_i^{Min} and melt μ_i^{Melt} are written as:

$$\mu_i^{Min} = \mu_i^{Min_0} + RT ln\gamma_i^{Min} X_i^{Min}$$

$$\mu_i^{Melt} = \mu_i^{Melt_0} + RT ln\gamma_i^{Melt} X_i^{Melt}$$

at equilibrium, the two equate:

$$\mu_i^{Min} = \mu_i^{Melt}$$

so that:

$$\mu_i^{Melt_0} - \mu_i^{Min_0} = RT\ln\frac{(\gamma_i^{Min} X_i^{Min})}{(\gamma_i^{Melt} X_i^{Melt})} = RT\ln K_i \qquad \text{Eq.2.2}$$

with μ_i being the chemical potential of element i in the phase of interest, μ_i^0 the standard-state chemical potential of element i in the phase of interest, γ_i the activity coefficient of the element i

in the solution, X_i the mole fraction of element i in the phase of interest, R the gas constant, and T the temperature in Kelvin. K_i represent the equilibrium constant of the solution.

Secondly, in this ideal solution at equilibrium, it is assumed that Henry's law is respected and can be applied to trace elements. This law states that, for an element extremely sparse in a solution (e.g., trace elements in a melt or solid), the molecular interaction between this element and the solution is almost null. In other words, trace elements are considered to move freely between physical states without constraints of molecular bonds. Hence, the activity coefficients in the Eq.2.2 are equal to 1, leading to the following notation:

$$\mu_i^{Melt_0} - \mu_i^{Min_0} = RTln\frac{X_i^{Min}}{X_i^{Melt}}$$

reorganising this leads to:

$$\frac{X_i^{Min}}{X_i^{Melt}} = \exp\frac{(\mu_i^{Melt_0} - \mu_i^{Min_0})}{RT} = D_i \qquad\qquad Eq.2.3$$

In thermodynamics, the variation of chemical potential between two phases is equal to the variation in Gibbs free energy between the two phases, which refers to the work done by a system to change from one state to another. Here, in simple terms, this change in state refers to the exchange of trace elements between a mineral and the melt. Thus, Eq.2.3 can then be written as:

$$D_i = \exp\frac{\Delta G^{Min-Melt}}{RT} \qquad\qquad Eq.2.4$$

Most of the methods presented hereafter in relation to the lattice strain model, take into account the development from Eq.2.2 to Eq.2.4 in the prediction of the partition coefficients, with additional specific attributes that will be presented accordingly.

2.2 Lattice strain model (LSM)

The LSM is a predictive model based on statistical analysis that predict the partition coefficients for cations of different charge and size replacing original cations in the lattice sites of minerals. The partition coefficients for elements to be present in the lattices at trace level are strongly dependent on the composition of minerals and particularly of the lattice composition of final products. It is also strongly dependent on the physical conditions in which the mineral is stable or unstable. It is important to point out that the LSM predicts trace element partition coefficients from an experimentally measured (e.g., LA-ICP-MS) or calculated (e.g., Perple_X, pMELTS) bulk composition of minerals. Therefore, the LSM is able to give a good quantitative approximation of the partition coefficients in minerals/melt systems.

2.2.1   Lattice strain theory

The lattice strain model is based on several studies that tested out the Goldschmidt rules of substitution (Goldschmidt, 1937). These studies worked on the incorporation of an atom of variable ionic size and valence in the structure of a mineral hosting their pure end-members major elements within solid/liquid experiments. Goldschmidt rules are stated as follows (Goldschmidt, 1937):

- If there is a small difference of ionic radius, the smaller ions enter the crystal preferentially.
- For ions of similar radius but different charges, the ions with the higher charge enters the crystal preferentially
- 2 ions with the same valence and radius should exchange easily and enter a solid solution in amounts equal to their overall proportions

It appeared that the behaviour of the lattice under various experimental conditions is not entirely consistent with Goldschmidt rules of substitution (Nasagawa, 1966, Brice, 1975, Onuma et al, 1968). Indeed, in nature, the crystallographic organisation of silicate minerals is not perfect, but exhibits some discrepancies in the electronic/crystallographic configuration called crystallographic defects or point defects. These defects affect the electronic stability of the structure leading to a reorganisation or relaxing of the surrounding ions (Bhagavantam and Pantulu, 1963, Lasaga, 1981, Nelson et al, 1989) that can be suitable for substitution.

As such, Blundy and Wood (1994) and Wood and Blundy (1997), following the work of Brice (1975), proposed another way to measure the substitution of an element of different ionic radius and different valence into the crystal structure by introducing the variation in strain energy needed in a crystal for such substitution. To calculate the energy involved in substituting a major element (ME) having an ideal fit for the lattice site (i.e., no strain applied to the structure) for a trace element (TE), it is necessary to take into account the equilibrium partitioning of both elements, so that the partitioning of ME and TE can be noted as Eq.2.4:

$$D_{ME} = \exp(\frac{-\Delta G^0_{ME}}{RT}) \qquad\qquad \text{Eq.2.5a}$$

$$D_{TE} = exp(\frac{-\Delta G^0_{TE}}{RT}) \qquad\qquad \text{Eq.2.5b}$$

In that case, it is reasonable to assume that the work done to substitute TE for ME is strictly related to the work done by the crystal and the melt exchanging cations of different size or different valence called the elastic strain energy ($\Delta G^{crystals}_{strain}$, ΔG^{Melt}_{strain}). Assuming that the work done by the melt is equal to 0, only the work done by the crystal is taken into account (Blundy and Wood, 1994). Also, the work done is measured from a standard substitution that, in this case, is

linked to the ideal variation of energy ΔG^0_{ME}. In other words, the trace element substitution will depend on the partition coefficient of the most ideal element for the lattice. This yields to the following relationship:

$$\Delta G^0_{TE} = \Delta G^0_{ME} - \Delta G^{crystals}_{strain,TE} \qquad \text{Eq.2.6}$$

Eq.2.6 inserted in Eq.2.5b gives:

$$D_{TE} = \exp(\frac{-\Delta G^0_{ME} + \Delta G^{crystals}_{strain,TE}}{RT}) \qquad \text{Eq.2.7}$$

Finally, by rearranging Eq.2.7 with Eq.2.5a, it is possible to link the highest partition coefficient for the lattice D_{ME} to the variation in strain energy associated with trace elements incorporation:

$$D_{TE} = D_{ME}\exp(\frac{-\Delta G^{crystals}_{strain,TE}}{RT}) \qquad \text{Eq.2.8}$$

In nature, a major element is rarely the best fit for the lattice configuration and therefore rarely represents the maximum partition coefficient for the lattice. Therefore, in Eq.2.8 the D_{ME} is replaced by D_0, which represents the maximum partition coefficient for the lattice of interest (cf 2.2.2). By replacing the notation TE with i, as used in section 2.1, we obtain:

$$D_i = D_0\exp(\frac{-\Delta G^{crystals}_{strain,i}}{RT}) \qquad \text{Eq.2.9}$$

Note that the full theoretical development can be found in Wood and Blundy (1997). The logical next step is to constrain the different parameters that control the variation in $\Delta G^{crystals}_{strain}$ and this will be presented in the next section.

2.2.1.1 Crystallographic dependencies: Size of substituting cations

Crystals are a succession of atoms, cations and anions, repeating the same continuous pattern; the minimum of which being called crystal lattices. Anions being in most cases oxygen, the nature of hosted cations will depend on the spare volume between the anions. These volumes are known as lattice sites. Usually, the size of the lattice is propitious for the incorporation of a major or minor network-modifying cation (Fe, Mg, Ca, Mn, Na, K and Ti ; Nielsen and Dungan, 1983; Nielsen and Drake, 1985) but the point defects occurring in the mineral structure lead to relaxation and deformation of lattices. The allocated elastic energy associated with this relaxation leads to a modification of the lattice site structure, volume and strain potential. Hence, the new set of conditions attributed to the new lattice environment is a new volume and a new value of strain that lead to potential substitution between major and trace elements. These new conditions are a new ideal ionic radius (r_0) and a new Young's modulus (E) (Blundy and Wood, 1994). This leads to the work of Brice (1975) and Nagasawa (1968) that states that $\Delta G^{crystals}_{strain,i}$ for a spherical ion entering a lattice of interest can be expressed as a function of the difference

between the ideal ionic radius r_0 and the substituting cation r_i as well as Young's modulus. In other terms, the element that would allow Eq.2.10 to equate 0 will have the largest partition coefficient:

$$\Delta G_{strain,i}^{crystals} = 4 \cdot \pi \cdot E \cdot N_A \cdot (r_0/2 \cdot (r_0 - r_i)^2 - 1/3 \cdot (r_0 - r_i)^3) \qquad \text{Eq.2.10}$$

where N_A is the scaled Avogadro's number for partition coefficient calculation on a molar basis ($602.214(\times 10^{-26})$ mol^{-1}) (Wood and Blundy ,2013), E is in GPa, T is the temperature in Kelvin, R the gas constant (8.314 JK^{-1}mol^{-1}) and r_0, r_i in Ångstroms.

It is important to realize that both larger and smaller cations than the one of r_0 are affected in the same way since they both increase $\Delta G_{strain,i}^{crystals}$. Then substituting Eq.2.10 into Eq.2.9 gives the following formulation for partition coefficient prediction (Brice, 1975; Blundy and Wood, 1994):

$$D_i = D_0 \cdot exp\left[\frac{-4\pi E N_A (r_0/2\,(r_0 - r_i)^2 - 1/3\,(r_0 - r_i)^3)}{RT}\right] \qquad \text{Eq.2.11}$$

Eq.2.11 shows that the prediction of trace element partition coefficients is dependent on the ionic radius of the element. However, not only are the partition coefficients dependent on the work done by the substitution of an ion of different size but also on the variation in charges between the hosted and substituting cations. Therefore, the aim of a next section will be to take into account the different valences that natural elements have (e.g.,1+ for Rb, 2+ for Sr, 3+ for La, 4+ for Ti,5+ for Ta), which induce changes in mineral composition and, therefore, variation in the trace element partition coefficient.

2.2.1.2 Crystallographic dependencies: Valence of substituting cations
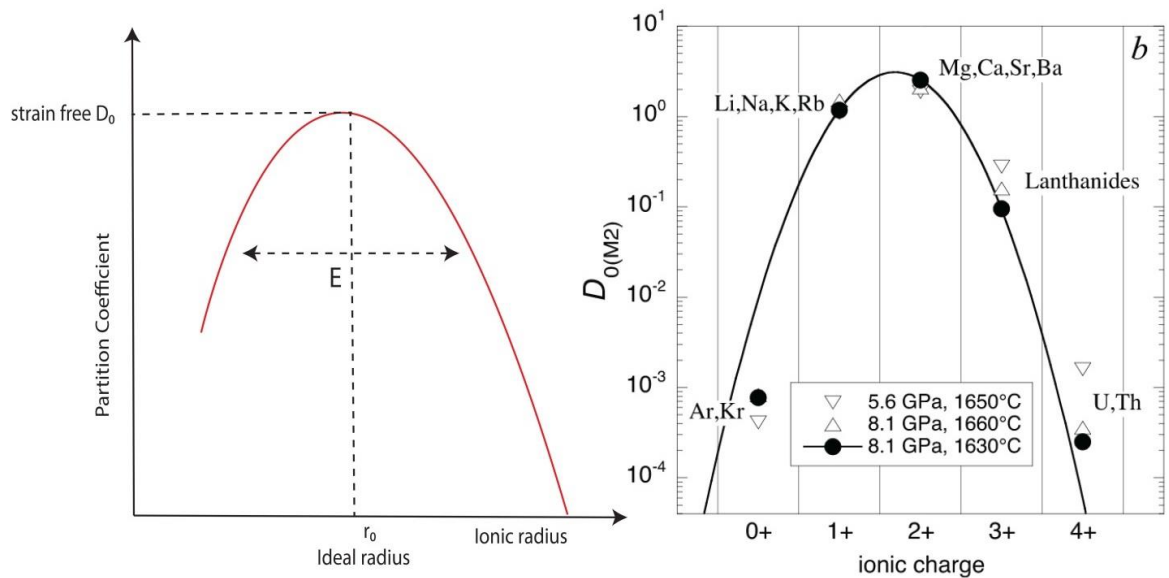
Figure 2-1: <u>Left:</u> *The graphic expression of the Lattice Strain Model or also called Onuma curve (see Eq.2.11) shows the parabolic shape of the curve and the relationship with the size of the substituting cations. It shows the effect of the lattice strain parameters D_0, r_0 and E on the behaviour of the curve and though the partition*

coefficients. As approaching the value of r_0, bigger or smaller cations are equally rewarded (see text). Right: The graphic expression of D_0 in the M2 site of pyroxene (see text Chap.3.3) shows the same parabolic dependencies against the valence of substituting cations. This shows that the LSM has to be used for series of isovalent cations, such as for example, the isovalent series of Rare Earth Element (REE^{3+}). Figure from Blundy and Wood, 2003. Marker shows the same behaviour of D_0 for various pressures and temperatures.

Lattices are electrostatically stable polyhedrons that usually set the electrical conditions favourable for hosting major elements of a specific charge (e.g. no mismatch in the ratio cation/anion, namely for silicate minerals the electronic ratio $\frac{Cation^+}{Oxygen^{2-}}$ should equate 1) and therefore the substitution needs to be in accordance with such electronic configuration. However, it is well known from geochemical measurement that any element can incorporate natural minerals suggesting that lattices are subject to heterovalent substitution. Thus, quantitative development of heterovalent substitution is needed to further understand the principle of substitution in silicate minerals and the use of the LSM (Blundy and Wood, 2003, Wood and Blundy, 2013).

Such quantitative development for heterovalent substitution was done by Wood and Blundy, 2001. On the one hand, they found that the substitution between a trace cation of charge Z_{cation} and a major ion of charge $Z_{initial}$ is controlled by the relation $(Z_{cation} - Z_{initial})^2$. This shows that as for ionic size dependency in Eq.2.10, higher and lower valence are equally penalised since their valences equally differ from the original (i.e. ideal) valence. This assumes that the lattice strain parameters will be sensitive to the valence of the substituting cation, which is in accordance with the observation of Wood and Blundy (2001). As for D_i versus ionic radius, D_0 can schematically be represented by a parabola depending on the valence of cations (Figure 2.1) and Young's modulus varies linearly with the valence of substituting cations (Hazen and Finger, 1979; Anderson and Anderson, 1980). Note that this observation is in discordance with Goldschmidt 3rd rule for substitution that states that cations with higher valence and the same ionic radii enter the lattice more easily.

On another hand, heterovalent substitution in a lattice site alters the ratio cation/anion that will be greater or lower than 1 depending on the valence of the substituting cation. However, this cannot be achieved in a finite crystal structure, and therefore the substitution must be compensated by the addition of compensating cations. For example, Wood and Blundy, 2001 studied the effect of incorporating a Th^{4+} (Thorium) in the M2 site of clinopyroxene and observed that the amount of 4-fold coordinated Al (Al^{IV}) or the inversely correlated 6-fold coordinated Al (Al^{VI}) in the tetrahedron is directly related to the partition coefficient of Th in the M2 site (Wood and Blundy 2001, Hill et al, 2000). Indeed, one way to compensate the incorporation of a cation of greater valence like Th is to substitute Si for Al in the tetrahedric site such as:

$$Th^{4+}Mg^{2+}Al_2^{3+}O_6^{2-} = \frac{Cation^+}{Oxygen^{2-}} = 1$$

This can also work for other cations like REE^{3+} in pyroxene such as:

$$REE^{3+}Mg^{2+}Al^{3+}Si^{4+}O_6^{2-} = \frac{Cation^+}{Oxygen^{2-}} = 1$$

Therefore, Al^{IV} or Al^{VI} are useful proxies to predict the partition coefficient of cations involving heterovalent substitutions in pyroxene offering better quantification of the lattice strain parameters (Wood and Trigila, 2001).

In summary, the lattice strain model has to be used to model series of isovalent cations since the behaviour of the lattice will change greatly from the valence of a substituting cation to another. Heterovalent substitution will also drive the chemistry in the lattices and proxies, such as Al^{IV} or Al^{VI}, can be used to calculate the lattice strain parameters.

2.2.2   Lattice strain parameters

Now that the equation for partition coefficient prediction can simply be written in the form of Eq.2.11 with the consideration of valence of substituting elements, the next step is to constrain the parameters in this equation that vary according to charge and size of the substituting cations as well as the chemistry of the lattices, namely the lattice strain parameters D_0, r_0 and E. The lattice strain parameters constitute an essential part of the LSM since they are dependent on the crystal lattice configuration, and therefore vary from one crystal to another or even from one crystal lattice to another. As such, their calculations are based on numerous experimental analyses that constrain the effect of a chemical or a physical parameter on the behaviour of the lattices (e.g., the Al^{IV} effect on D_0 for pyroxene; Hill et al, 2000). Therefore, the lattice strain parameters are fitted against the best chemical or physical components.

2.2.2.1 Strain free partition coefficient D0

As stated before, the strain-free partition coefficient is the maximum partition coefficient possible for the lattice site of interest and therefore can be written like Eq.2.4. The D_0 can be seen as a fictitious cation that is the perfect fit for the lattice. Considering D_0 the maximum partition coefficient in a crystal of composition X at conditions P and T, D_0 will not only depend on the Gibbs free energy of fusion/crystallisation. D_0 will also depend on the composition of the melt and solid at the pressure and temperature of interest as well as the type of heterovalent substitution involved leading to the following notation:

$$D_0(X,P,T) = \exp\frac{\Delta G^{Min-Melt}}{RT} \qquad \text{Eq.2.12}$$

where X, P, T represents the most effective chemical component in a crystal lattice for the calculation of D_0 and refers to the chemical activity of such component in the system (cf Eq.2.2).

Now, in order to parameterise the Gibbs free energy of fusion for a specific mineral (Figure 2.2), it is necessary to develop the RHS of Eq.2.12, such as the following simplified form (Blundy and Wood, 1997, van Westrenen et al, 1999):

$$\Delta G^{Min-Melt} = \Delta H - T\Delta S + P\Delta V - \frac{1}{2}\left(\frac{\delta \Delta V}{\delta P}\right)P^2 \quad \text{Eq.2.13}$$

where $\Delta H, \Delta S \; and \; \Delta V$ are thermodynamic parameters, representing, respectively, variation of enthalpy, entropy and volume. Whereas T and P are intensive properties of the system and can be determined otherwise, the extensive properties H, S and V remain to be deduced as they are dependent on quantities inherent to the mineral (Figure 2.2). In order to cover a large range of possibilities, a fitting procedure of such parameters to experimental data is required. This leads to polynomial representations such as:

$$G_{P,T}^{Min-Melt} = a_0 + a_1 T + a_2 P + a_3 P^2$$

where a_i are fitting coefficients. Substitution in Eq.2.12 gives the general shape of D_0:

$$D_0(X, P, T) = exp\left(\frac{a_0 + a_1 T + a_2 P + a_3 P^2}{RT}\right)$$

or:

$$ln\big(D_0(X, P, T)\big) = a_{1b} + \frac{a_0 + a_2 P + a_3 P^2}{RT}$$
$$with: a_{1b} = \frac{a_1}{R} \qquad \text{Eq.2.14a}$$

The general shape of Eq.2.14a represents a strong basis for the fitting procedure and may differ according to the minerals as some parameters may have the tendency to decrease the accuracy of the fit. Such fitting procedures were done in numerous studies for different minerals, in which the fitted coefficients were calibrated to have coherent data (Blundy and Wood, 1991; Blundy and Wood, 1994; Blundy and Wood, 1997; van Westrenen et al, 2000, 2001a, 2001b, van Westrenen et al, 2007; Dohmen and Blundy, 2014, Nandedkar et al, 2016).
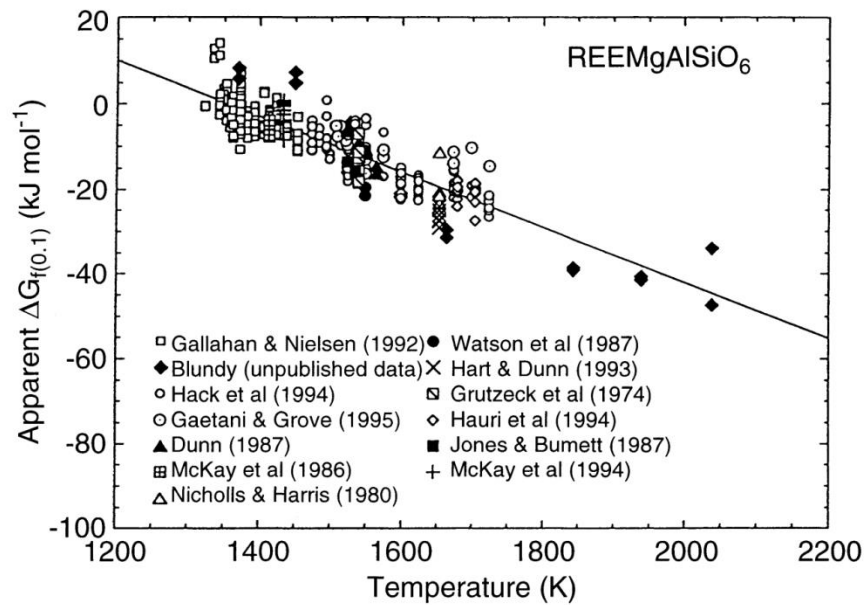
Figure 2-2: *Apparent energy of fusion of REE-bearing diopside (Wood and Blundy, 1997 and reference therein). The figure is an example of the melting relationship of minerals used in the thermodynamic development of either partition coefficients in general (see text) or the strain-free partition coefficient D_0. In this particular case, the data are used to model the strain-free partition coefficient.*

Moreover, some studies consider the variation of enthalpy and volume as being a constant for a given cation valence, which leads to the following notation (Sun and Liang, 2012; Sun and Liang, 2013; Yao et al, 2012):

$$ln\big(D_0\,(X,P,T)\big) = a_{1b} + \frac{a_4}{RT}$$

$$with:\ a_4 = a_0 + a_2P + a_3P^2$$

Eq.2.14b

This gives different equations of D_0 that will be presented in Chapter 3.

2.2.2.2 Ideal ionic radius

As for D_0, r_0 represents the radius of the fictive element that would enter the lattice with no strain. This parameter is mainly dependent on the composition of the crystal and the nature of the substituting cation (Figure 2.3, Law et al, 2000) and, in some cases (e.g., Plagioclase), on temperature (Wood and Blundy, 1997, Dohmen and Blundy, 2014). The lattice size will vary with the amount of major elements settled in the lattice. Then, the prediction of r_0 is derived from numerous experimental analyses in which various crystal compositions were explored and r_0 derived from fitting procedures (Blundy and Wood, 1991; Blundy and Wood, 1994; Wood and Blundy, 1997; van Westrenen et al, 2000, 2001a, 2001b, 2007; Dohmen and Blundy, 2014, Nandedkar et al, 2016). The fitting process will follow a linear relationship with the elements present in the lattices and on temperature such as the following:

$$r_0 = c + bT + a_1x_1 + a_2x_2 + \cdots + a_nx_n \qquad \text{Eq.2.15}$$

where x_n represents the cation per formula unit calculated on a molar basis and T the temperature. Also, b, a_n and c are fit coefficients. This gives different equations of r_0 that will be presented in Chapter 3.

2.2.2.3 Young's modulus

Young's modulus (E) is a measure of the stiffness of the lattice meaning the resistance of a lattice to applied stress. As a simplification, the mineral is considered to be isotropic in order to use one value of E for one mineral composition (Brice, 1975). Young's modulus is given in GPa (GigaPascal) and gives insight in the behaviour of trace elements. Indeed, for a given cation valence, a low value of E means bigger cations can enter the lattices with more ease and, inversely, high value of E means bigger cations will have difficulties to enter the mineral structure. In other terms, the value of E controls the tightness of the Onuma curve seen in Figure 2.1. Moreover, Hazen and Finger (1976) and Anderson and Anderson (1970) observed that the compressibility of the lattice site is a function of the nature of the substituting cation. In other words, Young's modulus decreases linearly with the decrease of the substituting cation charge. This is supported by the work of Blundy and Wood (1991) and Blundy and Wood (1994) in which they observed this linear behaviour for cations substitution in plagioclase, and proposed the following relationship:

$$E^{1+} = \frac{1}{3}E^{3+} < E^{2+} = \frac{2}{3}E^{3+} < E^{3+} < E^{4+} = \frac{4}{3}E^{3+} \qquad \text{Eq.2.16}$$

where n^+ indicates the charge of the substituting cation. In some cases, such as when the data does not fit Eq.2.16, it is necessary to derive Young's modulus from experimental studies. Also, it is necessary to determine the value of E^{3+} in order to use the relationship described Eq.2.16.
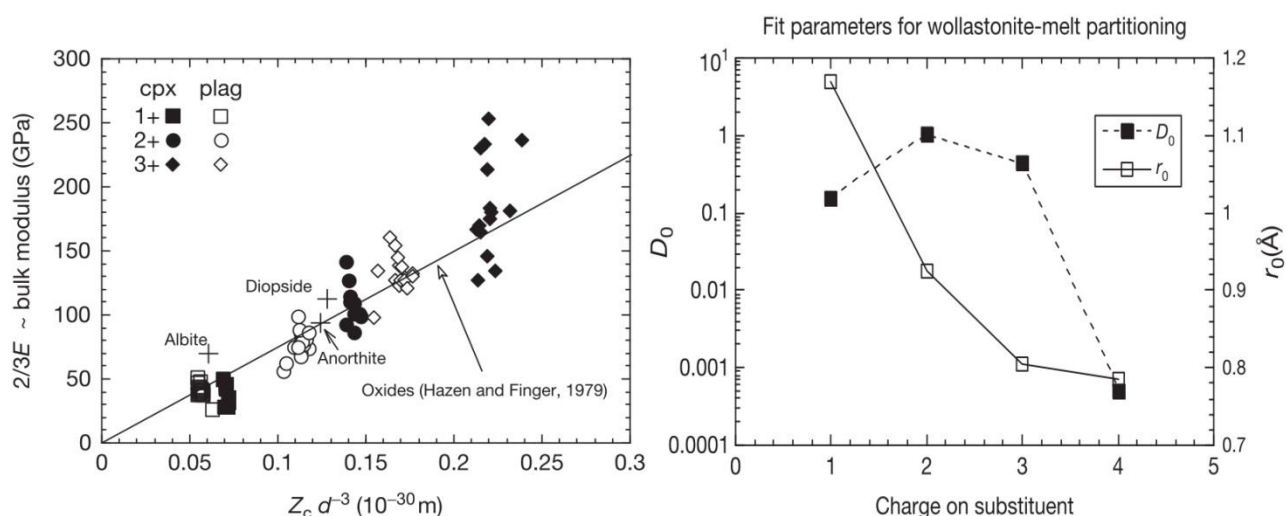
Figure 2-3: <u>*Left:*</u> *Example of a linear trend between the bulk modulus K of plagioclase and clinopyroxene and the charge of the substituting cations; with E=1.5K for silicate minerals (Blundy and Wood, 1997). The stiffness of the lattices decreases with decreasing cation charge and allows for a simpler notation (see text).*

Figure from Blundy and Wood, 1994. Right: Parabolic relationship of D_0 in calcic-clinopyroxene (wollastonite) as seen in Figure 2.1. Also, r_0 decreases as the cation charges decrease. However, the nonlinear relationship makes it impossible to fit the data to a simple curve, as it is possible with Young's modulus. Figure from Law et al, 2000.

Experimental studies on a large range of minerals composition were used to derive Young's modulus and in most cases, compositional dependencies were found. Young's modulus being a variable inherent of the lattice composition, it is not surprising that it is affected by the same parameters as r_0. As such, it is possible to derive E directly from r_0 through a linear relationship (Yao et al, 2012; Sun and Liang, 2012a, 2012b):

$$E = b + a_1 r_0 + f(X,P,T) \qquad \text{Eq.2.17}$$

Where a_1 and b are fitting coefficients and $f(X,P,T)$ an additional compositional or physical variable that can improve the fit and r_0 the ideal ionic radius. This gives different equations for E that will be presented in Chapter 3.

In summary, D_0 gives the maximum partition coefficient possible for a given mineral composition. The r_0 gives the radius of the element that would be the most acceptable one by the mineral. Finally, Young's modulus controls how much the partition coefficient varies with the cation radius deviating from r_0 (Figure 2.2, 2.3).

2.2.3   Lattice strain model with proxies

The lattice strain model with proxies respects the same development as the normal LSM. The only difference is that D_0 is not used in the model and this leads to a slightly different notation of Eq.4.1. First introduced by Blundy and Wood (1994), the method allows predicting the behaviour of isovalent series of trace elements directly from a major element with the same valence. In fact, for most of the minerals, 1+ and 2+ cations have an analogue major element sitting in the lattices such as Na for 1+ cations or Mg, Fe and Ca for 2+ cations. For example, in order to find the behaviour of Sr^{2+} and Ba^{2+} in garnet, the proxy Mg will be used, since Mg represents the most ideal element behaviour in this mineral. The lattice strain model with proxy is described as follows:

$$D_i = D_x \cdot exp\left[\frac{-4\pi E N_A \left(\frac{r_0}{2}(r_x^2 - r_i^2) - \frac{1}{3}(r_x^3 - r_i^3)\right)}{RT}\right] \qquad \text{Eq.2.18}$$

where x denotes the element used as a proxy (e.g., Na, Ca, Fe or Mg).

Therefore, the use of the lattice strain model with proxy will be largely used in Chapter 3 for 2+ and 1+ substituting cations.

2.3 Regressions and multiple regressions predictive models

In the case where the lattice strain model is not applicable due to a lack of data to correctly fit the lattice strain parameters, multiple regression analysis will be used. This approach, that does not consider the thermodynamics background for Di, can provide more accurate values of partition coefficients in the region where Henry's law is likely not valid (i.e., where the activity coefficient ratio of elements between two phases is not equal to one). For example, if the melt fraction is relatively small, and therefore concentration of highly incompatible trace elements in the melt relatively high, the chemical interactions between trace elements and melt can potentially have an impact on the properties of the melt, and in that case Henry's law is not respected and the use of the LSM can be biased.

Regression analyses do not need a quantitative theoretical background as for the LSM. For example, trace element behaviour in plagioclase will depend on either the anorthite or the albite content and to some extent on the Al content of the mineral since this mineral is made exclusively from these constituents. The multiple regression analyses will then be tested against these parameters.

Most of the models presented thereafter are from the bibliography and in most cases have the following shape:

$$D_i = a_1 x_1 + a_2 x_2 + \cdots + a_n x_n + b \qquad \text{Eq.2.19}$$

where x represents the parameter used for the fitting procedure. Also, a_i and b are fitting coefficients.

In some cases, the literature investigation did not lead to accurate or existing predictive models. In that case, I gathered partition coefficient data from the literature and tested several compositional parameters (cf., Chapter 3). The fitted curves have the following notation:

$$D_i = a_1 x + a_2 x^2 + a_3 \qquad \text{Eq.2.20}$$

$$D_i = a_1 x_1 + a_2 x_2 + a_3 x_1 x_2 + a_4 \qquad \text{Eq.2.21}$$

$$D_i = a_1 \exp(a_2 x) + a_3 \exp(a_4 x) \qquad \text{Eq.2.22}$$

where x represents the variable parameter tested for the fit. Again, a_n are fitting coefficients. In extreme cases, neither of the fit procedures tested gave significant results and, in those cases, a weighted average was used to find the most accurate values to represent the used set of data.

To conclude, LSM, LSM with proxies, and regression analyses are the state-of-the-art models to predict the partition coefficients between melt and minerals under various conditions. One problem is that each of those models are, for now, working independently to investigate the

effect of one phase on an initial budget of trace elements (Yao et al, 2012) or between two phases and the melt (Klemme et al, 2002). To study a geological system, it is therefore important to investigate the effect of a wider range of minerals onto an initial trace element budget. The next chapter will therefore concentrate on the gathering of predictive models of partition coefficients for 6 different minerals that are thought to play major roles in trace element differentiation. These roles can be of 2 kinds. Firstly, minerals can have an active effect meaning that they have affinity with some traces elements generating typical trace element signature (e.g., garnet). Secondly, minerals can have a passive effect meaning that they do not have affinity with trace elements but their ubiquity in some geological system affect the trace element budget (e.g., olivine in upper mantle).

3. Trace element predictive models for 6 mafic minerals: Results

In this chapter, I present the results for trace element behaviour between minerals and melts. Results were obtained from an extensive bibliographic review on trace element partitioning for the 6 main mafic minerals playing the major role in trace elements processes. This study also proposes preliminary results on predictive models that are not found in the bibliography. The minerals explored are plagioclase, orthopyroxene, clinopyroxene, amphibole, garnet and olivine. The usual behaviour of trace elements in these minerals is displayed in Figure 3.1. Note that, as stated in Chap.1, other main phases such as titanium oxides or phosphate oxides have not been investigated in this study. Here, I present why some minerals have more affinity with trace elements than others and I show the intimate link between crystal parameters (e.g., variation in lattice site volumes or variations in coordination number) and the elements inside the lattice (Table 1). Following the crystallographic presentation, I list the essential major cations thought to have the most influential effect on the mineral structure and electric configuration for the accommodation of trace elements. The major cation composition of a mineral greatly influences the choice of the predictive models used in TEPM. Since LSM predicts partition coefficients for series of isovalent elements, I use the following notation for practical reason: LILE will be divided in two subgroups, namely LILE1 (Cs^+, Rb^+, K^+) referring to the LILE cations of valence 1, LILE2 (Ba^{2+},Sr^{2+}) listing LILE cations of valence 2, HFSE4 (Ti^{4+},Hf^{4+},Zr^{4+}) are HFSE cations of valence 4, and HFSE5 (Ta^{5+},Nb^{5+}) refers to HFSE cations of valence 5.

Table 1: List of parameters and abbreviations used in the models and equations of Chapter 3.

List of parameters	Definition	List of parameters	Definition
$C_j^i (wt\%)$	*Concentration of oxide j in phase i*	$T(K)$	*Temperature in Kelvin*
Mg_n^i	*Mg number in phase i* $= \dfrac{Mg}{(Fe + Mg)}$	$P(GPa)$	*Pressure in Giga Pascal*
$Al^{iv}(a.p.f.u)*$	*Atoms per formula unit of Al 4 − fold coordinated*	X_{EM}	*Fraction of end − member EM***
$X_j^s(a.p.f.u)$	*Atoms per formula unit of element j in lattice site s*	γ_j^i	*Activity coefficient of element j in phase i*
$X_j^i(mol)$	*Molar concentration of element j in phase i*	$\dfrac{Xnf}{X}$	*Melt polymerisation (Nielsen and Dungan, 1983)*
$r_0^{n+}(Å)$	*Ideal ionic radius for n + cations. r_0 in Ångstroms*	$E^{n+}(GPa)$	*Young modulus for n + cations. E in GigaPascal*

* a.p.f.u= atom per formula unit

** Example: X_{Wo}= fraction of wollastonite end member, or calcic pole, in pyroxene (see text)

Note that the models presented hereafter are used in Chapter 4 and the behaviour of trace elements in the main minerals will be shown in Figure 4.2 of Chapter 4 and in appendix C and D.
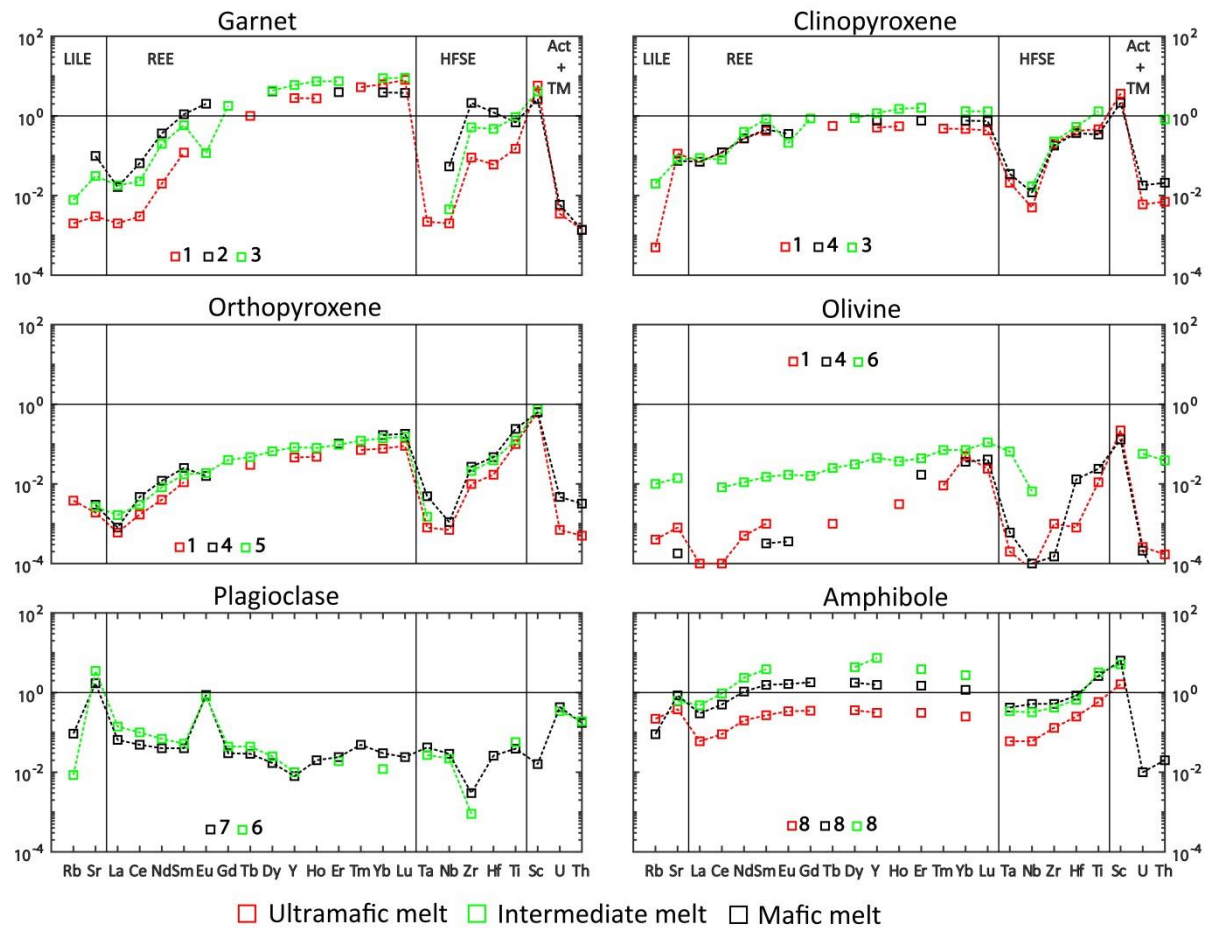
Figure 3-1: *Spidergrams of trace elements partition coefficient between the 6 minerals studied in this work for different melt compositions. This figure displays the usual behaviour of trace element in these minerals. Note that trace element behaviour (especially REE) in amphibole is really sensitive to melt composition. Garnet shows this dependency only for HFSE. Olivine shows a strong variation between mafic/ultramafic and intermediate. Other minerals do not show any correlation, suggesting that other chemical parameters are playing a dominant role in their trace element substitution. 1: Adam and Green (2006), 2: Hauri et al (1994), 3: Barth et al (2002), 4: McDade et al (2003), 5: Yao et al (2012), 6: Dunn and Senn (1994), 7: Aigner-Torres et al (2007), 8: Tiepolo et al (2007).*

3.1 Case 1: plagioclase (pl)

Plagioclase is ubiquitous in all crustal systems and is found in every magmatic and metamorphic environment. Plagioclase crystals are solid solutions between a sodic-endmember called Albite (Ab) and a calcic-endmember called anorthite (An) (Figure 3.2) with the calcic end-member crystallising at higher temperature and the sodic pole at lower temperature. From this simple statement, it can be inferred that calcic plagioclase are found in basaltic systems whereas sodic plagioclase are found in intermediate to felsic systems. In progressively cooling magma, it is often possible to find zoned plagioclase crystals with a mafic core (An) and a more acidic rim (albite: Ab). This zonation process is often used in petrological studies to tease out magmatic processes

such as magma cooling, mixing, and emplacement rate (Humphreys, 2009; Zellmer et al, 2003; Tepley et al, 2000; Menard and Spear, 1996).

In term of trace element behaviour in plagioclase, it is well known that several trace elements might be compatible in this mineral according to specific conditions. For example, plagioclase has a well-known effect on the behaviour of europium, which informs on the melt redox conditions (Weill and Drake, 1973; Drake, 1975; Wilke and Behrens, 1999, Aigner-Torres et al, 2007). Indeed, europium is sensitive to the change in oxygen fugacity conditions in the melt, according to which this element changes its valence from 3+ to 2+. This leads europium to have a similar ionic radius as Ca and be compatible in plagioclase. In such condition, it is referred to as the so called "europium anomaly" in melt generated from plagioclase rich layers. As stated before, the fugacity changes are not taken into account in the modelling component of our study. The europium anomaly is not explored in this study. Models exist in the literature (Aigner-Torres et al, 2007), but are only useful if the redox conditions of a system (i.e., oxygen fugacity fO_2) are known. Another particularity of plagioclase is that REE have an inverse trend, which means that La is more compatible than Yb (Drake and Weill, 1975) (Figure 3.3). This differs from other minerals explored in this study and is of value for modelling magma genesis and trace element signatures. Finally, LILE2 have the tendency to be compatible in plagioclase (Butler and Skiba, 1964; Blundy and Wood, 1991) (Figures 3.1, 3.3) giving another window into the deciphering of magmatic processes such as those occurring for mantle plume – lithosphere interaction (Sobolev et al, 2000), MOR processes (Niu and O'Hara., 2008; Zimmer et al, 1995), or lower crustal magmatic processes (Bouilhol et al, 2015; Chiaradia; 2015; Jagoutz et al, 2012).
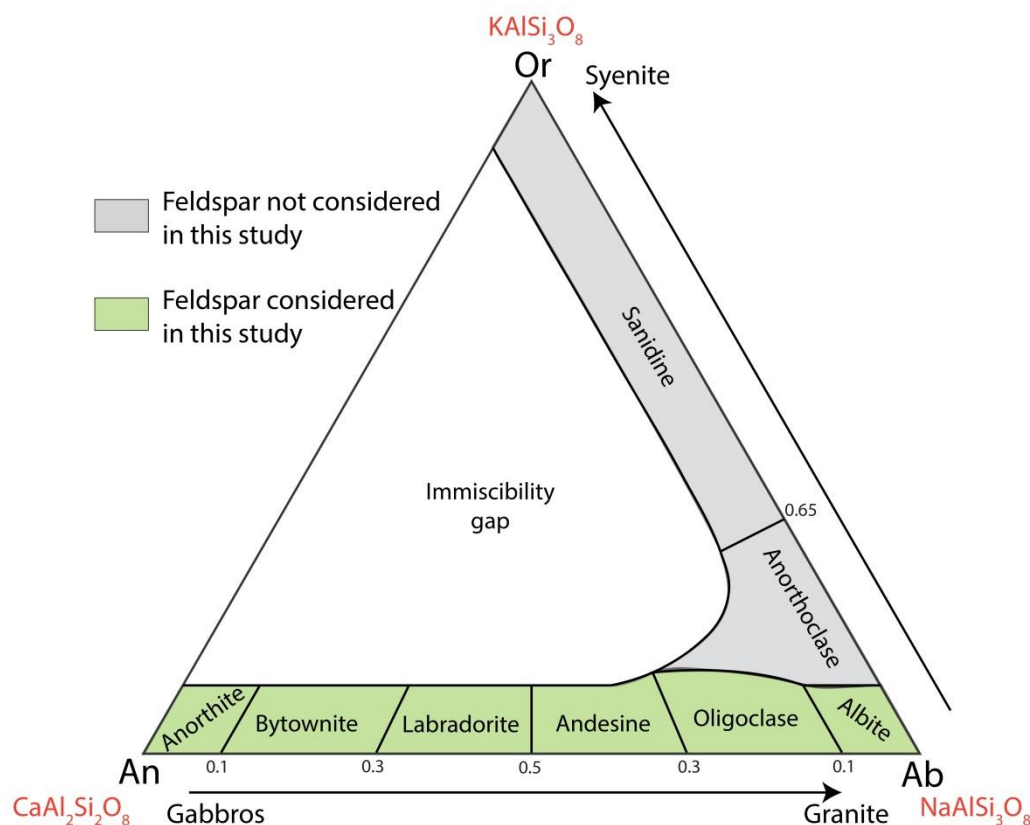
Figure 3-2: *Ternary plot showing the variability of feldspar at 900°C, modified from Deer et al (1963). The anorthite to albite transect shows the continuous series of plagioclase from anorthite in gabbro-like compositions to albite in granite-like compositions. K-feldspar enters in the discontinuous series of magmatic rocks (Bowen, 1915). K-felspar rich rocks help to classify rocks from gabbro-granite to syenite. Shaded green: Felspars that are considered in this study. Shaded grey: Range of feldspar that are not considered in this study (although model can be found in White (2003)).*

Note that this study does not investigate the alkali feldspar Orthoclase (Figure 3.2). However, trace element predictive models exist in the literature and can be used for future improvement (White, 2003).
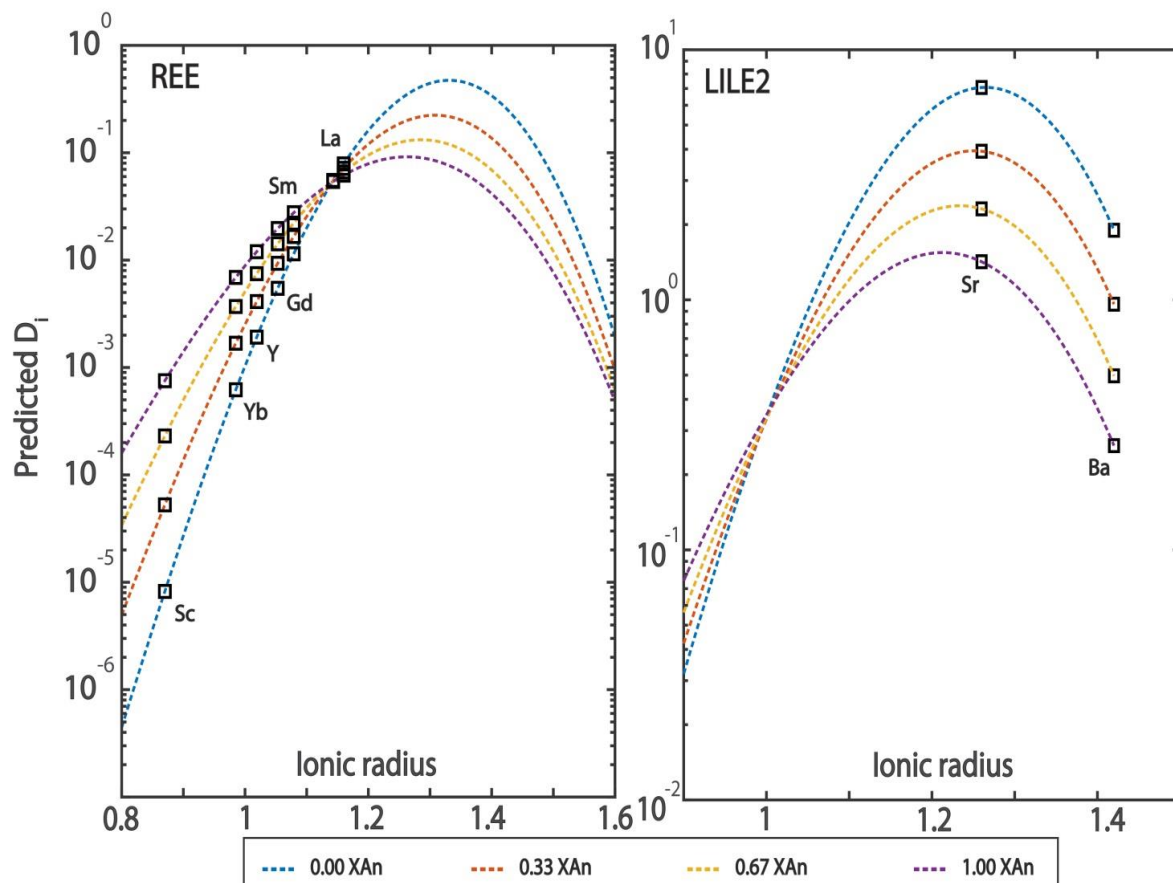
Figure 3-3: *Onuma curves for an empirical study of the behaviour of trace element according to the variation of the X_{An} parameter in plagioclase at constant temperature (1100°C) and $C_{SiO_2}^{melt}$, for REE (left figure) and LILE2 (right figure). The increase in X_{An} content in plagioclase decreases the strain free partition coefficients D_0, but increases the elasticity of the M1 site. This behaviour implies that LILE2 incompatibility increases with increasing X_{An} and, reciprocally, REE incompatibility decreases with increasing X_{An}.*

3.1.1   Structure of plagioclase

Plagioclase is a framework crystal and has only one large 8-fold coordinated M site in which all the trace elements and also the network modifying elements are situated. The coordination number CN is the number of oxygen atoms shared by the tetrahedron to the lattice. An example of a plagioclase structure of anorthite plagioclase is displayed in Figure 3.4 in which a cation Ca is sitting in the 8-fold coordinated M lattice. The structure notation (Str) for anorthite and albite end-members are (Megaw, 1962; Papike, 1976):

$$\text{Anorthite} \qquad M_{(Ca,LILE2,REE)_2} T1_{Al,Ti_2} T2_{Si_2} - O_8 \qquad \text{Str.1a}$$

$$\text{Albite} \qquad M_{(Na,LILE1,LILE2)} T1_{Al,Ti_1} T2_{Si_3} - O_8 \qquad \text{Str.1b}$$
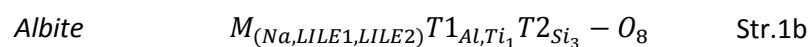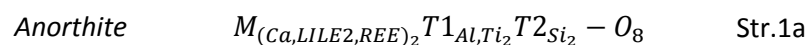
in which M is the lattice site and T the tetrahedron. A particularity of the plagioclase structure is that there are two distinct tetrahedral sites in which Al and Si contribute to the crystal building. Therefore, despite their apparent simplicity, plagioclase crystals have a complex crystallographic evolution between the An-Ab end-members accounting for the order-disorder of Al and Si in the tetrahedron. Indeed, Al is a 3+ cation and Si a 4+ cation meaning that the electrical defect brought by Al must always be balanced. In other words, an Al tetrahedron cannot share oxygen with another Al tetrahedron. This is the Al/Al avoidance of plagioclase and controls the crystallographic structure and symmetry of the plagioclase crystals together with temperature (Papike, 1976, Megaw, 1962). Therefore, the variation in the proportion of Al and Si in plagioclase along the An-Ab end-members join goes together with an evolution in the crystal structure. In fact, the anorthite crystal has a triclinic structure and a space group $P\bar{1}$ (Figure 3-4) and it evolves progressively to the triclinic structure with space group $C\bar{1}$ of albite.

Figure 3-4: OAB view on the triclinic $P\bar{1}$ structure of Anorthite plagioclase (Labradorite) from Wenk et al (1980). Note the slight deviation between the superposition of tetrahedron. This is the structural consequence of Al-Si ordering and structure evolution from $P\bar{1}$ to $\overline{C1}$. This view displays the M sites of plagioclase structure where large trace elements will substitute. Smaller trace elements such as HFSE may substitute Al or Si in the tetrahedron.

Therefore, the proportion of Si-Al in plagioclase controls the chemical composition of the M site by incorporating more or less Ca or Na cations. This structural control applies also to trace elements. This structural control can be measured by the amount of Ca and Na cations present in the M site given by the anorthite component X_{An} (Blundy and Wood, 1991; Blundy and Wood, 1994), written as:

$$X_{An} = \frac{X_{Ca}^{pl}}{(X_{Ca}^{pl} + X_{Na}^{pl})} \qquad \text{Eq.3.1}$$

The An-component is therefore a major controlling parameter for trace element behaviour prediction in plagioclase.

3.1.2   Trace element controlling parameters in plagioclase

Blundy and Wood (1991) have set the basis for our understanding of trace-element behaviour in plagioclase as a function of X_{An}, and further extended their study to the first applied LSM on this mineral (Blundy and Wood, 1994). The elastic properties of the crystals and, therefore, the trace element partitioning in plagioclase is mainly controlled by crystal chemistry (Brown et al, 2016). As an example, Figure 3.3 displays variation of partitioning behaviour of LILE2 and REE according to the variation of the anorthite component using the models of Dohmen and Blundy (2014). However, the control of X_{An} seems to be limited to the alkali elements (LILE), REE and Act or, in other words, to cations with large ionic radii (Bédard, 2006, Bindeman and Davis, 2000). The fate of smaller cations like HFSE and scandium is not dependent on the variation of X_{An} since the small size of these cations is more suitable in the tetrahedral site of plagioclase (Papike, 1976; Dohmen and Blundy, 2014). Indeed, HFSE are much smaller than Na and Ca and the single site of plagioclase is too large to accommodate small and high valence elements. This led Bédard (2006) to observe that melt chemistry is a controlling parameter on the behaviour of HFSE. Hence, it is reasonable to think that quasi-lattices in the melt prior to formation of plagioclase control the substitution mechanisms of small cations. This again relates to the melt polymerisation and the silica content of the melt (c.f. 1.2.2).

3.1.3   LSM

3.1.3.1 REE+Y

The models for REE and Y in plagioclase are used from Dohmen and Blundy (2014). As stated before, REE behave according to the variation in X_{An} leading to the following models for the lattice strain parameters (Figure 3.2).

The ideal ionic radius is written as:

$$r_0 = 1.331 - 0.068 \cdot X_{An} \quad \text{Mod.1.1a} \quad \text{Dohmen and Blundy (2014)}$$

Young's modulus equates to:

$$E = 152 - 31 \cdot X_{An} \quad \text{Mod.1.1b} \quad \text{Dohmen and Blundy (2014)}$$

Finally, the strain-free partition coefficient is not used for REE in plagioclase. Instead, La is used as a proxy for the calculation of other REE. The behaviour of La is dependent on Ca and Na in the M site D_{La}:

$$D_{La} = \frac{D_{Ca}^2}{D_{Na}} \cdot exp\left(\frac{4400 - 30.8\,T}{RT}\right) \quad \text{Mod.1.1c Dohmen and Blundy (2014).}$$

For partition coefficient predictions of the REE, the models Mod.1.1a, Mod.1.1b and Mod.1.1c must be integrated in the LSM with proxy equation (Eq.2.18).

3.1.3.2 LILE2

The models for LILE2 in plagioclase are also from Dohmen and Blundy (2014). LILE2 being larger than Ca, their behaviour is dependent on X_{An} (Figure 3.2).

The ideal ionic radius is written as follows:

$$r_0 = 1.29 \cdot T^r + 1.3.\,10^{-4} \cdot (T - T^r) +$$

Mod.1.2a Dohmen and Blundy (2014)

$$[-0.095 \cdot T^r - 4.10^{-5} \cdot (T - T^r)] \cdot X_{An}$$

with T^r a reference temperature for LILE2-Ca exchange in plagioclase:

$$T^r = 1563 \ K$$

Young's modulus equates to:

$$E = 120.038 - 0.37 \cdot X_{An} \quad \text{Mod.1.2b} \quad \text{Dohmen and Blundy (2014)}$$

Finally, Ca is logically representing the most ideal 2+ element behaviour in the M site of plagioclase. Therefore, Ca is used as a proxy for LILE2 partition coefficients. Although it is possible to use the Nernst partition coefficient for Ca, Dohmen and Blundy (2014) propose the following model for D_{Ca}:

$$RTLnD_{Ca} = -19107 + 467 \ C_{SiO_2}^{melt} \qquad \text{Mod.1.2c} \qquad \text{Dohmen and Blundy (2014)}$$

For partition coefficient predictions of the LILE2, the models Mod.1.2a, Mod.1.2b and Mod.1.2c must be integrated in the LSM with proxy equation (Eq.2.18).

3.1.3.3 LILE1

The models for LILE1 in plagioclase are taken from Dohmen and Blundy (2014). As LILE2 and REE, LILE1 are dependent on the variation of the An component, so that the following models can be used.

The ideal ionic radius is written as:

$$r_0 = 1.24 - 0.017 \cdot X_{An} \quad \text{Mod.1.3a} \quad \text{Dohmen and Blundy (2014)}$$

Young's modulus equates to:

$$E = 49.05 + 17.16 \cdot X_{An} \quad \text{Mod.1.3b} \quad \text{Dohmen and Blundy (2014)}$$

Finally, Na has the most ideal behaviour of +1 cation in plagioclase. Like Ca for LILE2, Na is used as a proxy for LILE1 prediction and the following model is used to parametrise Mod.5.3a and Mod.5.3b as:

$$RTLnD_{Na} = 13621 - 18990 \ X_{An} \qquad \text{Mod.1.3c} \quad \text{Dohmen and Blundy (2014)}$$

For partition coefficients prediction of REE, the models Mod.1.3a, Mod.1.3b and Mod.1.3c must be integrated in the LSM with proxy equation (Eq.2.18).

3.1.4 Regressions analysis

Predictive models used in this study are from the regression and multiple regression analyses of Bédard (2006), Bindeman and Davis (2000) and Bindeman et al (1998). From these studies, it is possible to extract a generic notation for the predictive models used for HFSE4, HFSE5 and Act. This notation is written as follows:

$$RTLnD_{TE} = a_{TE} + b_{\ TE}C_{SiO_2}^{melt} + c_{TE}\ C_{MgO}^{melt} + d_{TE}\ X_{An(\%)} \quad \text{Mod.1.4}$$

In Mod.5.4a, a_{TE}, b_{TE}, c_{TE} and d_{TE} are fitted coefficients, listed in Table 6.

Table 2: Coefficients for HFSE4, HFSE5 and Act used in Mod.1.4 as predictive models for plagioclase-melt partition coefficients.

Trace elements TE	Coefficients			
	a_{TE}	b_{TE}	c_{TE}	d_{TE}
$Ti^{1,3}$	-15.4	0	0	-28.9
Hf^1	-148.68	1.670	1.276	0
Zr^1	-187.27	2.26	0	0
U^2	-7.45	0	0	-48.4
Th^2	-11.65	0	0	-31.369
Nb^1	-417.35	5.26	10.34	0.41
Ta^1	-271.6	3.16	8.93	0.26
Sc^1	-23	0	-7.54	0

[1] Models from Bédard (2006)

[2] Models from Bindeman and Davis (2000)

[3] Models from Bindeman et al (1998)

The results presented in Table 6 show that small cations are more dependent on melt composition than the variation of X_{An}, suggesting that the partition coefficients for small HFSE and TM depend on melt polymerisation.

3.2 Case 2: orthopyroxene (opx)

Orthopyroxene (opx) or subcalcic pyroxene are ferromagnesian or mafic minerals that can appear in many different magmatic or metamorphic environments, either as a fractionating phase from parental melts, or as a HT metamorphic product. They are also an important phase during partial melting of peridotite or amphibolites leading to dunite in the mantle and gabbro-like igneous rock

rich in opx (Nandedkar et al, 2014, Bouilhol et al, 2015), or eclogite-like igneous rock (Qian and Hermann, 2013) in crustal systems. Although the affinity of opx for trace elements is rather low (Figure 3.1), the amount of opx, representing up to 33 wt.% of the upper mantle (Morgan and Anders, 1980; Kinzler and Grove, 1992; Herzberg and Zhang, 1996; Walter, 1998), makes this mineral a major phase for trace element storage and fractionation. Melting/crystallisation events or melt transfer in orthopyroxene-rich layers not only greatly affect the budget of trace elements due to the opx in mantle derived rocks, but also affect greatly the melt major element composition, which is also important for further magmatic reactions and trace element fractionation processes (Sorbadere et al, 2013).
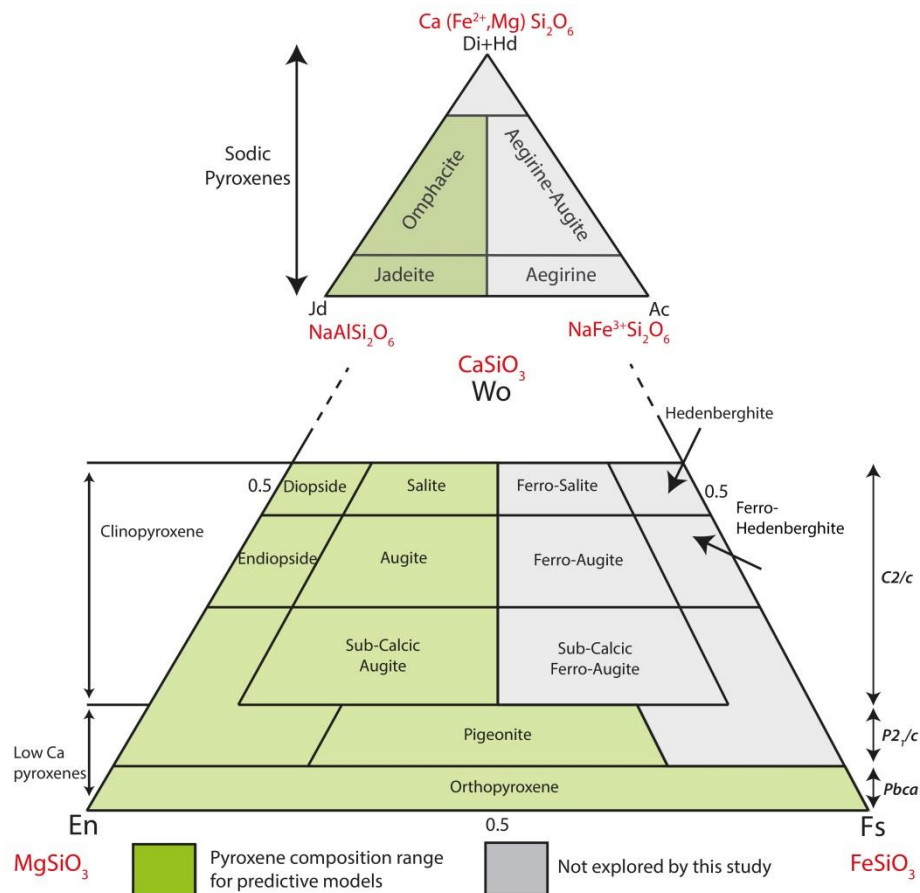
Figure 3-5: _Bottom figure:_ Ternary plot of calcic and ferro-magnesian pyroxene covered by this study. Pure end-members are En (Enstatite), Fs (Ferrosilite) and Wo (Wollastonite). Right-hand side double arrows display the evolution in space groups and crystallographic networks (Bravais lattices) according to the enrichment of pyroxene in Calcium. _Top figure:_ Ternary plot of sodic pyroxene also covered by this study where Jd is the Jadeite endmember (Al^{3+}) and Ac the Acmite endmember (Fe^{3+}). Green shaded area shows the range of composition of pyroxene for which the predictive models can be used. Grey shaded area shows the range of pyroxene composition not covered by this study due to different trace element behaviour in Fe and Fe pyroxene (see text).

3.2.1   Structure of opx

In the pyroxene class represented in Figure 3.5, opx is a solid solution represented by high proportions of enstatite (En: Mg^{2+} [SiO3], magnesium pole) and ferrosillite (Fs: Fe^{2+} [SiO3], ferrous pole) and some wollastonite (< 5%, Wo: Ca^{2+} [SiO3], calcic pole). En, Fs and Wo are the pure end-members of the pyroxene class, and opx is a mix between En and Fs with a low Wo content, which is referred to as a solid solution. The usual structure of opx is noted as follow:

$$M2_{(Mg,Fe,Ca,Na,K)}M1_{(Mg,Fe,Al)}T_{(Si,Al)_2} - O_6 \qquad \text{Str.2a}$$
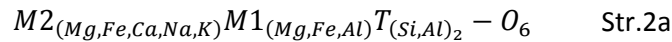
M2 and M1 refer to the 2 lattice sites in pyroxene where trace elements and network modifying cations are hosted in opx, and T refers, as in plagioclase, to the tetrahedral site that mostly hosts Si. However, minor Al incorporates the T site to locally re-equilibrate the structure. M2 and M1 are both octahedrons in opx with a usual coordination number of 6 (CN6), but can be of CN8 if bigger cations such as Ca are hosted in the lattice (Sun and Liang, 2013; Wood and Blundy, 2013; Cameron and Papike, 1981). The M2 site of opx is the largest site and is less stiff than the M1 site with the latter being the smallest of the M sites (Cameron and Papike, 1981) (Figure 3.6). Since the ionic radius (IR, see List of abbreviations) of elements varies from large (LILE: e.g. Cs^+ = 1.67Å (CN6)) to small (HFSE: e.g. Hf^{4+}= 0.71Å (CN6)) and show affinity with the M sites accordingly (Blundy and Wood, 1997; Sun and Liang, 2013; Yao et al, 2012; Wood et al, 1999), the notation of the Str.2a can be modified and noted as follows for the various trace elements explored in this study:

$$M2_{(LILE1,LILE2,REE,Act)}M1_{(HFSE4,HFSE5,TM)}T_{(Ti)_2} - O_6 \quad \text{Str.2b}$$

The structure notation Str.2b shows the most suitable place for specific trace elements to substitute in a fictive opx rather than a finite composition of opx that can be seen in nature. In other words, Str.2b shows the trace element ordering in opx.

From a strict crystallographic point of view, opx is an inosilicate that have an orthorhombic bravais lattice system and have the space group Pbca (Figure 3.6). The structure is therefore a succession of chained Si tetrahedrons that repeat in three dimensions according to the symmetry of the space group and the bravais lattice leaving additional place for network modifying cations in the lattice sites. Orthorhombic Pbca inosilicates crystals such as opx have an ideal composition of Mg and Fe in the M1 and M2 sites with Fe preferentially occupying the M2 site (Cameron and Papike, 1981). Therefore, an understanding of the lattice conditions in opx according to the amount of major network modifying cations hosted in the lattice (e.g., Mg, Fe, Ca) and the tetrahedral site (e.g., Si, Al) is essential in order to propose an accurate predictive model for each trace elements of interest.

3.2.2   Trace element controlling parameters in orthopyroxene

For opx, the incorporation of trace elements will be related to the rate of exchange of Fe and Mg between the opx and the melt. These are simply measured by the partition coefficients of these cations or by the Mg number in opx (Mg_n^{opx}) (Bédard, 2007, Frei et al, 2008). However, one particularity of opx is that, as stated before, Fe and Mg are hosted in both M1 and M2 sites and that the order-disorder arrangement of these cations (a theoretical evaluation of the substitution between the two sites, see Bragg and Williams, 1934 for details) is strongly dependent on the temperature of closure of the system in which the opx crystals crystallise (Wood and Banno, 1973; Stimpfl et al, 1999, Stimpfl et al, 2005, Kroll et al, 1997). Therefore, quantifying the amount of X_{Fe}^{M1}, X_{Mg}^{M1}, X_{Fe}^{M2} and X_{Mg}^{M2} is necessary for trace element calculation purposes. Despite the studies of Stimpfl et al (1999) and Wang et al (2005) on cation ordering for enstatite-like opx in a wide range of temperatures, the systematics of order-disorder in opx has not been deciphered and experimental values for Fe and Mg in the two lattices show too much variabilities, such as in a.p.f.u: 0.00137<Fe(M1)<0.0739,   0.0170<Fe(M2)<0.3037,   0.9145<Mg(M1)<0.9803, 0.6784<Mg(M2)<0.9788. Hence, due to these rather large variabilities, the method of Wood and Banno (1973) will be used, which consists on the following assumption:

$$Mg_n^{opx} = \left(\frac{X_{Mg}^{M1+M2}}{X_{Fe+Mg}^{M1+M2}}\right) = \left(\frac{X_{Mg}^{M2}}{X_{Fe+Mg}^{M2}}\right) = \left(\frac{X_{Mg}^{M1}}{X_{Fe+Mg}^{M1}}\right) \qquad \text{Eq.3.2}$$

Eq.3.2 suggests that Mg-Fe ordering is random in the M1 and M2 site, which simplifies the calculation of the amount of Fe and Mg in both lattices. Indeed, Str2a suggests that the M2 site in opx can host other major cations such as Ca, Na and K but that the total amount of cations in the M2 site is equal to 1 a.p.f.u leading to the following development:

$$X_{Fe+Mg}^{M2} = 1 - (X_{Ca}^{M2} + X_{Na}^{M2} + X_K^{M2}) \qquad \text{Eq.3.3}$$

Substituting in Eq.3.2 for the M2 site gives:

$$X_{Mg}^{M2} = Mg_n^{opx} . X_{Fe+Mg}^{M2} \qquad \text{Eq.3.4}$$

From there it is straightforward to calculate the amount of Fe in both sites and Mg in the M1 site. Note that this development works only for Fe^{2+} and the systematics for the acmite pyroxene are not the same due to the presence of Fe^{3+} in this mineral common in oxidised conditions (cf., Chapter 1.3, Figure 3.5).

The amount of Ca present in the structure will also be a proxy for trace element substitution since this larger cation applies a strain to the lattice, deforming the surrounding tetrahedron chain. This indicates that potential substitution for trace elements will occur nearby to re-adjust the opx

crystal. The models presented hereafter consider that Ca is hosted exclusively in the M2 site, which is in accordance with experimental observations (Cameron and Papike, 1981).

Another process to take into account is the heterovalent substitution occurring in opx. The incorporation of cations of greater valence will change the electronic configuration of the crystallographic environment that has to be accommodated by the crystal involving coupled substitution. A well-studied proxy to measure this accommodation is to calculate the amount of Al^{3+} present in the tetrahedric site (4-fold coordinated Al: Al^{IV}) for opx, which can be inversely correlated with Al^{3+} in the M1 site (6-fold coordinated Al^{VI}) (cf., Chapter 2.2.2).

Also, melt composition plays a role in trace element partitioning and the amount of Si, Al, Fe or Mg from the melt is often used as a controlling parameter for trace element behaviour in opx. Orthopyroxene is a ferro-magnesian mineral and trace element incorporation will depend on the degree of acidity of the melt (cf., Chapter 1.3). This is consistent with the observation of Bédard (2007) who observes a regular increase of element compatibility in opx according to the amount of MgO or FeO. The dependency on melt Si and melt Al might account to the substitution of Si by Al in the tetrahedron of opx, which depends directly to the melt polymerisation and the formation of quasi-lattices (cf., Chapter 1.3).
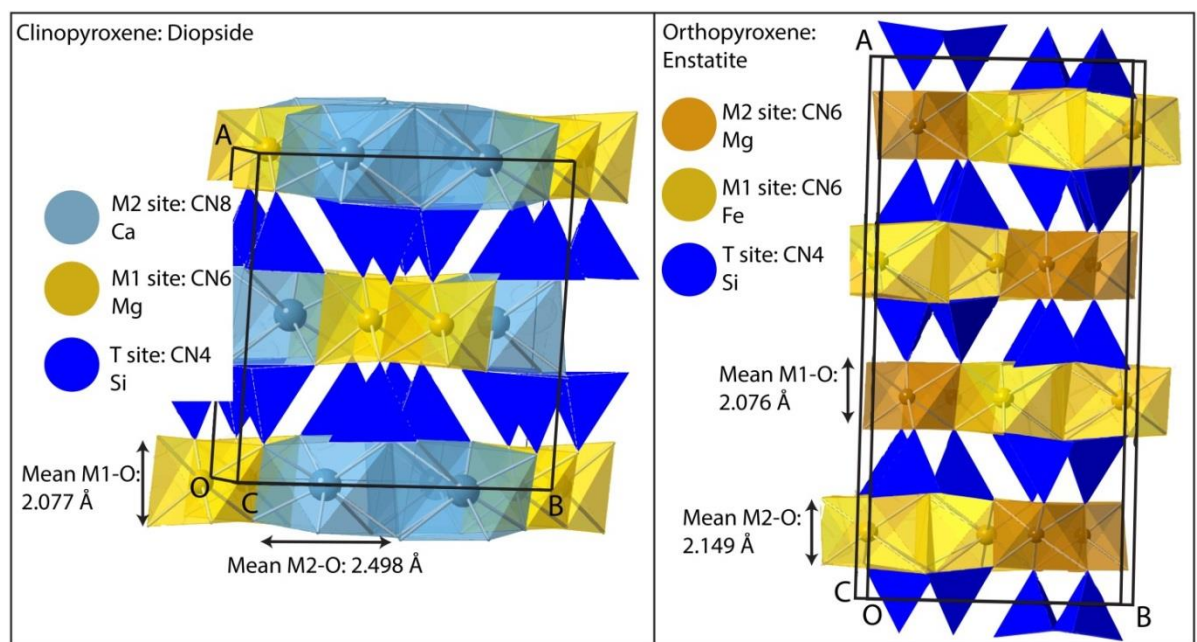
Figure 3-6: Crystallographic expression of pure diopside (left figure) and pure enstatite (right figure). Both figures display the M1, M2 and tetrahedral sites in pyroxene. Atomic bond lengths M-O are the mean distance between the cation in the lattices and the bonded oxygen for completely ordered pyroxene. They represent the size of the lattice (atomic bond length data are from Cameron and Papike (1981)). The M2 site of cpx is larger than the M2 site of opx, which facilitates the substitution mechanism in cpx. Otherwise, the M1 sites in opx and cpx are identical and are thought to have the same elasticity constant (Wood et al, 1999). Left: Diopside is crystallised according the Monoclinic Bravais lattice and has the space group C2/c

(Thompson and Down, 2008). Right: Enstatite is crystallised according the orthorhombic Bravais lattice and has the space group Pbca (Smyth, 1973).

3.2.3   LSM

3.2.3.1 REE+Y

The models for REE in opx are found in the work done by Yao et al (2012). The fitting procedure on the lattice strain parameters is made on crystal composition from enstatite-like opx to sub-calcic augite. Due to the order-disorder process in opx, the models for REE work reasonably well for ferrosillite-like opx, with the exception of Fe^{3+}-rich opx, which requires more work.

The ideal ionic radius is calculated as:

$$r_0^{3+} = 0.69 + 0.43\, X_{Ca}^{M2} + 0.23\, X_{Mg}^{M2} \quad \text{Mod.2.1a} \quad \text{Yao et al (2012)}$$

Young's modulus relationship is dependent on the ionic radius and the amount of Ca in opx (Figure 3.7):

$$E^{3+} = [-1.37 + 1.85\, r_0 - 0.53\, X_{Ca}^{M2}] \cdot 10^3 \quad \text{Mod.2.1b} \quad \text{Yao et al (2012)}$$

Finally, the strain free partition coefficient is given by:

$$lnD_0^{3+.} = -5.37 + \frac{38700}{RT} + 3.56\, X_{Ca}^{M2} + 3.54\, Al^{iv} \quad \text{Mod.2.1c} \quad \text{Yao et al (2012)}$$

For the partition coefficient prediction of REE, the models Mod.2.1a, Mod.2.1b and Mod.2.1c must be integrated in the LSM equation (Eq.2.11).

3.2.3.2 LILE2

For LILE2 in orthopyroxene, the models from Wood and Blundy (2013) are used. LILE2 are incorporated in the M2 site of opx, since that site has a less stiff, more voluminous lattice site that is more suitable for the large LILE2 cations.

The ideal ionic radius is written as follows:

$$r_0^{2+} = r_0^{3+} + 0.08 \qquad \text{Mod.2.2a}$$

Wood and Blundy (2013)

Young's modulus for LILE2 in opx is given by Wood and Blundy (2013) as being the following constant:
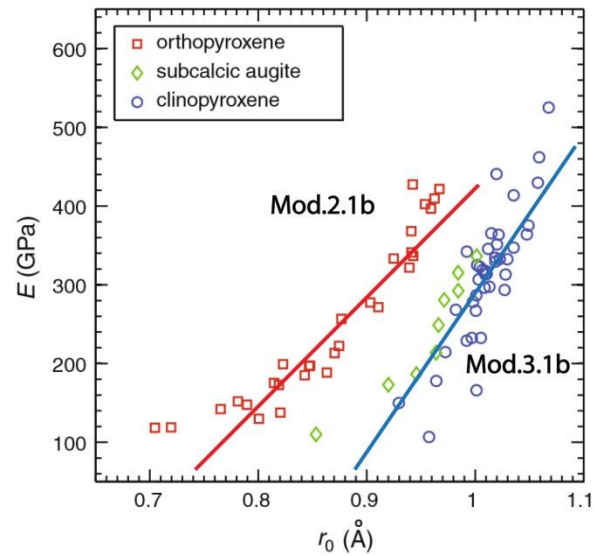
Figure 3.7: Example of relationship for Young's Modulus E and the ideal radius in orthopyroxene, clinopyroxene and subclacic-augite for REE (Yao et al, 2012). The red and blue straight lines is Mod.2.1b and Mod.3.1b fitted empirically on the figure, respectively.

$$E^{2+} = 240 \quad \text{Mod.2.2b} \quad \text{Wood and Blundy (2013)}$$

Finally, the strain-free partition coefficient is not used in the models for LILE2. Instead, proxies can be used since Mg and Fe may have the most ideal cation behaviour in the M2 site depending on the amount of Fe and Mg in the M2 site, which is given by Eq.3.1. Wood and Blundy (2013) consider that, for basaltic systems, the partition coefficient for Mg or Fe is equal to one and propose to use this value as D_{Mg} or D_{Fe}, so that:

$$D_{Mg} = D_{Fe} = 1 \quad \text{Mod.2.2c} \quad \text{Wood and Blundy (2013)}$$

However, this value might not be representative for Si-rich melt. Therefore, I tried to test higher partition coefficient for Mod.2.2c such as $D_{Mg} = 15$ for opx-silica rich melt from Qian and Hermann (2013). The attempt did not lead to significant improvement for the model and rather decreases the accuracy of the prediction. This suggests that the main factor controlling the LILE2 behaviour in opx is the size of the lattice rather than Mg or Fe partitioning. Hence, for LILE2 partition coefficient predictions, the models Mod.2.2a, Mod.2.2b and Mod.2.2c are integrated in the LSM with proxy (Eq.2.18).

3.2.3.3 HFSE4

The models for HFSE4 in orthopyroxene are used from Sun and Liang (2013b). HFSE4 are incorporated in the (6-fold coordinated) M1 site of opx, so the 6-fold coordinated values of ionic radius must be used (Shannon, 1976).

The ideal ionic radius is dependent on the amount of Ca in the M2 site and Mg in the M1 site. As stated before, the amount of Ca in the M2 site not only deforms the M2 lattice but also the adjacent M1 lattice. The amount of Ca therefore affects the ionic radius of the M1 site. The models are written as follows:

$$r_0^{4+} = 0.618 + 0.032\, X_{Ca}^{M2} + 0.03\, X_{Mg}^{M1} \quad \text{Mod.2.4a} \quad \text{Sun and Liang (2013b)}$$

Young's modulus of the M1 site is really stiff and will be considered by TEPM to be constant (Sun and Liang, 2013b):

$$E^{4+} = 2203 \quad \text{Mod.2.4b} \quad \text{Sun and Liang (2013b)}$$

Finally, one would anticipate that the M1 site strain free coefficient is dependent on the variation in the local charge in this site given by Al[iv] (Wood and Blundy, 2003). In orthopyroxene, the composition of the M2 site also plays a role in the distribution of HFSE4 in the M1 site so that the strain free partition coefficient is given by (Figure 3.8):

$$D_0^{4+} = -4.825 + \frac{31780}{RT} + 4.17\, X_{Al}^{iv}$$

$$+8.55\, X_{Ca}^{M2} \left(X_{Mg}^{M2}\right) - 2.62\, X_{Fe}^{M1}$$

Mod.2.4c   Sun and Liang (2013b)

For the prediction of partition coefficients for HFSE4, the models Mod.2.4a, Mod.2.4b and Mod.2.4c must be integrated in the LSM equation (Eq.2.12).
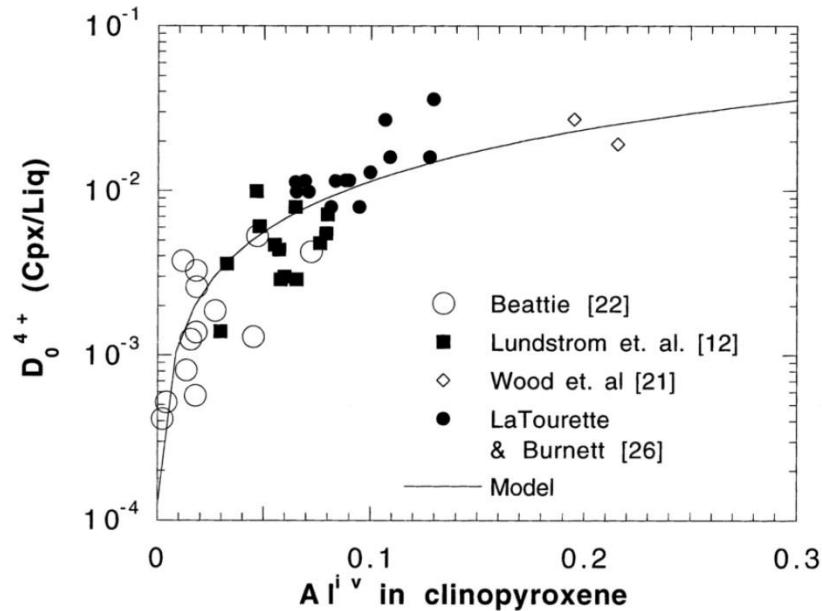
Figure 3-7: *Example of relationship between mineral composition and the strain free partition coefficient for 4+ cations in the M1 site of pyroxene (see text: Mod.1.4c; Mod.2.4c, Eq.2.14b). In clinopyroxene, Al^{iv} is a proxy for the lattice parameters in the M1 site, since Al^{iv} witnesses a variation in the local charge. Note that this dependency is also applicable to orthopyroxene and for other trace element that change the local charge in pyroxene (LILE1, REE, HFSE5, Act and TM) (Wood and Blundy, 2013). Figure from Wood and Blundy (2003).*

3.2.4   Regressions analysis

The regressions analyses and the results of predictive models for LILE1, HFSE5, actinides and transition metals are from Bédard (2007). This study explores all the parameters thought to play an important role in the partition coefficients for orthopyroxene and proposes the following predictive models.

3.2.4.1 LILE1

For LILE1, Bédard (2007) proposes different dependencies according to the type of LILE1.

For the highly incompatible element Cs, the predictive model shows that the behaviour of this element seems to be related to physical conditions, i.e. the composition of the melt and the composition of the mineral:

$$LnD_{Cs} = 23.6 - 1.46\,P - 0.26\,C_{SiO_2}^{melt} - 32.49\,Mg_n^{opx} \quad \text{Mod.2.5a} \quad \text{Bédard (2007)}$$

For Rb, the proposed behaviour of the element depends on the physical condition and melt composition:

$$LnD_{Rb} = -24.88 + \frac{31496}{T} - 0.35\,C_{SiO2}^{melt} + 1.3\,C_{Al2O3}^{melt} \quad \text{Mod.2.5b} \quad \text{Bédard (2007)}$$
$$-0.65\,ln\big(C_{MgO}^{melt}\big) - 3.95\,Mg_n^{melt}$$

Note that the models for Cs and Rb were derived from only 5 and 8 experimental data respectively. Therefore, further studies on the partition coefficients of LILE1 between melt and opx can probably improve the models significantly.

For K, the partition coefficient seems to depend on the physical condition and composition of both the melt and the mineral (Bédard, 2007):

$$LnD_K = -13.05 + 0.95\,P - 0.43\,X_{Wo} + 0.13\,C_{SiO2}^{melt} \quad \text{Mod.2.5c} \quad \text{Bédard (2007)}$$
$$-0.94\,ln\big(C_{FeO_{tot}}^{melt}\big) + 1.34\,ln\big(C_{MgO}^{melt}\big)$$

As stated before, for the highly incompatible LILE1elements, the partitioning behaviour is more dependent on physical condition and melt composition than the composition of the mineral (cf., Chapter 1.3).

3.2.4.2 HFSE5

For HFSE5, Bédard (2007) finds a correlation with the amount of 4-fold coordinated Al in opx.

For Ta, the model shows a simple linear relationship with the amount of Al^{iv} such that:

$$D_{Ta} = -1.68 + 0.62\,Al^{iv} \quad \text{Mod.2.6a} \quad \text{Bédard (2007)}$$

For Nb, the model suggests that the behaviour of this element depends on the amount of Al^{iv} as well as the behaviour of Ta. This is in accordance with the fact that opx is not known to fractionate Nb from Ta:

$$D_{Nb} = D_{Ta}\big(1.17 - 3.16\,Al^{iv}\big) \quad \text{Mod.2.6b} \quad \text{Bédard (2007)}$$

Mod.2.6b and Mod.2.6a were derived from only 10 and 15 experimental data respectively, which suggests that more data are needed to better constrain these models.

3.2.4.3 Actinides

For the actinides model, Bédard (2007) proposes that the composition of opx is the main parameter governing the behaviour of Th and U. Indeed for U, the Mg number in opx is thought to control the partition coefficient such as:

$$D_U = exp\big(3.967 - 11.668\, Mg_n^{Opx}\big) \quad \text{Mod.2.7a} \quad \text{Bédard (2007)}$$

For Th, both mineral and melt composition are represented in the model, although mineral composition seems to have more control:

$$LnD_{Th} = -6.71 + 19.59\, Al^{iv} + 2.1\, ln\big(C_{FeO}^{opx}\big) \quad \text{Mod.2.7b} \quad \text{Bédard (2007)}$$
$$-2.55\, ln\big(C_{MgO}^{melt}\big)$$

3.2.4.4 Scandium (TM)

For the behaviour of the transition metal Sc, Bédard (2007) proposes that the compositions of the mineral and the melt control the partition coefficient:

$$LnD_{Sc} = 5.04 - 4.37\, Mg_n^{opx} - 0.41\, ln\big(C_{FeO}^{opx}\big) - 0.318\ ln\big(C_{MgO}^{melt}\big) \quad \text{Mod.2.8 Bédard (2007)}$$

It is important to note that Sc does not behave as REE + Y, since Sc substitutes in the M1 sites of opx, despite being a transition metal like Yttrium. Indeed, the small size of Sc (IR (CN6) = 0.745Å) allows this element to enter the small M1 site.

3.3 Case 3: clinopyroxene (cpx)

Clinopyroxene differs from orthopyroxene by the incorporation of more calcium in its structure. Cpx is a major phase in mantle and crustal systems, as well as metamorphic environments. Importantly, Cpx major and trace element composition is often used as a marker of the melt composition. The importance of cpx lies in the fact that trace elements might be compatible in this mineral under specific conditions and therefore, plays a major role in trace element fractionation (Blundy et al, 1998). Indeed, clinopyroxene-bearing rocks from MOR conditions such as gabbros or pyroxene cumulates (Warren, 2016) show that MREE and HREE are compatible in cpx with D-values up to 1.2 (Nagasawa, 1973; Irving and Frey, 1984). Cpx is the main phase in melt production during mantle melting, and controls most of the mantle melt composition. In arc settings, cpx is ubiquitous in the fractionation sequence of primary magmas, making it a key mineral for the understanding of arc petrogenesis. Cpx can have D-values for HREE and MREE up to about 20 for highly differentiated products (Mahood and Hildreth, 1983) but can also have D-values > 1 in other systems, depending on its composition (Figure 3.1). Also, Cpx shares an intimate relationship with amphibole, either during crystallization or melting, where amphibole is a peritectic product of the reaction between cpx and melt. The understanding of element partitioning in cpx is thus of major importance for the generation and evolution of magmas in general (Smith, 2014; Bouilhol et al, 2015a).

3.3.1 Structure of cpx

The structural formula of cpx is identical to opx (Str.1a) and the incorporation of trace elements in the structure can be written as in Str.1b. However, REE potentially enter the M1 site in Fe^{2+}-rich calcic pyroxene (Figure 3.6) and the use of the models presented below will lead to large error for Fe-rich cpx (Olin and Wolff, 2012). As stated above, the pyroxene solid solution will present more Ca in the structure, more correctly, the mineral will be composed of more Wo (>20%). The incorporation of more Ca results in loss of symmetry relative to opx and monoclinic spacegroup C2/c (Cameron and Papike, 1981, see Figure 3.6). This structure forms a larger M2 site that is needed for the incorporation of larger cations (cf., Str.2b). The M2 site in cpx is of coordination 8 (CN8) and the study of the trace elements has to be treated accordingly (e.g,. the ionic radius of the element in 8-fold coordination, Shannon, 1976).

Another important group of clinopyroxene are the Na-bearing pyroxene or sodic pyroxene (Figure 3-5). Sodic pyroxene has also the space group C2/c and a monoclinic crystalline network. The first particularity of this mineral is that the M2 site is mainly composed of Na in the endmembers jadeite and acmite and a mixture of Ca and Na in omphacite and aegirine-augite (Figure 3-5). The other particularity is that the M1 site is no longer occupied by a 2+ cation, but by a 3+ cation such as Al for Jadeite and Fe^{3+} for acmite. This common occurrence of a 3+ balanced M1 site and a 1+ balanced M2 site in pyroxene is usually used to understand the substitution mechanism of LILE1 in clinopyroxene by investigating the jadeite-diopside join (Blundy and Wood, 1994). Note that the Acmite endmember bearing Fe^{3+} is usually a typical clinopyroxene of oxidised conditions, which is not explored in this study (cf., Chapter 1.3)

3.3.2 Trace element controlling parameters in clinopyroxene

In clinopyroxene, as in orthopyroxene, the chemical composition of the crystals will be the main controlling factor for trace element substitution. Therefore, it is necessary to quantify the amount of major elements in the lattices to be able to calculate the partition coefficient.

Despite Ca being the major component of the M2 site, Mg or Fe can replace Ca to locally rearrange the structure. This leads to having the same order-disorder mechanism in cpx as in opx. Indeed, as in opx, Mg and Fe are the major element sitting in the M1 site. Therefore, In order to quantify the amount of Fe and Mg in both lattices for partition coefficient modelling, the development presented in Eq.3.2, Eq.3.3 and eq.3.4 will be used.

Also, like in opx, the ordering of Al in the tetrahedral site (Al^{iv}) or the M1 site (Al^{vi}) will be a good proxy to quantify heterovalent substitution and is used in several model presented below (cf., Chapter 2.2.2).

3.3.3 LSM

3.3.3.1 REE + Y

The models for REE in clinopyroxene are from Sun and Liang (2012). The REE and Y enter the M2 site of cpx so that ionic radii of elements coordinated 8 must be used. Sun and Liang (2012) gathered partition coefficients for cpx in systems involving cpx and basaltic to intermediate melt with $C_{SiO_2}^{melt} < 57$. In order to test the validity of the Sun and Liang (2012) models for more acidic melt ($C_{SiO_2}^{melt} > 57$), this study attempted to predict partition coefficients between cpx and tonalitic melt form Barth et al (2002). Results in Figure 3.9 show that the model of Sun and Liang (2013) reproduces well the partition coefficients of REE. The main outlier is Eu, which misbehaves in oxidised melt (cf., Chapter 1.3).
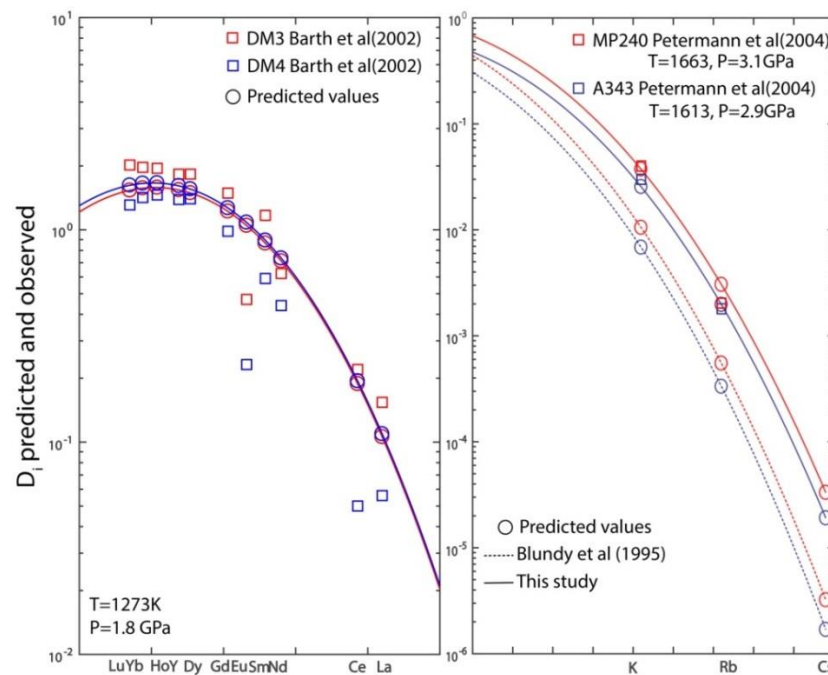
Figure 3-8: Testing the predictive models against experimental data. <u>Left figure</u>: Onuma plot displaying the LSM for REE predicted with Mod.3.1a, Mod3.1b and Mod3.1c from cpx crystallising in silica rich tonalitic melt $C_{SiO_2}^{melt} = 69\ wt\%$ (Barth et al, 2002; Sun and Liang, 2012). The models were tested against partial melting experiments DM3 and DM4 of Barth et al, 2002. The HREE are predicted well by the models. Eu is in 2+ state in the experiments of Barth et al (2002) due to melt oxidation, which complicates correct modelling of this element (cf, Chapter 1.3). The LREE (La and Ce) are not predicted well for experiment DM4. This might be due to the complexity of measuring the two highly incompatible elements in cpx. <u>Right figure:</u> Onuma plots displaying the LSM for LILE1 in cpx predicted from two experiments of Petermann et al (2004). The correction applied to Mod.3.3a allows fitting correctly the experimental data of Petermann et al (2004) to the LSM curve.

Other outliers are La and Ce for experiment DM4 that might be related to properties inherent to the experimental procedure used by Barth et al (2002) that limits the detection of these two highly incompatible elements in the minerals and the melt. This test against tonalitic melt is considered acceptable since the predicted partition coefficients reflect well the behaviour in the

experiments of Barth et al (2002). These models are, therefore, used to model trace element behaviour in felsic system.

The ideal ionic radius model is:

$$r_0 = 1.066 - 0.104 \cdot X_{Al}^{M1} - 0.212 \cdot X_{Mg}^{M2} \quad \text{Mod.3.1a} \quad \text{Sun and Liang (2012)}$$

The predictive models for Young's modulus show a dependency on r_0 (Figure 3.7), which is parameterised with:

$$E = [2.27 \cdot r_0 - 2] \cdot 10^3 \quad \text{Mod.3.1b} \quad \text{Sun and Liang (2012)}$$

and the strain free partition coefficient is written as follows (Figure 3.9):

$$LnD_0 = -7.14 + \frac{71900}{RT} + 4.37 \cdot Al^{iv} + 1.98 \quad \text{Mod.3.1c} \quad \text{Sun and Liang (2012)}$$
$$\cdot X_{Mg}^{M2} - 0.91 \cdot X_{H20}^{melt}$$

The models Mod.3.1a, Mod.3.1b and Mod.3.1c must be integrated into Eq.2.11 for the partition coefficient prediction.

3.3.3.2 LILE2

The models for LILE2 in cpx are from Wood and Blundy (2013). LILE1 enters the M2 site as well, and therefore ionic radii of CN8 have to be used in this model. The model for the ionic radius is noted as follows:

$$r_0^{2+} = r_0^{3+} + 0.06 \quad \text{Mod.3.2a} \quad \text{Wood and Blundy (2013)}$$

Young's modulus follows the Hazen and Finger (1979) relationship (Figure 2.3):

$$E^{2+} = \frac{2}{3} \cdot E^{3+} \quad \text{Mod.3.2b} \quad \text{Wood and Blundy (2013)}$$

Finally, for LILE2, Ca is used as a proxy since it reflects the most ideal behaviour of a 2+ cation in the M2 site of cpx. Therefore, Ca being a major element, it is possible to measure the partition coefficient directly from the Nernst equation:

$$D_{Ca} = \frac{X_{Ca}^{mineral}}{X_{Ca}^{melt}} \quad \text{Mod.3.2c} \quad \text{Wood and Blundy (2013)}$$

For the calculation of the partition coefficient, models Mod.3.2a, Mod.3.2b and Mod.3.2c must be integrated in the LSM with proxy equation (Eq.2.18).

3.3.3.3 LILE1

The models for LILE1 are from Blundy et al (1995). However, it appeared that the models proposed by this study tend to underestimate the partition coefficients for LILE1 (Figure 3.9). Therefore, I added a correction factor on the ideal ionic radius of +0.20Å instead of +0.12Å (see Mod.3.3a). The initial correction value from Blundy et al (1995) was approximated from the data of Law et al (2000) on a wollastonite pyroxene ($CaSiO_3$). Therefore, it is reasonable to assume that the ideal ionic radius for LILE1 in pyroxene approximates values greater than the one for Na (e.g., 1.18Å for 8-fold coordinated lattices) and lower than the one for K (e.g. 1.51Å CN8). The correction also has to take into account than D_K should remain smaller than D_{Na} since Na represents the most ideal behaviour for LILE1 in the M2 site of cpx (Blundy et al, 1995) since they can form the sodic pyroxene. The value of +0.20Å respects such conditions and allows to fit experimental data to the LSM within a correct range of error (Figure 3.9).

The ideal ionic radius is therefore written as:

$$r_0^{1+} = r_0^{3+} + 0.20 \quad \text{Mod.3.3a} \quad \text{Blundy et al (1995), This study}$$

Young's modulus follows the Hazen and Finger (1979) relationship (Figure 2.3):

$$E^{1+} = \frac{1}{3} \cdot E^{3+} \qquad \text{Mod.3.3b} \quad \text{Blundy et al (1995)}$$

For LILE1, Na is used as a proxy since it reflects the most ideal behaviour of a 1+ cation in the M2 site of cpx forming the jadeite endmember in Na-Al pyroxene modelled in this study. Although Na is a major element and can be determined by the Nernst partition coefficient, Blundy et al (1995) parametrised the model for LILE1 according to Mod.3.3c. Hence, model Mod.3.3c will be used in the modelling study:

$$LnD_{Na} = \frac{10367 + 2100 \cdot P - 165P^2}{T} - 10.27 + 0.36 \cdot P \qquad \text{Mod.3.3c} \quad \text{Blundy et al (1995)}$$
$$- 0.018 \cdot P^2$$

For the prediction of the partition coefficient, the models Mod.2.3a, Mod.2.3b and Mod.2.3c must be integrated in the LSM with proxy (Eq.2.18).

3.3.3.4 HFSE4

The models for HFSE4 are from Hill et al (2011). HFSE4 incorporate the 6-fold coordinated M1-site of cpx and therefore the appropriate 6-fold coordinated ionic radii have to be used in Eq.2.18 (Shannon, 1976).

The ideal ionic radius is given by:

$$r_0 = 0.64 - 0.008 \cdot P + 0.071 \cdot X_{Al}^{M1} \quad \text{Mod.3.4a} \quad \text{Hill et al (2011)}$$

Young's modulus is derived from a large amount of data on the M1 site of cpx (Hill et al, 2011 and reference therein) and is written as:

$$E = 10473 - 5.09 \cdot T - 201.54 \cdot P + 14633 \cdot Al^{iv} \quad \text{Mod.3.4b} \quad \text{Hill et al (2011)}$$

For HFSE4 cations, Ti is used as a proxy since the high values of E (e.g., up to 3687GPa; experiment 10P10; Hill et al, 2011) increase the tightness of the LSM curve (Blundy and Wood, 2003). This increases the amplitude of variation of D_0 leading to large uncertainties. If Ti is considered a major element, D_{Ti} can be found using the Nernst equation. If Ti is considered a trace element in the system, it is possible to measure the partition coefficient from the following model:

$$D_{Ti} = Y exp \left(\frac{46387 - 4257 \cdot P - 907 \cdot P^2}{RT} \right) \quad \text{Mod.3.4c} \quad \text{Hill et al (2011)}$$

with:

$$Y = [X^{4+}] + [X^{3+}] \, e^{\left(\frac{-\Delta G_{elec}^{cpx}}{RT} \right)} + [X^{2+}] \, e^{\left(\frac{-4\Delta G_{elec}^{cpx}}{RT} \right)} \quad \text{Eq.3.5}$$

where ΔG_{elec}^{cpx} represents the necessary energy for a cation of different valence to enter the M1 site of cpx. In the M1 site of cpx, ΔG_{elec}^{cpx} equates to (Wood and Blundy, 2001; Hill et al, 2011):

$$\Delta G_{elec}^{cpx} = 16.5 \; kJ$$

In Eq.3.5, $[X^{4+}]$, $[X^{3+}]$ and $[X^{2+}]$ are the amount of 4+, 3+ and 2+ cations in the M1 site of cpx and are calculated following the method of Wood and Blundy (2001) (Figure 10):

$$[X^{4+}] = \left[\left(Al^{iv}\right)^2 (1 - X_{1+}^{M2}) + 2 \cdot X_{1+}^{M2} \cdot Al^{iv} \cdot X_{Si} \right] \quad \text{Eq.3.6}$$

$$[X^{3+}] = \left[X_{1+}^{M2} \cdot (X_{Si})^2 + 2(1 - X_{1+}^{M2}) \cdot X_{Al}^{M1} \cdot X_{Si} \cdot Al^{iv} \right] \quad \text{Eq.3.7}$$

$$[X^{2+}] = [(1 - X_{1+}^{M2}) \cdot X_{Si}] \quad \text{Eq.3.8}$$

For the partition coefficient prediction, the models Mod.3.4a, Mod.3.4b and Mod.3.4c must be integrated in the LSM with proxy (Eq.2.18).

3.3.3.5 Scandium (TM)

The model for the transition metal Sc is also given by Hill et al (2011). As for HFSE4, Sc enters the structure of cpx preferentially in the M1 site.

$$D_{Sc} = L \exp \left(\frac{255646 - 149 \cdot T + 4233 \cdot P^2 - 2280 \cdot (Z_{Sc} - Z_0)^2}{RT} \right) \quad \text{Mod.3.5} \quad \text{Hill et al (2011)}$$

with L given as:

$$L = [X^{4+}] + ([X^{3+}] + [X^{2+}]) \, e^{\left(\frac{-\Delta G_{elec}^{cpx}}{RT}\right)} \quad \text{Eq.3.9}$$

(see section 3.2.3.4 for the definition of $[X^{4+}]$, $[X^{3+}]$, $[X^{2+}]$, and , ΔG_{elec}^{cpx}), and Z_0, as expressed by Blundy and Wood (2001) as the mean melt charge excluding the role of Si and Al in the melt and equates to:

$$Z_0 = \frac{\sum(X_{cation}^{melt} \cdot charge)}{\sum charges}$$

3.3.3.6 Actinides

The models for actinides are from Landwehr et al (2001). Actinides are 4+ cations but, unlike HFSE4, their ionic radii are too large for the M1-site of cpx. Hence, actinides enter the 8-fold coordinated M2-site of cpx, and therefore the appropriate 8-fold coordinated ionic radii have to be used in Eq.2.18 (Wood et al, 1999; Shannon, 1976).

The ideal ionic radius for actinides is equal to the ones for REE due to similar ionic radii between these elements (e.g., U (CN8) = 1Å, which is similar to the radius of Yb(CN8) = 1.004 Å). The model used is therefore:

$$r_0^{4+} = r_0^{3+} \quad \text{Mod.3.6a} \quad \text{Wood et al, 1999}$$

Young's modulus is considered to follow the Hazen and Finger (1979) relationship in the M2 site of cpx (Figure 2.3):

$$E^{4+} = \frac{4}{3} \cdot E^{3+} \quad \text{Mod.3.6b} \quad \text{Wood and Blundy (2013)}$$

There are no other 4+ cations in the M2 site of cpx, and therefore a quantitative investigation of Act-bearing pyroxene is needed to constrain a proxy for the determination of the actinide behaviour. Here, Th was used as a proxy by Landwehr et al (2001). Using the quantitative development for Th exchange between cpx and melt (c.f.2.2.2.1), they propose the following model for D_{Th}:

$$D_{Th} = \frac{\gamma_{Th}^{M2} \cdot X_{Mg}^{M1} \cdot \gamma_{Mg}^{M1}}{X_{Mg}^{Melt}} \\ \cdot exp\left(\frac{214.79 - 0.757 \cdot T + 16.42 \cdot P - 1.50 \cdot P^2}{RT}\right) \quad \text{Mod.2.6c} \quad \text{Landwehr et al (2001)}$$

With γ_{Th}^{M2} the activity coefficient of thorium in Th-bearing cpx:

$$\gamma_{Th}^{M2} = exp\left[\frac{-4 \cdot \pi \cdot N_A \cdot E_{M1}^{4+\cdot}}{R \cdot T} \cdot \left(\frac{r_0^{4+}}{2} \cdot (r_{Th} - r_0^{4+})^2 + \frac{1}{3} \cdot (r_{Th} - r_0^{4+})^3\right)\right] \quad \text{Eq.3.6}$$

And γ_{Mg}^{M1} is the activity coefficient of Mg in Th-bearing cpx:

$$\gamma_{Mg}^{M1} = \left(\frac{7500}{RT}\right) \quad \text{Eq.3.10}$$

Hence, D_{Th} can be used as a proxy for r_0 and E of actinides, and values have to be added to Eq.2.18 to derive D_i.

3.3.4   Regressions analysis

Since all the other elements can be modelled using the LSM, only the HFSE5 needs to be parametrised via regression analyses. Like the behaviour of HFSE5 in opx, Wood and Blundy (2013) find that the local charge imposed by the amount of Al^{iv} controls the behaviour of these elements. For example, for Ta:

$$LnD_{Ta} = -2.127 + 3.769 \cdot Al^{iv} \quad \text{Mod.3.7a} \quad \text{Wood and Blundy (2013)}$$

Also, like opx, the behaviour of Nb is closely related to the one of Ta since cpx does not show any fractionation process between HFSE5 (Foley et al, 2002, Bédard, 2007). So a predictive model for Nb is given by:

$$D_{Nb} = 0.003 + 0.292 \cdot D_{Ta} \quad \text{Mod.3.7b} \quad \text{Wood and Blundy (2013)}$$

Like in opx, HFSE5 enter exclusively the M1 site and it is therefore reasonable to use Mod.2.7a and Mod.2.7b, since Al^{iv} is a proxy for heterovalent substitution.

3.4 Case 4: amphibole (amph)

Amphibole is a hydrous mafic mineral common in many magmatic/metamorphic rocks that experienced melting, metamorphism, or metasomatism in a hydrous environment. Amphibole is found in various shapes from high pressure - low temperature melting reactions with hornblende-like amphibole (Wolf and Wyllie, 1994, Qian and Hermann, 2013) to the settings of hydrothermal fluids with riebeckite-like amphibole (Chao et al, 1992). Water-bearing amphibole plays a major role in the creation of evolved SiO_2-rich magmas in arc settings (Nandedkar et al, 2014, Wolf and Wyllie, 1994; Alonzo-Perez et al, 2009) and trace element behaviour in amphibole provides valuable insights in the understanding of amphibole fractionation processes (Davidson et al, 2007; Qian and Hermann, 2013; Nandedkar et al, 2016, Tiepolo et al, 2007).

In this study, hydrous calcic amphibole (mostly Pargasite, Kaersutite, Richterite, Tschermakite) will be investigated, as they are more representative of large scale magmatic processes such as lower crustal differentiation in fluids-rich environments (e.g., subduction zones) (Bouilhol et al, 2015; Alonzo-Perez et al, 2009; Nandedkar et al, 2014, Wolf and Wyllie, 1994; Rapp et al, 1991; Rushmer, 1991). Amphiboles of this kind have specific signatures that put constraints on magma petrogenesis, magma pathways and continental building (Davidson et al, 2006; Foley et al, 2002,

Foley et al, 1999). Such signatures are the high Dy/Yb ratio (MREE/HREE) due to a high affinity for Dy in Ca-amph, or the fractionation of Nb from Ta in low magnesium Ca-amphibole (Foley et al, 2004) (see Figure 3.1).

3.4.1 Structure of amph

Ca-amphiboles have a wide range of compositions, leading to highly variable crystal structures and complexities. For the Ca-amph group, 9 different monoclinic networks can be found and are gathered in one symmetry group called C2/m (Hawthorne and Oberti, 2007). An example of amphibole structure is presented in Figure 3.10. From this symmetric structure, Ca-amphs have up to seven different cation sites in their structure and can be written as follows in terms of cation ordering (Hawthorne and Oberti, 2007; Leake et al, 1997; Bottazzi et al, 1999; Tiepolo et al, 2000a):

$$A_{(Na,K)}M4_{(Ca,Na,Mg,Fe)}M3_{(Mg,Fe)}M2_{(Al,Ti)}M1_{(Mg,Fe)}T1_{Si}T2_{(Si,Al)} - (O, OH, F, Cl) \quad \text{Str.3a}$$
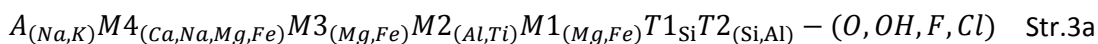
where A is the "cavity" 12-fold coordinated site of amphibole, M4 the 8-fold coordinated site, M3, M2 and M1 are the 6-fold coordinated octahedral sites, and T1 and T2 the 4-fold coordinated tetrahedral sites of Ca-amphibole (Figure 3.10). For the structural formula calculation, the notation Str.3a can be simplified (Leake et al, 1997):

$$A_{0-1}B_{(2)}C_{(5)}T_{(8)} - (O, OH, F, Cl)_{24} \quad \text{Str.3b}$$
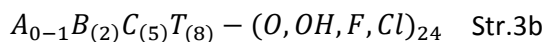
where A is a A site, B is the M4 site, C are the M1, M2 and M3 sites, and T are the T1 and T2 sites. Site occupancy of trace elements in Ca-amph is described as (Dalpé and Baker, 2000, Bottazzi et al, 1999, Foley et al, 1999):

$$A_{(LILE1)}M4_{(LILE2,REE,TM)}M3_{(HFSE5)}M2_{(HFSE4)}M1_{(HFSE5)}T1_{Si}T2_{(Si,Al)} - (O, OH, F, Cl) \quad \text{Str.3c}$$
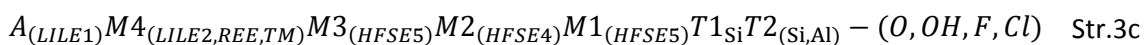
The trace element ordering shown in Str.3c illustrates that the trace element behaviour in amphibole is not straightforward and might depend on several variables. In the next section, it is shown that trace element behaviour can be determined from other compositional proxies.
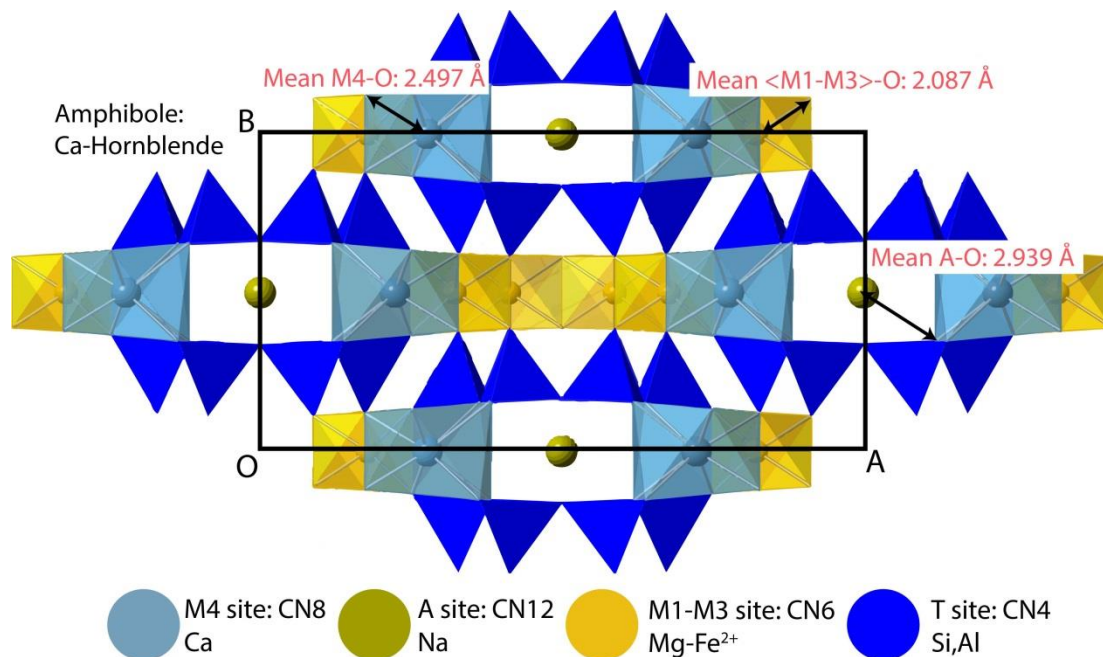
Figure 3-9: OAB view of the structure of a monoclinic Ca-Hornblende with space group C2/m from Makino and Tomika (1989). Mean atomic bond lengths data (<M>-O) representing the size of the lattices are from Hawthorne and Oberti (2007). This figure shows an example of distribution and lattice sizes in Ca-Amphibole. The A site is a "cavity" and can incorporate really large cations (LILE1 + Ba). Other sites are the chained polyhedrons, which are smaller in size.

3.4.2   Trace element controlling parameters in amphibole

The behaviour of trace elements in amphibole is widely discussed in the bibliography since the complexity of amphibole leads to complex interrelationship between the various cation sites and the nature of occupying cations (Nandedkar et al, 2016; Tiepolo et al, 2007; Dalpé and Baker, 2000; Bottazzi et al;, 1999). Indeed, the site deformation (which provides information on the lattice strain parameters) will depend on the behaviour of each lattice site and the amount of major cations within these lattices. This represents many variables for the derivation of predictive models for lattice strain parameters, and the scientific community has not yet been able to derive such model.

However, it is now accepted that trace element behaviour in Ca-amphibole is, to some extent, controlled by the melt polymerisation state (Nandedkar et al; 2016; Tiepolo et al, 2000a; Tiepolo et al, 2007). There is a simple approximation suggesting a linear increase of polymerisation with the amount of silica in the melt. This linear trend can be observed by fitting the data of Tiepolo et al (2007) against the Si-content of the melt (Figure 3.11) and give the following equation that will be used in the modelling part of this study:

$$\frac{Xnf}{X} = 0.008458 \cdot C_{SiO_2}^{melt} + 0.1734 \quad r^2 = 0.85 \qquad Eq.3.11$$

with $\frac{X_{nf}}{X}$ being the notation for polymerisation state from Nielsen and Dungan (1983) (X_{nf} denotes the molar composition of network-forming cations (Si and Al), and X denotes the molar composition of the total amount of cations in the melt).

Therefore, the partition coefficient can be approximated as being Si-melt dependent. Some studies state that melt polymerisation and/or SiO$_2$ content in the melt can be used to derive lattice strain parameters predictive models for amphibole (Nandedkar et al, 2016), although this has not been attempted in this study. Note that the $\frac{X_{nf}}{X}$ polymerisation term is a simplification of the work of Mysen et al (1982), who considered more elements as being network forming cations in the melt such as Ti. However, for Amphibole predictive models, it appears that only the abundance of Al and Si quasi-lattices plays a major role in the incorporation of trace elements in the mineral structure (Tiepolo et al, 2000a).
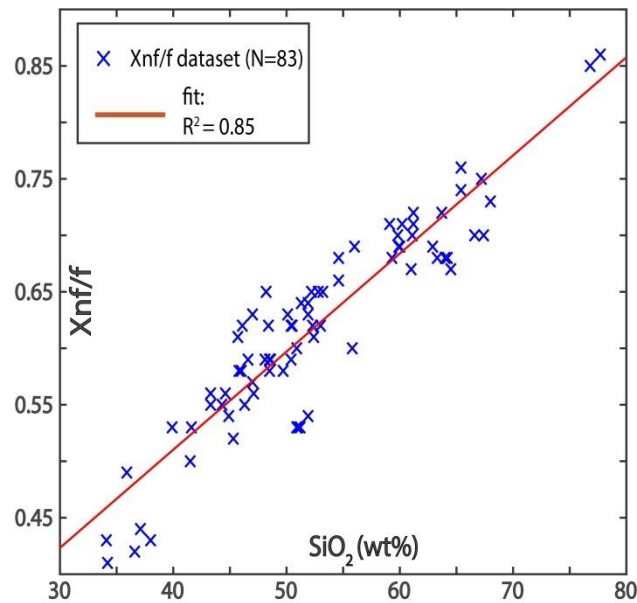
Figure 3-10: *Regression analyses work for amphibole partition coefficient models. Data points are from Tiepolo et al (2007). A linear trend between melt polymerisation and the $C_{SiO_2}^{melt}$ (wt%) suggests that the silica content in the melt is the main factor controlling the melt polymerisation. In other words, more silica in the melt means more Si and Al quasi-lattices (see text). The best fit equation results in Eq.3.11.*

3.4.3   LSM

The lattice strain parameters for amphibole have been chosen from the work of Dalpé and Baker (2000). The data presented in Table 2 give the lattice strain parameter used in this study from the experimental work of Dalpé and Baker (2000) on pargasite amphibole at various pressure,

temperature and oxygen fugacity conditions (cf., Table 5 and Table 6 of Dalpé and Baker, 2000 on calculated lattice-site parameters). Although these values have to be revised for more accurate models, they can reproduce well the data from the bibliography (cf, Chapter 4), and were preferred over the models of Nandedkar et al (2016) and Tiepolo et al (2007). This choice is due to the fact that pressure is the dominant parameter that controls the behaviour of LILE1 and Ba in amphibole (Tiepolo et al, 2007; Dalpé and Baker, 2000) and that the polymerisation state model of Tiepolo et al (2007) and the Ca partitioning between amphibole and melt models of Nandedkar et al (2016) do not consider the variation of pressure. Indeed, while looking at Figure 3.10, it is coherent that the cavity site A is most subject to variation in volume due to the applied pressure. This variation of volume significantly affects the type of cation that can be hosted in the cavity.

Also, for HFSE4 and HFSE5, Tiepolo et al (2007) argue that there are no correlations with polymerisation state for high values of $\frac{X_{nf}}{X}$ ($\frac{X_{nf}}{X} \sim 0.65$ that translated to SiO_2 content using eq.3.11 gives ~ 65 wt%). This is due to crystal chemical control and other environmental parameters such as water fugacity that regulate the behaviour of these elements in amphibole (Tiepolo et al, 2007; Dalpé and Baker, 2000). Therefore, for high value of polymerisation state, the use of the LSM from Dalpé and Baker (2000) Mod.4.1d and Mod.4.1e are preferred with respect to the other models. However, more work on the quantification of HFSE4 and HFSE5 behaviour in amphibole is required to correctly model these elements.

Table 3: Lattice strain parameters derived from the experiments of Dalpé and Baker (2000). The A-site values for 1+ cations (LILE1) and the M2-site values (HFSE4) are averaged using the calculated lattice strain parameters on experiments of Dalpé and Baker (2000) using Table 6 of these authors' paper. The M1-site values (HFSE5) and A-site values for 2+ cation (Ba) are directly taken out from Table 5 of Dalpé and Baker (2000).

Trace elements	r_0(Å)	E(GPa)	D_0	Condition	Model
Cs, Rb, K (CN12)	1.52	86.75	2.99	n/a	Mod.4.1a
Ba (CN12)	1.52	315	1.6	n/a	Mod.4.1b
HFSE4 (CN6)	0.65	1393.2	1.27	$if\ SiO_2^{Melt} > 65$wt%	Mod.4.1c*
HFSE5 (CN6)	0.73	1985	2.16	$if\ SiO_2^{Melt} > 65$wt%	Mod.4.1d*

* models for mafic and intermediate melts are presented in Table 4

It is important to note that LILE1 and Ba enter the A site of amphibole so that 12-fold coordinated ionic radii must be used to calculate partition coefficients with the LSM equation (Eq.2.11). For Sr, the coordination is 8, and for HFSE4 and HFSE5, the coordination is 6.

3.4.4 Regressions analysis

3.4.4.1 Strontium (Sr)

For strontium, the model of Nandedkar et al (2016) was used. The use of this model gives more accuracy in trace element modelling (cf., Chap.4). The model is noted as follows:

$$D_{Sr} = \exp(0.51 . \log(D_{Ca}) - 0.998) \qquad \text{Mod.4.2} \qquad \text{Nandedkar et al (2016)}$$

With D_{Ca} the partition coefficient of Ca between amphibole and melt.

3.4.4.2 HFSE4, HFSE5, Actinides and Scandium

As stated before, the behaviour of trace elements in amphibole is better predicted by the melt polymerisation. The work of Tiepolo et al (2007) provides a full study of predictive models for the partition coefficient versus $\frac{X_{nf}}{X}$. These authors observed that partition coefficients for actinides and transition metals follow an exponential trend versus melt polymerisation:

$$D_{TE} = a_{TE} \, exp\left(\frac{Xnf}{X} \cdot b_{TE}\right) \qquad \text{Mod.4.3} \qquad \text{Tiepolo et al (2007)}$$

The coefficient a_{TE} and b_{TE} are fitting coefficients determined by Tiepolo et al (2007) and listed in Table 3. For HFSE4 and HFSE5, partition coefficients also follow Mod.3.2 but only for basaltic and intermediate melts ($SiO_2^{Melt} < 65$ wt%) (cf.3.4.3).

Table 4: Set of coefficients for the Tiepolo et al (2007) models (see text: Mod.4.3)

Trace elements	a_{TE}	b_{TE}	Trace elements	a_{TE}	b_{TE}
Sc	0.0169	9.33	U	9e-6	12.15
Ti*	0.0273	6.9531	Th	1e-5	12.24
Hf*	0.0035	8.894	Nb*	6.5e-6	18.46
Zr*	0.001493	9.352	Ta* $D_{Ta} = D_{Nb} . (D_{TE})$	3.48e-5	16.51

* Models for felsic melts are presented in Table 3

3.4.4.3 REE + Y

Predictive models for REE are also from Tiepolo et al (2007). However, no model is available for Pr, Tb and Tm, so not the entire series of REE can be modelled. Therefore, this study converted

the $\frac{X_{nf}}{X}$ data from Tiepolo et al (2007) to a SiO$_2$-content using Eq.3.11 and proposes a new set of coefficients for REE partitioning in amphibole using regression analyses. The result of this fitting procedure is an exponential relationship similar to Mod.4.2, but a function of SiO2 content in the melt, such as:

$$D_{REE} = a_{REE}\, exp\big(C_{SiO_2}^{melt} \cdot b_{REE}\big) \quad \text{Mod.4.4} \quad \text{Tiepolo et al (2007), This study}$$

Table 5: Set of coefficients for the revisited models of Tiepolo et al (2007). (See text: Mod.4.3)

Trace elements	a_{REE}	b_{REE}	Trace elements	a_{REE}	b_{REE}	Trace elements	a_{REE}	b_{REE}
La	0.0135	0.0478	Eu	0.0445	0.0607	Ho	0.0496	0.06
Ce	0.0194	0.0194	Gd	0.0466	0.0606	Er	0.0495	0.0597
Pr	0.0266	0.0596	Tb	0.0482	0.0605	Tm	0.0491	0.0593
Nd	0.0388	0.0607	Dy	0.0492	0.0603	Yb	0.0485	0.0589
Sm	0.0417	0.0607	Y	0.0495	0.0601	Lu	0.0478	0.0585
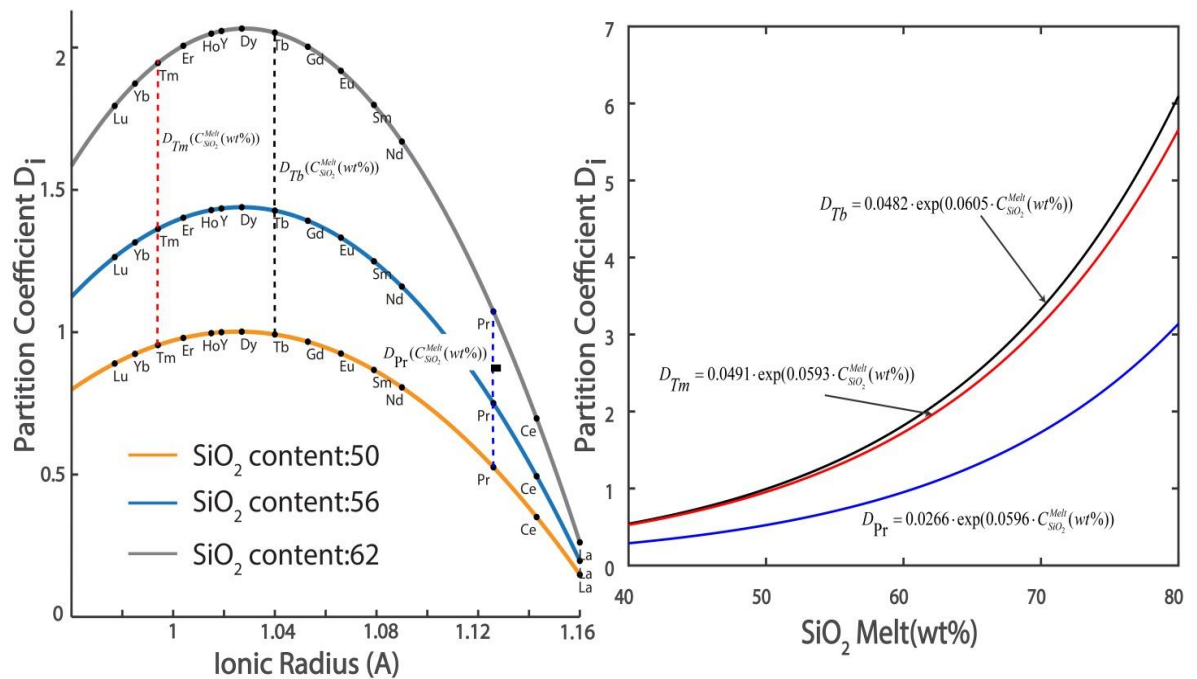
Figure 3-11: *Fitting procedure for the new set of coefficients for REE in amphibole (Mod.3.3a). Data are also from Tiepolo et al (2007). Partition coefficient vs $\frac{X_{nf}}{X}$ were converted to partition coefficient vs SiO$_2$ using Eq.3.2. **Left figure:** example of partition coefficient evolution vs Ionic radius at different silica content in the melt. The size of substituting cation plays an important role in the partition coefficient behaviour in amphibole. The dashed lines are the representation of Di vs SiO$_2$ drawn on the right figure. **Right figure:** Di vs SiO$_2$ for the three missing elements of Tiepolo et al (2007) models, namely Pr, Tm and Tb.*

To determine the coefficients, this work assumes that the lattice strain theory is applicable to the M4 site of amphibole, leading to a relationship of partition coefficient vs ionic radius of

substituting elements (Bottazzi et al, 1999; Dalpé and Baker., 2000). This offers a second dependency with which the partition coefficient can be constrained. Converting $\frac{X_{nf}}{X}$ to C_{SiO2}^{Melt} with Eq.3.11 and using the lattice strain theory for each of the REE provides a new set of fitting coefficients presented in Table 5. Figure 3.12 shows an example of the fitting procedure for Mod.4.3 for the new set of coefficients.

These models were preferred over the one of Nandedkar et al (2016) since they reproduce more accurately the trace element partition coefficients from experimental studies (cf., Chapter 4.2).

3.5 Case 5: garnet (gt)

Garnet is a mineral common in metamorphic/magmatic reactions and is a marker of high pressure conditions. The presence of garnet is recorded in a wide range of geological conditions and represents a special interest for geodynamical studies. Firstly, garnet-bearing rocks give insights not only in the conditions of pressure, temperature and compositional variation of a system but also on the prograde and retrograde paths of geological materials, which are shown by zonations in garnet (Baxter and Scherer, 2013; van Breemen and Hawkesworth, 1980). These zonations, related to the variability of crystal composition from core to rim, are particularly useful to determine the prograde paths in metamorphic environments (Dragovic et al, 2012; Viete et al, 2011a; Riel et al, 2016). Secondly, garnet-bearing magmatic cumulates indicate drastic changes in the regional density, participating, for example, to the delamination of the lower arc crust (Jagoutz et al, 2011; Jagoutz et al, 2006; Ducea and Saleeby, 1998a).

Finally, the role of garnet in the formation of mid-ocean ridges basalt is still a matter of debate. On a one hand, some authors argue that the role of garnet is essential to explain typical signatures of MORB such as the Lu/Hf paradox or the evolution of the Sm/Nd ratio
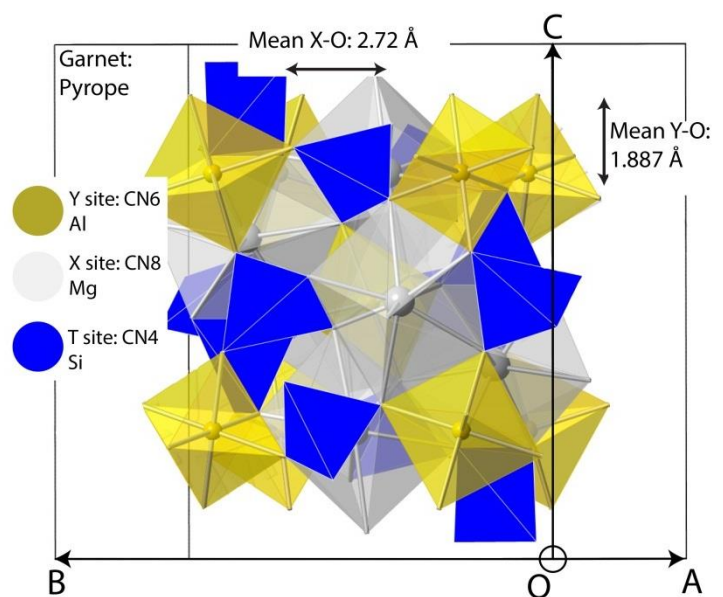
Figure 3-12: *Structure of pyrope garnet crystallising in the cubic system and with a space group Ia3d creating one small octahedral site Y and one large dodecahedral site X. Tetrahedrons in garnet are not connected to each other and are so called orthosilicate. Mean atomic bond lengths show the size of the lattices. The larger X site may accept more trace elements than the Y site. Structure data and mean atomic bond lengths are from Novak and Gibbs (1971).*

(Hellebrand et al, 2002; Salters and Hart, 1989), assuming that the depths of melting in the ridge axis occurs in the garnet stability field (~90km). This was tested by a numerical model of porous flow in mid ocean ridges at 95km depth whereby melt genesis in the garnet stability field correlates with melt production and stacking in the uppermost ridge axis (Tirone et al, 2012). On the other hand, extensive compilation of natural samples (Warren, 2016), modelling of trace element behaviour in cpx on the spinel lherzolite solidus (Blundy et al, 1998), or experimental observation of pervasive flow in abyssal peridotites (Lissenberg and Mcleod, 2016) led to the conclusion that melt genesis does not occur in the garnet stability field and that other phases can explain MORB signatures. A garnet signature in the melt is manifested through the affinity of HREE to enter garnet crystals, which results in melts that are depleted in such elements and in a high La/Yb ratio (LREE/HREE) (Shen and Forsyth, 1995) (see Figure 3.1).
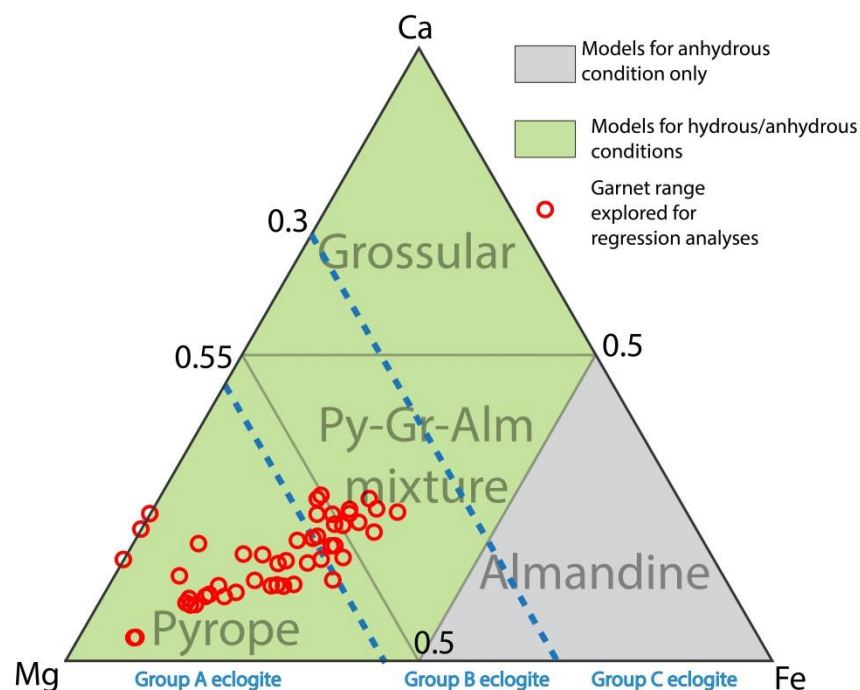
Figure 3-13: *Ternary plot of natural garnet excluding the other major garnet Spessartine and Andradtite (see text). Green shaded areas show the garnet range for which predictive models are provided. Grey shaded area shows that the model provided for Fe-rich garnet is limited to anhydrous conditions (see text, Draper and van Westrenen, 2007). Group A, B and C eclogites show that garnet compositions inform on the geodynamical context (Coleman et al, 1965). Group A eclogites are garnet that crystallise in ultramafic peridotites or dunites (ultra-high pressure mantle conditions). Group B eclogites are garnet that form in intra-crustal ultra-high pressure and temperature conditions (migmatites, metapelites). Group C eclogites are garnet from amphibolite/ granulite conditions. Red data points show the range of garnet used for regression analyses. Used literature is listed in Table 5.*

3.5.1   Structure of gt

The understanding of the general structure of garnet is essential to decipher the trace element behaviour in this mineral. Moreover, the knowledge of the different end-members as well as the conditions in which they occur is important for the following application chapter.

Garnets are orthosilicates with a common symmetry group called *Ia3d* (Figure 3.13). This structure has two distinctive sites for network modifying cations and the common tetrahedral site. The general formula is:

$$X_{(Mg,Fe,Ca,Mn)_3} Y_{(Al,Cr,Fe^{3+})_2} T_{(Si,Al)_3} - O_{12} \quad \text{Str.5a}$$
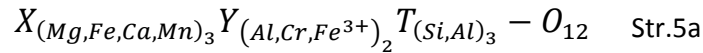
In structure Str.5a, X is the 8-fold coordinated site equivalent to the M2 site of pyroxene, Y the 6-fold coordinated site equivalent of the M1 site of pyroxene and T the tetrahedral site. Unlike the chain silicate pyroxene, orthosilicates do not share edges with other tetrahedrons. Garnet minerals can be subdivided into two main groups. The first and most represented one is the Pyralspite group that has exclusively Al in the Y site. Among this group are the pyrope (Py: $Mg_3Al_2Si_3O_{12}$), almandine (Alm: $Fe^{2+}_3Al_2Si_3O_{12}$), grossular (Gr: $Ca_3Al_2Si_3O_{12}$) and spessartine (Spess: $Mn_3Al_2Si_3O_{12}$) garnet that are the main phases in many geological processes and are used to categorise the three groups of eclogites (Figure 3.14). Pyrope-rich garnet is the most common phase of garnet under upper mantle conditions (Adam and Green, 2006; van Westrenen and Draper, 2007) such as mid-ocean ridges, while almandine garnet is a common phase under lower crust conditions, such as in arc settings (Narduzzi et al, 2017; Williams et al, 2014). The second is the ugrandite group with exclusively Ca in the X site. In this group we can find, for example, andratite (And: $Ca_3Fe^{3+}_2Si_3O_{12}$) and Urarovite (Ura: $Ca_3Cr_2Si_3O_{12}$) garnet and appear only in specific conditions such as oxidised melt and Cr rich environment. These are the garnet end-members. Therefore, a single notation can encompass the composition of garnet:

$$X_{Py} X_{Alm+Spess} X_{Gr+And} \quad \text{Str.5b}$$
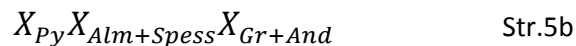
in which X denotes the fraction of a specific kind of garnet. For example, the molar fraction of pyrope X_{Py} can be calculated as:

$$X_{Py} = \frac{X_{Mg}}{(X_{Mg} + X_{Ca+Fe^{3+}} X_{Fe^{2+}+Mn})} \quad \text{Eq.3.12}$$

where X is the molar concentration of the indicated elements in garnet. For the sake of this study, only Py, Gr and Alm will be considered since Cr, Mn and Fe^{3+} are not part of the chemical space investigated in the modelling part ($X_{Spess} = 0$, $X_{Ura} = 0$ $X_{And} = 0$). However, the incorporation of these end-members can be added in further studies.

In terms of trace elements, like for other minerals, garnet preferentially incorporates some trace elements in the X site, while others prefer to enter the Y site:

$$X_{(REE,Sc,Act,LILE1,LILE2,HFSE4)_3}Y_{(HFSE4,HFSE5,Sc)_2}T_{(Si,Al)_3} - O_{12}$$ Str.5c

Unlike other minerals, HFSE4 can be incorporated in the large X site of garnet under specific conditions that will be presented in the next section.

3.5.2   Trace element controlling parameters

Str.4a shows that the X site of garnet requires 3 cations per formula unit to balance the structure. Therefore, the variation of amount of Ca, Fe or Mg is the main proxy to calibrate models for partition coefficients as they are the main cations hosted in the X lattice. Several studies were done on the control of various compositional parameters on the X site of garnet (van Westrenen et al, 1999; van Westrenen et al, 2001a, Draper and van Westrenen, 2007, Sun and Liang, 2013a). It appears that the variation of Ca content in the X lattice controls the behaviour of the trace elements (Sun and Liang, 2013a). Indeed, the presence of Ca indicates potential lattice conditions suitable for trace element substitution. However, in Fe-rich garnet, Draper and van Westrenen (2007) and van Westrenen et al (2000, 1999) observed that the amount of Fe^{2+} significantly decreases the partition coefficient. This suggests using Fe as a compositional proxy in Fe-rich garnet, although these studies argue that the presented model is not able to reproduce natural and experimental data of partition coefficient under hydrous conditions (van Westrenen and Draper, 2007).

One particularity of garnet is that the very stiff Y site is almost insensitive to the compositional variation within the larger X site (Geller, 1967; van Westrenen et al, 2000). It turn, the variations of lattice characteristics in the X site are not dependent to the Y site variation, which differ from pyroxene. Therefore, the amount of cations in the octahedral Y-site, which is a useful proxy for the partition coefficient prediction in pyroxene, is not useful here. However, van Westrenen et al (2001b) proposed that in a specific range of X_{Gr} composition (i.e., $0.19 < X_{Gr} < 0.4$), Hf, Zr and Sc are able to enter both the X and Y sites of garnet.

3.5.3   LSM

3.5.3.1 REE + Y

The models for REE in garnet are from Sun and Liang (2013a). They compiled data for REE partition coefficients in garnet that cover the eclogite A and eclogite B groups (Figure 3.14). Their models propose more accurate partition coefficient data for Py-rich garnet.

The ideal ionic radius is written as:

$$r_0 = 0.780 + 0.155 \cdot X_{Ca} \quad \text{Mod.5.1a} \quad \text{Sun and Liang (2013a)}$$

Young's modulus relationship is only dependent on the ideal ionic radius:

$$E = [-1.62 + 2.29 \cdot r_0] \cdot 10^3 \quad \text{Mod.5.1b} \quad \text{Sun and Liang (2013a)}$$

Finally, the strain-free partition coefficient is written as:

$$lnD_0 = -2.05 + \frac{91700 - 91.35 \cdot P(38 - P)}{RT} - 1.02 \cdot X_{Ca} \qquad \text{Mod.5.1c} \qquad \text{Sun and Liang (2013a)}$$

For the prediction of partition coefficients for REE+Y, models Mod.5.1a, Mod.5.1b and Mod.5.1c must be integrated in the LSM equation (Eq.2.11).

3.5.3.2 LILE2

The models for LILE2 in garnet are used from van Westrenen et al (2001a).

The ideal ionic radius is written as:

$$r_0^{2+} = r_0^{3+} + 0.053 \quad \text{Mod.5.2a} \quad \text{van Westrenen et al (2001a)}$$

Young's modulus follows the Hazen and Finger (1979) relationship (Figure 2.3):

$$E^{2+} = \frac{2}{3} \cdot E^{3+} \quad \text{Mod.5.2b} \quad \text{van Westrenen et al (2001a)}$$

Finally, in pyrope garnet, Mg has the most ideal behaviour and can be used as a proxy to derive partition coefficient information for LILE2. Therefore, for pyrope, van Westrenen (2001a) give the following predictive model for D_{Mg}:

$$D_{Mg} = \frac{exp\left(\frac{(258210 - 141.5\,T + 5418\,P)}{3\,RT}\right)}{exp\left(\frac{(19000\,X_{Ca}^2)}{RT}\right)} \qquad \text{Mod.5.2c} \quad \text{van Westrenen et al (2001a)}$$

However, one would anticipate that the most ideal behaviour is dependent to the dominant end-member in garnet, which is not always pyrope. Indeed, other garnet such as the Gr-rich or Alm-rich ones have Ca and Fe as the major constituent of the X site, respectively. So the ideal proxy element for LILE2 will change with the composition of the X site (van Westrenen et al, 2007). These compositional variations have not been investigated in this study, but would improve the

predictive model for LILE2. For partition coefficient predictions for LILE2, models Mod.5.2a, Mod.5.2b and Mod.5.2c must be integrated in the LSM with proxy equation (Eq.2.18).

3.5.3.3 HFSE4

The models for HFSE4 are from the semi-empirical models of van Westrenen et al (2001b). Hf and Zr substitute in the Y site of garnet but are also entering the X site in specific conditions (e.g., $0.19 < X_{Gr} < 0.4$), leading to a double substitution mechanism. The models presented here propose a means to calculate the double substitution of Hf and Zr. Accounting for the change in X_{Gr}, the LSM is used to predict the amount of HFSE4 in both the X and Y site in accordance with the change in coordination (X site = CN8; Y site = CN6). Outside of this range, only substitution in the Y site is considered, such that:

$$if \ 0.19 < \ X_{Gr} < 0.4 \qquad D_{HFSE4} = D_{HFSE4}(CN6) + D_{Hf,Zr}(CN8)$$

$$if \ X_{Gr} > 0.4 \qquad\qquad\qquad\qquad\qquad\qquad\qquad\qquad\qquad Eq.3.11$$
$$andor \qquad\qquad D_{HFSE4} = D_{HFSE4}(CN6)$$
$$if \ X_{Gr} < 0.19$$

With X_{Gr} the fraction of grossular garnet calculated using Eq.3.12 and D_{HFSE4} the partition coefficient of HFSE4.

However, van Westrenen et al (2001b) propose to use two different proxies when the X_{Gr} condition is respected, which are D_{Ti} for the Y site and D_{Th} for the X site since both are 4+ cations thought to represent the most ideal behaviour of 4+ cation in garnet. While a model for D_{Th} exists in the bibliography and is presented in the following sub-section (cf.,Chapter 3.5.3.4), no model is given for D_{Ti}. Therefore, this study will propose a model of D_{Ti} , constrained from literature data listed in Table 5. Moreover, no model for Young's modulus is available for the Y site of garnet, and this study also proposes a model to calculate that (Figure 3.15).

The ideal ionic radii for HFSE4 in the X site ($r_0^{4+}{}_X$) and HFSE4 in the Y site ($r_0^{4+}{}_Y$) are given as follows:

$$r_0^{4+}{}_X = r_0^{3+}{}_X - 0.05 \qquad\qquad\qquad van \ Westrenen \ et \ al \ (2001b)$$
$$\qquad\qquad\qquad\qquad Mod.5.3a$$
$$r_0^{4+}{}_Y = 0.67$$

The lack of experimental data on Young's modulus led van Westrenen et al (2001b) to propose a constant for HFSE4 in the X site. For the Y site, 4 data points were given for 4 different X_{Gr}. These data are used to propose a model of variation of Young's modulus according to the variation in X_{Gr} content (Figure 3.15).

The models are given as follows:

$$E_X^{4+} = 1325 \text{ GPa}$$

$$E_Y^{4+}(GPa) =$$

$$15870 \, exp\left(-0.1086 \, . \, X_{Gr \, (\%)}\right) \qquad \text{Mod.5.3b} \qquad \text{This study}$$

$$+409.6 \, exp\left(0.01191 \, . \, X_{Gr \, (\%)}\right)$$

$$r^2 = 0.99$$

where $X_{Gr(\%)}$ is the amount of grossular in percent.
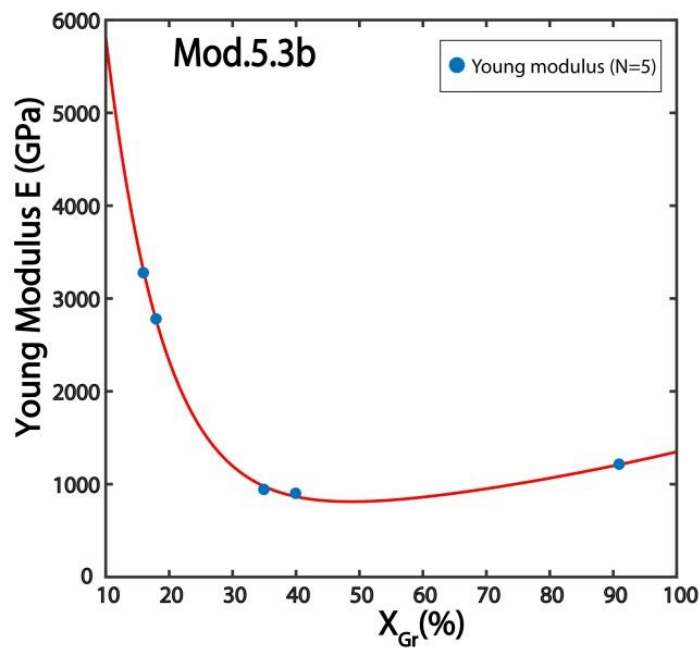
Figure 3-14: *Young's modulus versus XGr (%) in the Y site of garnet for 4+ cations. Regressions made on 5 data points from van Westrenen et al (2001b) giving Mod.4.3b. These data shows that while the condition $0.19 < X_{Gr} < 0.4$ is respected, Young's modulus critically decreases in the Y site. This suggests that over this range of garnet compositions, the elastic properties of the mineral vary considerably.*

Following the suggestion of van Westrenen et al (2001b), Ti is used as a proxy for the prediction of other HFSE4 in the Y site, and Th is used as a proxy for the Hf and Zr cations entering the X site. However, while studies were done to constrain the partition coefficient of actinides in garnet (Salters and Longhi, 2002), none or very few studies worked on the partitioning of Ti. In the attempt to have an accurate model of trace elements partitioning, this study investigates different parameters that might control the variation of D_{Ti}. Therefore, a set of partition coefficients from experiments under various pressures and temperatures and a large range of garnet and melt compositions have been collected to create predictive models for D_{Ti} (Table 5). Multiple regression analyses were attempted for several controlling factors

$(X_{Gr}, X_{Py}, X_{Alm}, X_{Ca}, X_{Mg}, X_{Fe}$, P, T and $\frac{X_{nf}}{X}$), and the best fitting product results in the following equation (Figure 3.16):

$$D_{Ti} = 0.0037 \cdot exp\left(7.386 \cdot \frac{Xnf}{X}\right)$$

$$r^2 = 0.53$$

Mod.5.3c   This study

in which $\frac{Xnf}{X}$ is the melt polymerization as calculated using Eq.3.11. Ti can substitute Si in the tetrahedral site, and therefore the partitioning of Ti is not only limited to the Y site of garnet (Huggins et al, 1977). It is therefore interesting to observe than D_{Ti} in garnet is dependent on the polymerization of the melt, confirming that the cation Ti is a network-forming cation in alumino-silicate melts (Mysen et al, 1982). However, this observation highlights the fact that Ti substitutes in both tetrahedral and octahedral coordination, in the T and X sites, respectively. It is likely that the scatter in Figure 3.16 is partly caused by this double substitution. Therefore, the use of the Mod.5.3c as a proxy for D_{Hf} and D_{Zr} will lead to an overestimation of these partition coefficients in the Y site since $D_{Ti} = D_{Ti}(CN6) + D_{Ti}(CN4)$. Further studies are necessary to quantify the D_{Ti} $(CN6)$ in garnet to improve the predictive models for HFSE4.
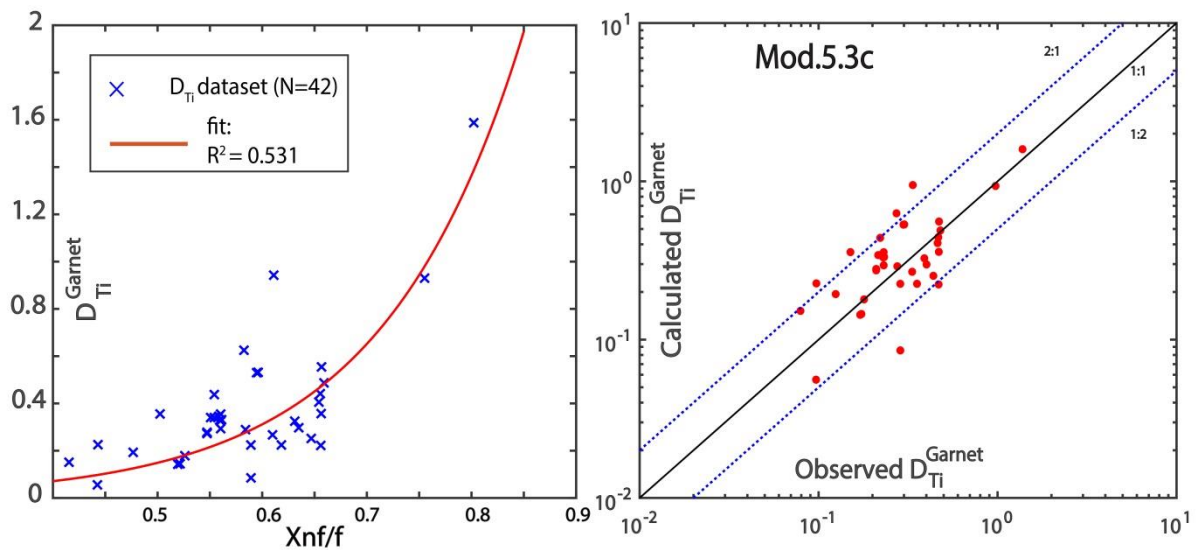
Figure 3-15: *Results for the regression analyses for D_{Ti} in garnet. The behaviour of Ti in garnet seems strongly dependent on the melt polymerisation. This suggests that Ti act as a network forming element, which creates the proto-tetrahedron of garnet (Mysen, 1985). Left figure: analyses on 42 data points show a rather scattered but obvious relationship. Right figure: Mod.5.3c tested against natural and experimental data of D_{Ti} fall mostly within the +/- 50% error lines.*

3.5.3.4 Actinides

The set of models for actinides are from the work of Salters and Longhi (2002). These authors propose a predictive model for both Th and U, based on multiple regressions. However, it is possible to use the LSM with proxies to determine U from the partition coefficient of Th using the

LSM with proxy (cf.2.2.3; Blundy and Wood, 2003). Considering that Actinides enter exclusively the X site of garnet (van Westrenen et al, 2001b), it is possible to use the ionic radius model determined for tetravalent cation entering the X site, namely Mod.4.3a. HFSE4 can be assumed to have the same Young's modulus as actinides in the X site so that Mod.4.3b can be used to predict the behaviour of Act in garnet (van Westrenen et al, 2001b).

The predictive model for Th in garnet can be written in the simplified form (Salters and Longhi, 2002):

$$D_{Th} = \left(X_{(Fe+Mg)}^{melt}\right)^4 \cdot \left(X_{Si}^{melt}\right)^2 \cdot B^2 \qquad \text{Mod.5.4a} \qquad \text{Salters and Longhi, 2002}$$

with B given by:

$$B = 11.46 - \frac{24200}{T} + 8.6 \cdot \left(1 - X_{(Fe+Mg)}^{melt}\right)^2 - 2.0 \cdot (1 - X_{Gr})^2 \quad \text{Eq.5.4b}$$

The B component represent the ideal partition coefficient D_0 although additional molar composition of garnet are added in the calculus, namely $X_{(Fe+Mg)}^{melt}$ and X_{Gr}. This is due to a particular regression analysis technic based on known reaction formation and element site assignments provided in more details in Salters and Longhi (2002).

D_U can then be calculated from D_{Th} with Mod.5.4a and Mod.4.4b using the LSM with proxies (Eq.2.18).

Table 6: Literature partition coefficient data used for the regression analyses of garnet LILE1, HFSE4 and HFSE5.

References	Cs *N=3*	Rb *N=17*	K *N=25*	Na *N=41*	Nb *N=45*	Ta *N=27*	Ti *N=42*
Gaetani et al, 2003	-	-	x	x	x	-	X
Barth et al, 2002	-	x	-	x	x	-	x
Salters and Longhi.,1999	-	-	-	x	x	-	x
Hauri et al, 1994	-	-	x	-	x	-	x
Sweeney et al, 1992	-	x	x	x	x	x	-
Bennet et al,2003	-	-	-	-	x	x	-
Klemme et al,2002	x	x	x	x	x	x	x
vanWestrenen et al, 2000	-	-	x	x	x	x	-
Green et al, 2000	-	-	x	x	x	x	x
Petermann et al, 2004	-	x	x	x	x	x	x
Johnson, 1998	-	-	x	x	x	-	x
Adam and Green., 2006	x	x	-	x	x	x	x
Tuff and Gibson, 2007	-	-	x	x	x	-	x
Mibe et al, 2006	-	x	-	x	x	x	x

3.5.4   Regressions analysis

3.5.4.1 LILE1

Due to their high incompatibility of LILE1 in garnet and, therefore, the minor role of garnet in LILE1 fractionation (Adam and Green, 2006), there is a lack of experimental data for LILE1 partition coefficient in garnet in the bibliography. Hence, no previous work has studied in detail the behaviour of LILE1 in the X site of garnet and no predictive models are available. This thesis proposes a preliminary analyses of predictive models for LILE1 using a set of partition coefficient from the bibliography (Table 5). Various compositional ($X_{Gr}, X_{Py}, X_{Alm}, X_{Ca}, X_{Mg}, X_{Fe}$) and physical parameters (P, T and $\frac{Xnf}{X}$) thought to play a role in the lattice conditions of the X site (van Westrenen et al, 2000; Sun and Liang, 2013a) are tested against the set of partition coefficient for Rb, K and Na in a multiple regressions analyses study. For Cs, the set of data were not sufficient to provide an accurate fit (N=3). I will therefore use a constant for D_{Cs} in garnet. The best fits for LILE1 result in the following models (Figure 3.17).

For Cs, a constant D-value was chosen from an amphibole-bearing garnet lherzolite (Adam and Green, 2006), as follows:

$$D_{Cs} = 0.001 \quad \text{Mod.5.5a} \quad \text{This study}$$

For Rb, the fit shows dependencies on the amount of Mg only in the X site suggesting that Rb is dependent on the behaviour of Mg in the X site:

$$LnD_{Rb} = 0.4703 - 4.644 \cdot X_{Mg} + 0.656 \cdot X_{Mg}^2 \quad r^2 = 0.56 \quad \text{Mod.5.5b} \quad \text{This study}$$

For K, the analyses result in a complex dependence of K on the X_{Gr} component and the variation of P:

$$LnD_K = 4.72 - 1.4 \cdot P - 50 \cdot X_{Gr} + 8.09 \cdot X_{Gr} \cdot P \quad r^2 = 0.57 \quad \text{Mod.5.5c} \quad \text{This study}$$

For Na, Mod.5.5d can be used if Na is not considered a major component in the system. The behaviour of Na in the X site seems to be more dependent on the amount of the almandine component in the lattice:

$$LnD_{Na} = -7.64 + 27.813 \cdot X_{Alm} - 44.02 \cdot X_{Alm}^2 \quad r^2 = 0.57 \quad \text{Mod.5.5d} \quad \text{This study}$$

The models for LILE1 in garnet can be improved in the future if more data becomes available.
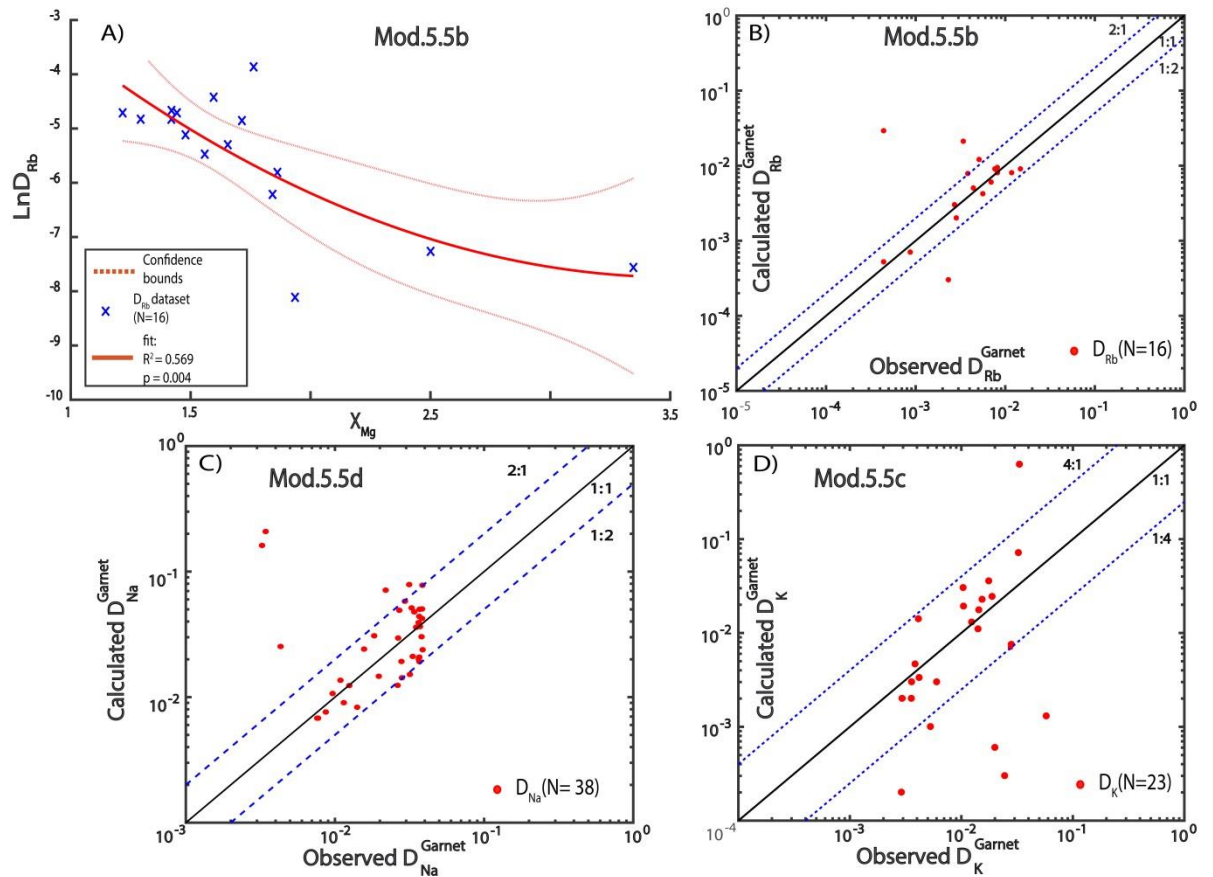
Figure 3-16: *Results of the regression analyses of D_{LILE1} in garnet from the literature data listed in Table 5. **A)** example showing the dependency of Rb for the amount of Mg in the X site of garnet. Data for D_{Rb} (N=16) show a decreasing trend with increasing X_{Mg} in the lattice site. This suggests that Rb is more compatible in Mg-poor garnet. **B)** Calculated vs observed D_{Rb} plot showing a good fit using Mod.4.5b. **C)** Calculated vs observed D_{Na} plot showing a good fit with most data falling within +/-factor 2 error lines. D) Calculated vs observed D_K show a poor fit with most data falling only in 4-fold margin of error. However, Mod.4.5c still produces the best fit and is therefore used as a predictive model in this study. Further work on the behaviour of K in garnet is needed to improve the predictive models.*

3.5.4.2 HFSE5

Like LILE1, HFSE5 are considered to be really incompatible in garnet. Therefore, no models are available in the literature. This thesis proposes a model constraining the behaviour of Nb and Ta in garnet. The role of garnet in the fractionation of Ta and Nb is minor. However, there is a good amount of data available in the literature (Table 5) and regression analyses are, therefore, achievable. The small ionic radii of HFSE5 allow these elements to enter the Y site of garnet. As stated before, the lattice conditions of the Y site are not sensitive to the compositional variation in the X site apart from X_{Gr} (cf., Chapter 3.5.3.3). Therefore the compositional parameters used in the previous fit for LILE1 (e.g., X_{Py}, X_{Alm}, X_{Ca}, X_{Mg}, X_{Fe}) are excluded from the fitting procedure. Only the X_{Gr} compositional parameter was tested against the behaviour of HFSE5 in the regression analyses, since this component affects the behaviour of the Y-site (cf., HFSE4 in gt,

Chapter 3.5.3.3). Also, physical parameters are taken into account in the regression analyses (P, T and $\frac{Xnf}{X}$). -Unfortunately, no relationships are found using the dataset provided in Table 5 and the variables previously listed. Therefore, weighted averages made on the set of partition coefficient are provided in order to use a representative constant. This gives the following results:

$$D_{Ta} = 0.0290(\pm 9.14e - 4) \quad \text{Mod.5.6a} \quad \text{This study}$$

and

$$D_{Nb} = 0.0146(\pm 2.28e - 4) \quad \text{Mod.5.6b} \quad \text{This study}$$

Further research on the behaviour of HFSE5 is required to propose a more accurate set of predictive models.

3.6 Case 6: olivine (ol)

Olivine is the most common mineral in the upper mantle and a major constituent of ultrabasic rocks such as lherzolite, dunite, hazburgite or wherlite. Like opx, olivine has a really small effect on trace element partitioning due to low partition coefficient values (Figure 3.1). Two exceptions are the transition metals Ni and Li, not explored in this study, which are both compatible in olivine, with reported values of partition coefficient up to 34 for Ni in alkali basalt (Villemant et al, 1981) and 1.3 for Li in a basalt andesite (Dunn and Senn, 1994). Also, it is thought that olivine plays a role in the fractionation of Nb from Ta in the upper mantle due to a higher compatibility of Nb in olivine, although this observation is still a matter of debate (Kelemen et al, 1993; Zanetti et al, 2004) Therefore, as for opx, the importance of olivine for the trace elements behaviour lies in the fact that the upper mantle is mainly composed of this mineral (Rudnick and Gao, 2005). Indeed, partial melting of ultrabasic rocks bearing olivine and primitive cumulates affect the evolution of trace elements concentration and is therefore of interest for modelling studies.

3.6.1   Structure of ol

Like other silicate minerals, olivine is a generic name describing a solid solution between end members. For olivine, there are two major end members, which are magnesian olivine called forsterite (Fo) and ferrous olivine called fayalite (Fa), although Mn and Ca are known to be incorporated in olivine. As displayed in Figure 3.18, olivine is an orthosilicate composed of isolated tetrahedrons sharing edges with two octahedral sites M1 and M2. Note that the lattices are 6-fold coordinated (Lumpkin et al, 1983; Zanetti et al, 2004; Beattie, 1994). The size and distribution of the sites in the structure develops according to an orthorhombic network and a space group called Pbcm (Figure 3.18). This tight arrangement of polyhedrons forms small lattices, pairing Mg and Fe in the M2 and M1 sites, so that the structure of olivine is:

$$M2_{(Mg,Fe,Ca)}M1_{(Mg,Fe)}T_{(Si,Al)_2} - O_4 \qquad \text{Str.6a}$$
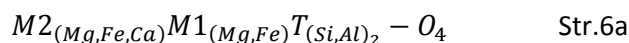
Due to the relatively similar size and the same coordination of the two lattices as well as the difficulty to measure trace element behaviour in olivine, the ordering of trace elements in olivine is unclear (Beattie, 1994; Zanetti et al, 2004; Blundy and Wood, 2003a; Wood and Blundy, 2013). Thermochemical analyses by Beattie (1994), however, led to conclude that LILE1 and LILE2 must enter the slightly larger M2 site with the energy defect of LILE1 being accommodated by 3+ transition metals such as Sc or Al in the M1 site. The fate of REE and HFSE are still unclear. However, Wood an Blundy (2014) propose a single site substitution mechanism for REE considering that (i) REE enter only one site in olivine and (ii) both sites are similar in size and stiffness. However, this does not correlate with the observation of Bédard (2005) that observed that the values of LREE partition coefficients are equivalent to MREE partition coefficients. This is typical of a double site substitution (van Westrenen et al, 2001b). Also, tetravalent and pentavalent cations (HFSE) in olivine may enter the tetrahedral site (Beattie, 1994).
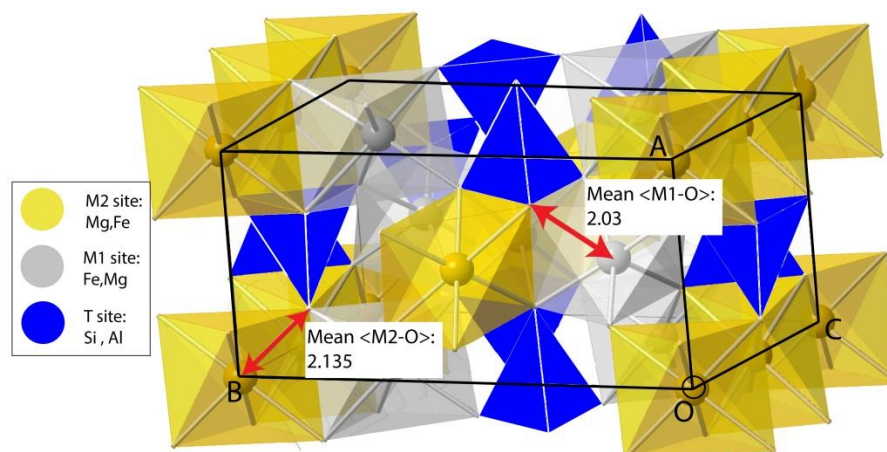
Figure 3-17: Pure forsterite olivine structure crystallised in the orthorhombic network and space group Pbnm from Smyth and Hazen (1973). <M-O> mean bond lengths are from Brown (1980). Figure shows the tight crystallographic arrangement of olivine forming tetrahedral sites (blue) sharing edges with octahedral M1 sites (grey) and octahedral M2 sites (yellow).This limits the variation in size of the lattices and affects trace element substitution.

3.6.2   Trace element controlling parameters in olivine

Like other ferro-magnesian minerals (i.e., opx, cpx), Mg and Fe is submitted to order-disorder in the M1 and M2 lattices (Lumpkin et al, 1983; Birle et al, 1968). However, the experimental and regression analyses to constrain lattice strain parameters return negative correlations with the compositions of the M1 and M2 lattices X_{Mg} and X_{Fe} (Sun and Liang, 2013a). Instead, the heterovalent substitutions are dependent on the value of X_{Fo} and the amount of tetrahedral Al.

$$X_{Fo} = \frac{X_{Mg}^{ol}}{(X_{Mg}^{ol} + X_{Fe}^{ol})} \qquad \text{Eq.3.13}$$

Melt composition is also thought to play a role in the partitioning of HFSE and actinides (Bédard, 2005).

3.6.3   LSM

3.6.3.1 REE + TM (Sc + Y)

The models for REE and Sc in olivine are from Sun and Liang (2013a). Although the behaviour of Sc in olivine is still a matter of debate, this study successfully fitted the LSM on the partition coefficients of Sc and REE suggesting that Sc enters the same lattice site as REE.

The ideal ionic radius is written as follows:

$$r_0^{3+} = 0.725 \quad \text{Mod.6.1a} \quad \text{Sun and Liang (2013a)}$$

Young's modulus is thought to be constant in the really tight crystallographic organisation of olivine, such that:

$$E^{3+} = 442 \quad \text{Mod.6.1b} \quad \text{Sun and Liang (2013a)}$$

Finally, pressure, tetrahedral Al and the Fo content in olivine seems to play a major role in the partitioning of REE in olivine by affection the strain free partition coefficient:

$$LnD_0^{3+} = -0.67 - 0.17\,P + 117.30\,X_{Al}^T \\ - 0.0147\,X_{Fo} \qquad \text{Mod.6.1c} \qquad \text{Sun and Liang (2013a)}$$

For the partition coefficient prediction of REE, the models Mod.6.1a, Mod.6.1b and Mod.6.1c must be integrated in the LSM equation (Eq.2.11).

3.6.3.2 LILE2

The used models for LILE2 in olivine are from Wood and Blundy (2013).

The ideal ionic radius is written as:

$$r_0^{2+} = 0.79 \quad \text{Mod.6.2a} \quad \text{Wood and Blundy (2013)}$$

Young's modulus follows the Hazen and Finger relationship (Figure 2.3):

$$E^{2+} = \frac{2}{3} \cdot E^{3+.} \quad \text{Mod.6.2b} \qquad \text{Wood and Blundy (2013)}$$

Finally, the most ideal behaviour for 2+ cations must be dependent on the composition of the solid solution that is either Mg-rich or Fe-rich. In the modelling part, we will consider olivine as being mainly Mg-rich, since Forsterite-rich Olivine is the common composition of upper mantle olivine. Then, Mg has the most ideal behaviour and its partition coefficient can be found via the Nernst partition coefficient as follows:

$$D_{Mg} = \frac{X_{Mg}^{mineral}}{X_{Mg}^{melt}} \quad \text{Mod.6.2c} \qquad \text{Wood and Blundy (2013)}$$

For the partition coefficient prediction of REE, the models Mod.6.2a, Mod.6.2b and Mod.6.2c must be integrated in the LSM with the proxy equation (Eq.2.18).

3.6.3.3 LILE1

The used models for LILE1 in olivine are from Wood and Blundy (2013).

The ideal ionic radius is written as:

$$r_0^{1+} = 0.79 \quad \text{Mod.6.3a} \quad \text{Wood and Blundy (2013)}$$

Young's modulus follows the Hazen and Finger relationship (Figure 2.3):

$$E^{1+} = \frac{1}{3} \cdot E^{3+.} \quad \text{Mod.6.3b} \quad \text{Wood and Blundy (2013)}$$

Finally, it is thought that LILE1 follow the behaviour of the transition metal Li^{1+} in olivine. This element is of interest for petrological studies as it can be compatible in olivine. Therefore, it can be used as the most ideal behaviour of 1+ cation in olivine. There is no predictive model to constrain the evolution of D_{Li} between olivine and melt in the literature. Therefore, a constant value will be used that represents the partitioning of Li between Olivine and melt (Sample 34Ol, Dunn and Senn, 1994):

$$D_{Li} = 0.86 \qquad \text{Mod.6.3c} \qquad \text{Sample 34Ol, Dunn and Senn (1994)}$$

However, one would argue that a constant partition coefficient as ideal behaviour of 1+ cations in Olivine is overly simplistic. Further studies are needed to constrain the systematics of partitioning of Li in Olivine to comply with this missing parameter. For the partition coefficient prediction of LILE1, the models Mod.6.3a, Mod.6.3b and Mod.6.3c must be integrated in the LSM with the proxy equation (Eq.2.18).

3.6.4   Regressions analysis

Predictive models for HFSE4, HFSE5 and Actinides are from Bédard (2005). This study tested the trace element behaviour for these elements versus C_{MgO}^{melt}. However, it infers that the models do not fit the data beyond a threshold of C_{MgO}^{melt}. Hence, the model can be written under the generic shape noted as in Mod.6.3, but is better described using a constant. So the generic model for HFSE and Act can be written as:

If C_{MgO}^{melt} lower than values specified in Table 7, then:

$$LnD_{TE} = a_{TE} - b_{TE} . ln(C_{MgO}^{melt}) \quad \text{Mod.6.3} \quad \text{Bédard (2005)}$$

and otherwise:

$$D_{TE} = c_{TE}$$

In Mod.6.3, the a_{TE} and b_{TE} are fitting coefficients listed in Table 7, and c_{TE} a constant proposed by Bédard (2005) when the C_{MgO}^{melt} threshold is reached.

Table 7: Coefficients for LILE1, HFSE4, HFSE5 and Act used in Mod.6.3 for olivine-melt partitioning. Coefficient data are from Bédard (2005).

Trace element	a_{TE}	b_{TE}	Conditions if	c_{TE}
Hf	-2.98	-0.76	$MgO < 1.38$	0.04
Zr	-0.25	-1.88	$MgO < 5.2$	0.036
Th	3.8	-4.22	$MgO < 4.9$	0.0542
U	7.08	-5.67	$MgO < 5.91$	0.0479
Nb	0.28	-3.29	$MgO < 4.4$	0.01
Ta	0	-1.5	$MgO < 3.79$	0.126
Ti^*	0.29	-0.52	$MgO < 0.493$	0.0302
* $D_{Ti} = \exp(-9.72 + 0.11\ SiO_2^{Melt})$			if $SiO_2^{Melt} > 57$	
$D_{Ti} = 0.32 - 0.034\ Mg_{\#}^{Melt}$			if $Mg_{\#}^{Melt} < 8.35$	

As shown in Table 7, smaller cations with higher valence tend to depend more on melt composition. This suggests that HFSE and Act must enter the tetrahedral site. This is in agreement with the observation of Beattie (1994).

4. Applications

The previous chapter presents a bibliographic review of trace element partitioning for 6 major minerals and for basaltic to felsic melts, and proposes preliminary models if not available in the literature. In this chapter, I will present a tool, referred to as the Trace Element Predictive Models tool (TEPM), which is built for this study, and gathers all the predictive models presented in Chapter 3. This will be followed by an investigation of trace element behaviour in real geological systems that involve the complex paragenesis of the 6 parameterised minerals. To do so, two applications will be presented to test TEPM. Firstly, this tool is applied to the reproduction of partial melting experiments from the literature. The benchmarking of partial melting experiments offers a simple mean to test the accuracy of the models for further, more complex, modelling studies of magmatic processes. Secondly, TEPM is coupled to the software tool Perple_X (Conolly, 2005), which uses Gibbs free energy minimization and a wide range of thermodynamic data to calculate stable mineral assemblages in geological systems. This code has proven to be efficient in numerical modelling studies (e.g. Hacker, 2008; van Keken et al, 2011; Siret et al, 2008; Bouilhol et al, 2015; Magni et al, 2014; Riel et al, in prep), and offers a suitable basis for the prediction of major element distributions in geodynamic systems. The coupling between Perple-X and TEPM allows forward modelling of trace element of magmatic systems in various geodynamic environments, and, in Chapter 4.5, I will present a potential application on lower arc crust processes.

4.1 Building of TEPM: A technical approach

TEPM is a numerical tool, developed to predict the partition coefficients between melt and solid during magmatic processes at various pressure, temperature and compositional conditions. As such, the predictive models for trace elements partition coefficients between the 6 minerals and their ambient melt, as presented in Chapter 3, are compiled into this tool, with the aim to be used in the forward modelling of trace element geochemistry.

In order to predict the trace element concentration in the solid and liquid phases, the implementation of mass balance equations for trace element modelling is required. In this study, only the modal batch melting equations are parameterised (Shaw, 1970; Hertogen and Gijbels, 1976; Zou and Reid, 2001), since it is particularly adapted for the application presented thereafter, although it is possible to modify the code for more complex trace element modelling studies. Modal batch melting equations are noted as follows:

$$C_i^{melt} = \frac{C_i^0}{F + D_i^{wr}(1-F)} \qquad \text{Eq.4.1}$$

$$C_i^{solid} = C_i^{melt} D_i^{wr}$$

in which C_i^{melt} and C_i^{solid} are the concentration of a trace element i in the melt and solid, respectively. C_i^0 is the initial trace element concentration, F the melt fraction, and D_i^{wr} the whole rock partition coefficient:

$$D_i^{wr} = \sum_n F^{min} D_i^{min} \qquad \text{Eq.4.2}$$

with F^{min} the fraction of mineral and D_i^{min} the partition coefficient of element i of the mineral given by the predictive models of Chapter 3.

In a first attempt to reproduce experimental data (cf., following section Chapter 4.2; 4.3), a stand-alone version of the code has been built that follows the flow diagram of Figure 4.1. For this version the reader is referred to appendix B for an example of an input spreadsheet.

Furthermore, in the interest of presenting forward modelling results, a coupling with Perple_X has been done. This code is able to give modal composition, chemical compositions and site occupancy needed by TEPM in an entire P-T-X space defined by the user.

Perple-X requires two pieces of input: the starting bulk composition X and a set of chosen solid solutions as the phases that are potentially present in the system (e.g., px, gt, pl, amph, ol and melt in this study). The accuracy of the different solid solution models relies on extensive studies made on the thermodynamic parameters of phases within different chemical systems, and recent advances allow exploring mafic and ultramafic systems (Bouilhol et al, 2015a;

Figure 4-1: Flow diagram of TEPM displaying the computational development of the code.

Jennings and Holland, 2015; Holland and Powell, 2011; Green et al, 2016). More information can be found on the Perple_X website documentation and tutorials: http://www.perplex.ethz.ch/perplex_documentation.html). Perple-X has been implemented in complex numerical models to better constrain petrological processes in various geodynamical settings. The implementation of TEPM can therefore bring further constraints on these processes as trace elements are key observations for petrogenetic models.

Further coupling with numerical code are possible, yet not attempted by this study. Examples of coupling are TEPM with dynamic models of melt genesis, transfer and emplacement via porous media flow (Tirone et al, 2012; Bouilhol et al. 2011; Riel et al, in review) or with thermo-chemical codes for large scale tectonic processes (e.g. van Hunen and Allen, 2011, Magni et al, 2013; Bouilhol et al, 2014; Gerya and Burg, 2007; Karakas et al, 2017).

Note that the use of TEPM is constrained to the limitations described above in this thesis, and that future work for trace element partitioning is needed to strengthen the predictions and to expand the domain of applicability of this tool. Also, this thesis does not explore trace element partitioning between minerals and aqueous fluids, which has been covered in a recent MSc project (Grigorova, 2017).

Foremost, this thesis proposes to investigate the systematic of trace element exchange between melt and solid via the reproduction of two melting experiments: one on an amphibolite presented in the next section and another one on a dry-MORB like eclogite presented in the next section (Chapter 4.3). Reproduction of experimental data offers a solid basis on which future numerical modelling studies can rely on.

4.2 Benchmarking 1: Partial melting of an amphibolite

4.2.1   Experimental conditions and products

Benchmark 1 was done against the partial melting experiments of Qian and Hermann (2013). This study has been chosen because it provides all the data needed for the TEPM inputs, and also an extensive set of trace-element analyses of the different experimental products. The starting material is thought to be similar to a lower crust composition (Condie and Selverstone, 1999, sample CS1999). Experiments were done between 1-1.5 GPa and 1000-1323K using a piston cylinder apparatus that reproduce favourable supra-solidus conditions of partial melting in an amphibolitic lower crust. Trace elements studied are LILE1, LILE2, REE+Y (without Tb, Ho, Tm), Sc, HFSE4, HFSE5 and actinides that were measured in the quenched melt and minerals by means of laser ablation inductively coupled plasma mass spectrometry (LA-ICP-MS). The obtained residual assemblages are composed of the minerals discussed in this study (e.g., cpx, opx, pl, amph, gt) forming amphibolites and pyroxenites/gabbros (Table 8). The melt composition ranges from tonalite to granodiorite depending on the major element composition.

Table 8: Experimental conditions and products of the partial melting experiments of Qian and Hermann (2013) (from C3081 to C3123) and Petermann et al (2004) for A343 and MP240

Experiments	T (K)	P (GPa)	$C_{H_2O}^{melt}$ (wt%)	Mode (wt%)						AP*	A/CNK**
				cpx	opx	amph	pl	gt	melt		
C3081	1273	1	13.8	22	17	-	48	-	13	Yes	1.0138
C3124	1173	1.25	9.2	18	2	20	10	11	39	Yes	1.0738
C3171	1073	1.5	10.2	-	-	62	9	2	27	Yes	1.1662
C3179	1173	1	13	12	10	24	27	-	27	Yes	1.1229
C3161	1073	1	20.8	-	-	61	16	-	23	Yes	1.0275
C3180	1073	1.25	19.4	-	-	64	22	-	14	no	1.2502
C3136	1273	1.25	6.1	20	17	-	30	-	33	Yes	0.9903
C3221	1173	1.35	8.3	13	-	18	-	25	44	No	1.077
C3162	1173	1.5	14.5	20	-	10	-	30	40	Yes	1.076
C3052	1273	1.5	3.4	26	-	-	-	30	44	yes	0.9968
C3217	1273	1.5	3.4	20	-	-	-	21	59	no	0.9892
C3123	1323	1.5	2.9	24	7	-	-	-	69	no	0.9850
A343	1700	2.9	0	8	-	-	-	1	91	no	3.542
MP240	1673	3	0	10	-	-	-	4	86	no	2.572

* Accessory phases: Titanium oxides (rutile, ilmenite, titanite), Apatite. See Qian and Hermann (2013)

** aluminousity of the melt: A/CNK>1 = peraluminous. A/CNK = Al/ (Ca+Na+K) [1]

The experiments provide a large range of pressure and temperature conditions as well as a large variety of modal compositions that, if correctly predicted, will confirm the validity of TEPM for a wide P-T-X space. Compositions of plagioclase, garnet and pyroxene fall into the range of composition that can be predicted by the tool (see appendix C). Amphibole is Mg-hornblende at low temperature and pressure (1073K and 1GPa) and tchermakite (Ca-rich hornblende) in other conditions. Moreover, the experiments lasted 1 week to ensure proper thermodynamic

---

[1] considering Al as being a network forming cation (Nielsen and Dungan, 1983), the measure of the aluminousity of the melt is a simple mean to evaluate the degree of polymerisation of the melt and is given by:

$$A/CNK = \frac{X_{Al}^{melt}}{X_{Ca+Na+K}^{melt}}$$

with X_{Al}^{melt} being the molar concentration of Al in the melt and $X_{Ca+Na+K}^{melt}$ the amount of Ca, K and Na in the melt. An A/CNK > 1 implies that the melt is peraluminous, which means more suitable for the formation of quasi-lattices (Mysen and Toplis, 2007).

equilibrium between crystals and melt (Patiño-Douce and Johnston, 1991). As such, the present phases are homogeneous in composition showing that equilibrium between melt and phases was achieved in the experimental runs. Some minor zoning occurs in pyroxene but their Fe-Mg partition coefficients indicate values close to equilibrium. Hence, a batch melting equation (Eq.4.1) for melt and cumulates is used to model the trace element partitioning with TEPM.

4.2.2   Benchmark results

An example of predicted partition coefficients is displayed Figure 4.2 for the experiments C3124 that has the most complex paragenesis. This figure shows that (i) the predictive models implemented in the tool are able to provide coherent partition coefficients for each minerals and (ii) the tool is able to capture the trace element behaviour in the different phases. The reader is also referred to appendix C for the variation of the trace element behaviour from a change in P-T-X conditions.

The results of benchmark 1 are shown in Figure 4.3 and Figure 4.4, which present the 288 predicted versus observed (LA-ICP-MS) concentration data points. A Logarithmic Pearson Chi-squared test was run on the dataset of Qian and Hermann (2013) and the predicted values by TEPM to test the goodness of fit of the program. This test is often used to compare predicted vs observed data. It is also used instead of the Normal Pearson Chi-squared to counteract the amplitude effect of dataset with values differing over several orders of magnitude such as the Qian dataset explored in this study. The test is noted as follows (Yao et al., 2012; Sun and Liang, 2012, 2013):

$$\chi_P^2 = \sum_{j=1}^{N} (\log C_j - \log C_j^o) \qquad \text{Eq.4.3}$$

With C_j the predicted concentration and C_j^o the observed concentration for a specific element j. N is the total number of experimental data (N=288). The Chi-squared critical value (χ_C^2) is calculated assuming the data have a normal distribution. A greater value of χ_P^2 than χ_C^2 means that the results are not statistically robust. For this test, I consider that an individual set of trace element data (e.g., calculated and observed) is independent to another set. Then, the dataset is not categorical and the degree of freedom is equal to N-1. The p-value used for the derivation of the critical value is p-value<0.001 and gives $\chi_C^2(Ti\ in) = 366.76$ and $\chi_C^2(Ti\ out) = 353.2$. The Pearson chi-squared test gives a $\chi_P^2 < \chi_C^2$ for the whole dataset ($\chi_P^2(Ti\ in) = 99.84$) but is significantly improved by the removal of Ti from the calculation ($\chi_P^2(Ti\ out) = 66.34$) (Figure 4.3).

Moreover, it is possible to observe in Figure 4.3 that 87% (250 points out of these 288 points) fall within +/- 50% error lines. The outliers are mainly HFSE and Act (n=25) and Sc (n=4) with some

REE (n=8) and only one LILE2 (i.e., Ba) (Figure 4.3, 4.4). Most of the outliers are contained in only three experiments, namely C3081, C3180 and C3161, which have different particularities. The experiment C3081 is dominated by pl and cpx with accessory titanium oxide (rutile and ilmenite). These accessory phases have a really strong impact on the partitioning of HFSE between melt and solid (Foley et al, 2000; Klemme et al, 2005) and can also incorporate actinides in silica-rich melt with D-values up to 7.5 (Nash and Crecraft, 1985). The overestimated concentration of HFSE and actinides in the melt for this experiment is, therefore, attributed to the presence of these oxides. The Qian and Hermann (2013) study does not provide the proportions of these oxides, which prevent more detailed modelling. For the REE in experiment C3081, La, Ce and Pr fall outside of the +-50% lines. Also in experiment C3081, Ba is overestimated in the melt by TEPM. These elements are controlled by plagioclase, being the most abundant phase in C3081 (Table 8; Figure 4.2, c.f., Chapter 3.1). As Qian and Hermann (2013) used a doped silica gel for the experiments, which has been demonstrated to change the partitioning behaviour between plagioclase and melt (Bindeman and Davies, 2000), the discrepancy between the calculated values and the measured values are interpreted to results from the "doping". This could also affect the partitioning of HFSE and Act contributing to the effect of titanium oxides. Hence, REE and Ba misbehaviour but also HFSE and Act are attributed to the doping materials used in the experiments.

Experiments C3180 and C3161 are mainly composed of low-temperature amphibole (e.g., 64wt% and 61wt% respectively, see Table 8) without any accessory phases. This suggests that amphibole controls the trace elements budget of these experiments. Qian and Hermann (2013) stated that the Mg# of amphibole products in these experiments range between 0.57-0.60. Henceforth, as the Mg# in amphibole is thought to be a main proxy for the derivation of the ratio Nb/Ta (Foley et al, 2002) with low Mg# amphibole having a higher Nb/Ta ratio, it can be inferred that Nb is more compatible than Ta in the amphibole of experiments C3180 and C3161. Moreover, HFSE4 is thought to follow the behaviour of Nb in low Mg# amphibole (Tiepolo et al, 2000; Tiepolo et al, 1999). This implies that HFSE4 are also abnormally compatible in the same amphibole. Therefore, the outliers of C3161 and C3180 may be due to the models not taking into account the HFSE behaviour in the low Mg# amphibole.

The mismatch between experiments and models for other elements (e.g., Lu, Yb and Sc) might also be caused by the use of dopant in the experiments. However, with the minor role of plagioclase in the concerned experiments (e.g., C3161, C3221), this can also be attributed to the predictive models calculating too high or too low partition coefficients. In these cases, improvements of the models are needed. One way to improve the models is to consider that, for Lu and Yb being the smallest of the lanthanide series as well as Sc a small transition metal, these elements might have a double site substitution mechanism in some minerals (van Westrenen, 2001a, Olin and Wolff, 2012). Therefore, the model considering only one site substitution

mechanism might underestimate the partition coefficient, which would result in an overestimation in the melt.
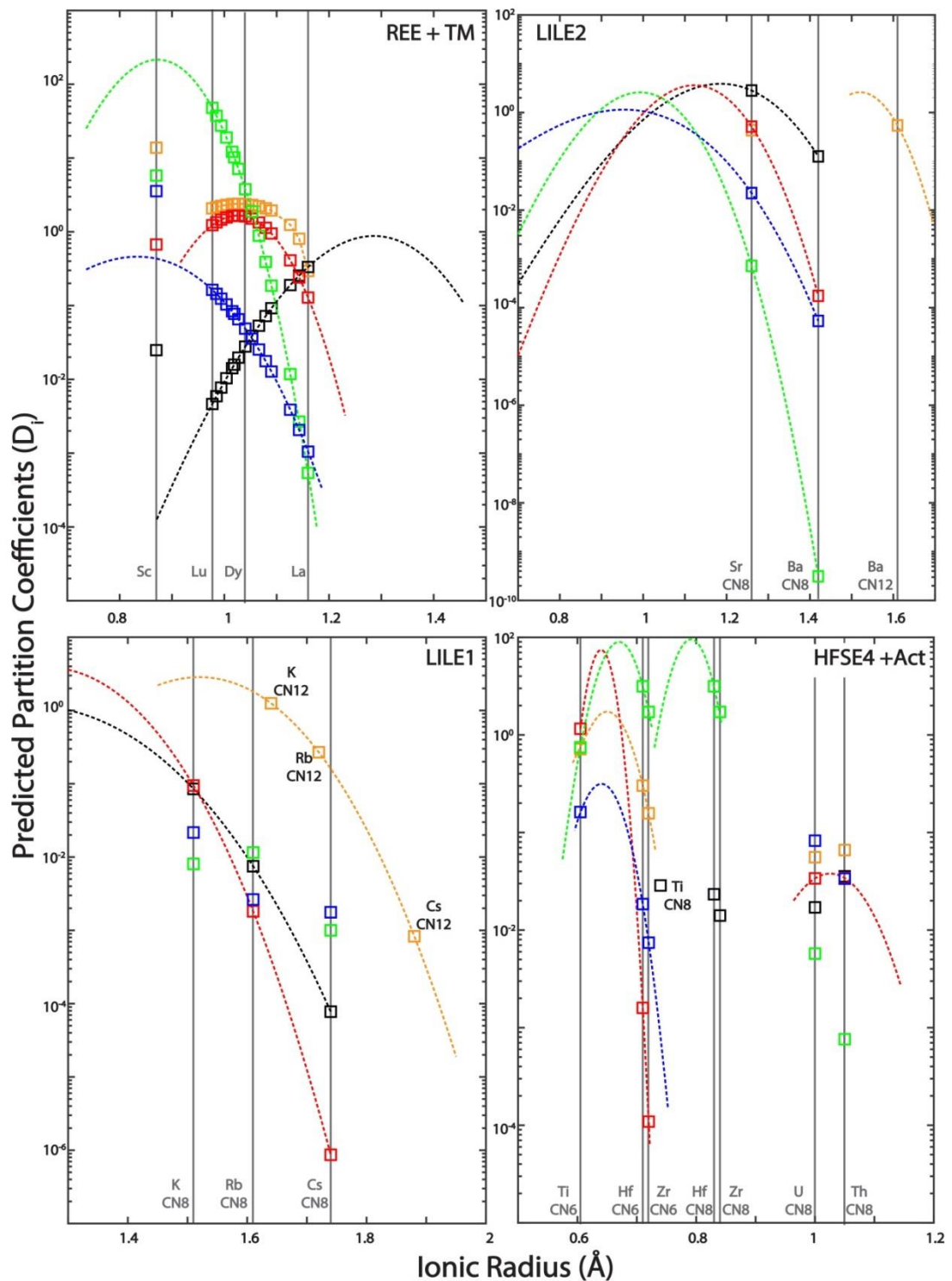
Figure 4-2: *Onuma plots showing the predicted partition coefficients of the explored trace elements for the 5 minerals present in experiment C3124 of Qian and Hermann (2013) (see Table 8). Green is garnet, red is clinopyroxene, black is plagioclase, orange is amphibole and blue is orthopyroxene. Dotted line intersecting squares are the models parametrised with the LSM and squares alone are data parametrised from regression analyses.*
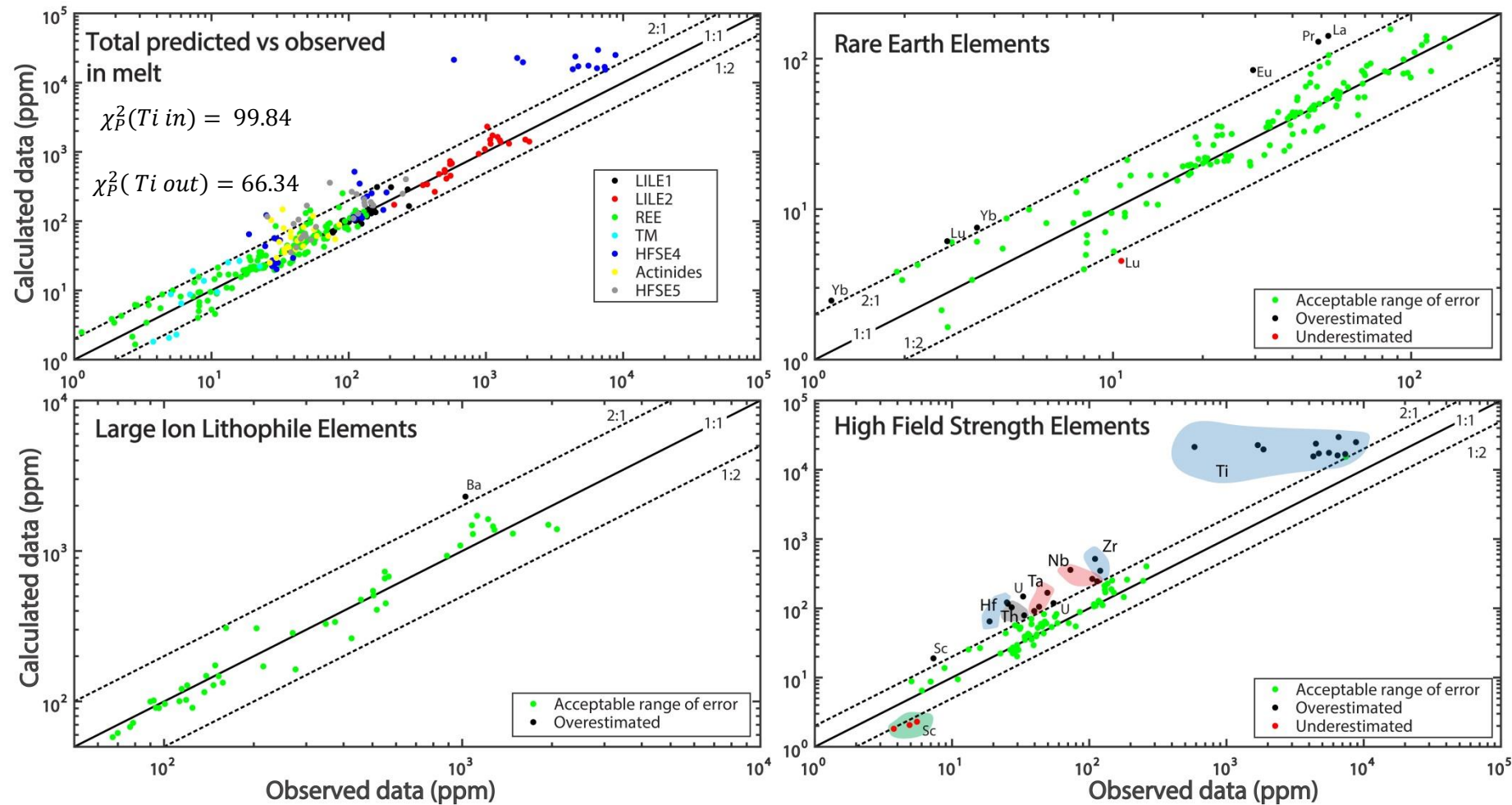
Figure 4-3: *Calculated vs observed trace element concentrations in the melt grouped according to trace element type. 250 out of 288 data points fall within the +-50% mismatch range. The Pearson Chi-squared analysis calculated from Eq.4.3 is shown on the top left figure. The results show that the predictive models fail to correctly predict the behaviour of Ti for these experiments.*
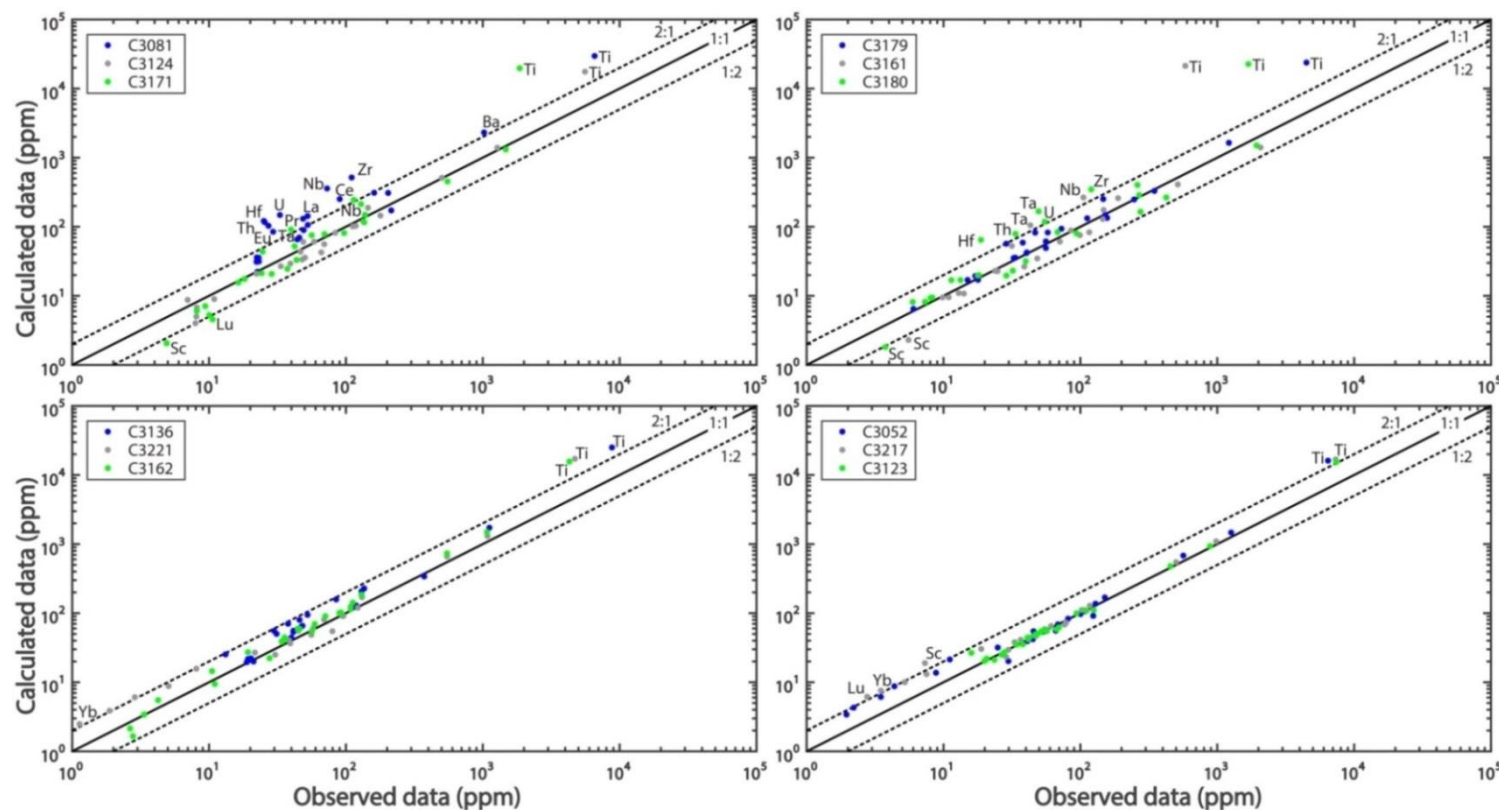
Figure 4-4: Calculated vs observed trace element concentration in the melt showing the outliers according to the experiments. Top left figure has numerous blue outliers which are from experiment C3081. This experiment is controlled by the presence of plagioclase (48wt%). This mineral is known to alter trace element behaviour in doped experiments (see text). Top right figure displays the effect of amphibole in the system. Particularly low Mg# amphibole of experiments C3180 probably controls the behaviour of HFSE4 and HFSE5. TEPM is not yet able to predict HFSE behaviour in low Mg# amphibole (see text). For all other experiment, all the data points are in really good agreement with experimental data, apart from Sc that has behaviour not yet predictable by TEPm and Ti and is controlled by the titanic oxides present in the experiments (see text, Table 8).

4.3 Benchmark 2: Partial melting of a dry-MORB eclogite

The second benchmark involved partial melting experiments done on anhydrous MORB-like eclogites in Pertermann et al (2004).

4.3.1   Experimental conditions and products

In their study, they carried out high pressure and high temperature experiments using a piston cylinder apparatus to reproduce the melting of anhydrous MORB-like eclogite with various Ti content under upper mantle conditions. The main purpose of their work was to study the effect of various amounts of garnet on the trace element composition of partial melts. As such, the studied pressure and temperature range from 2.9 to 3.1 GPa and from 1500 to 1600 K to assure garnet crystallisation. The obtained experimental products are composed of gt, cpx and melt (Table 8). Trace elements investigated are HFSE, TM, LILE2, Act, LILE1 (excluding Cs) and REE (La, Ce, Nd, Sm, Eu, Gd, Dy, Er, Yb,Lu), which were measured using LA-ICP-MS. The duration of the experiments ranged from 4 to 34 hours, which, according to the recommendation of Patiño-Douce and Johnston (1991), is not enough to reach full thermodynamic equilibrium. Nevertheless, the authors argue that trace elements spectra are very similar for each analysis, which suggests that the duration time of the experiments was enough to properly equilibrate the crystals. Hence, full equilibrium is assumed here and the batch melting equation Eq.4.1 is used for the calculation.

Benchmarking was done on samples A343 and MP240 (Table 8). Sample A343 was created at 2.9 GPa and 1670K and is composed of gt (1wt%), cpx (8wt%) and melt (91wt%). Garnet is pyrope in composition (i.e., Chapter 3.5, eclogite A) and cpx is salite-diopside reflecting the condition of UHP mantle conditions (see appendix D). Sample MP240 was created at 3 GPa and 1610 K and is composed of gt (4wt%), cpx (10wt%) and melt (85wt%) with a small fraction of kyanite (1wt%).The garnet is a Py-Gr-Alm mixture although richer in Py (e.g., cf., Chapter 3.5, eclogite B, see appendix D) and cpx is augite. The gt and cpx compositions reflect UHP crustal conditions. Both formed melts are intermediate in composition.

4.3.2   Benchmark results

Results are presented in Figure 4.5, in which the predicted versus observed concentration (LA-ICP-MS) are plotted against each other. In this benchmark 95% (42 out of 44 data points) fall within the +-50% discrepancy lines. Additionally, the Pearson Chi-squared return a low value of 2.83 (Figure 4.5)

The outliers are, in both experiments, the transition metal Sc. As stated in the previous benchmark, the models for Scandium are not totally consistent with natural processes due to a double substitution mechanism in garnet (van Westrenen et al, 2001b). The presence of the

aluminosilicate kyanite in experiment MP240 has a really small effect on the trace element partitioning and does not alter the prediction.
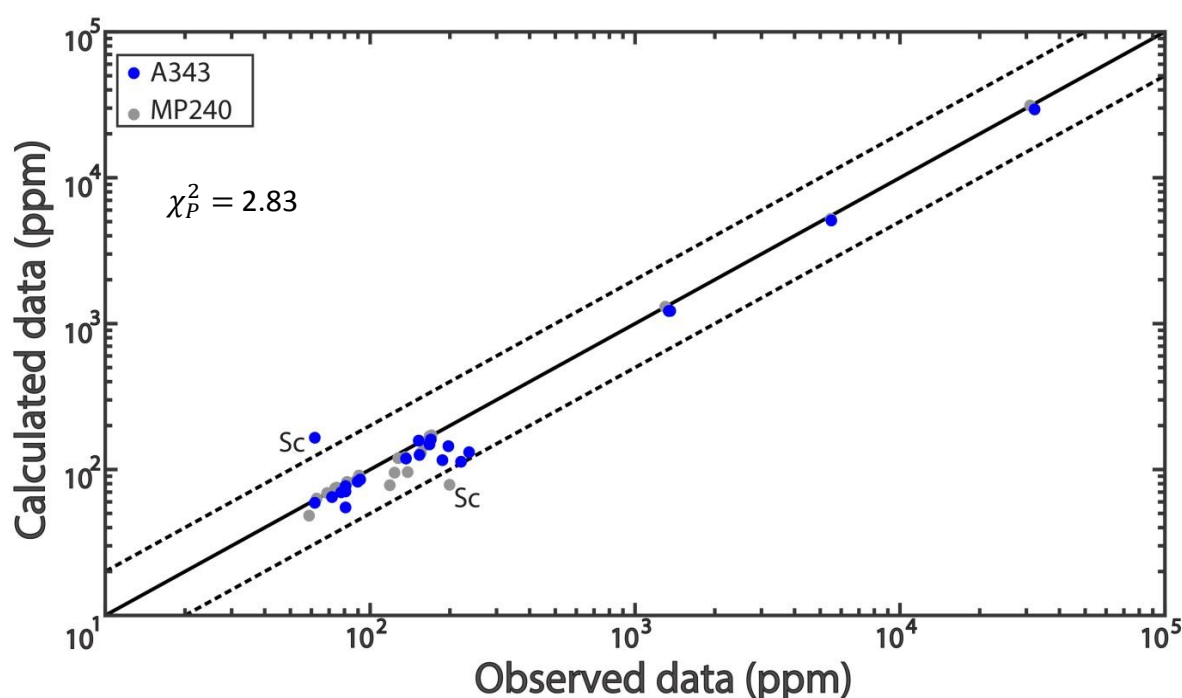
Figure 4-5: Calculated vs observed trace element concentrations in the melt in experiments A343 and MP240 of Pertermann et al (2004)

4.4 Benchmark discussion

The +/- 50% error lines (or more precisely, the +/- factor 2 error lines) are usually used by authors to compare predictive models of trace elements partition coefficients against observed natural or experimental data (Sun and Liang, 2013; Yao et al; 2013; Dohmen and Blundy, 2014). Data within the error lines is considered as being within the acceptable range of error since a maximum of 50% mismatch does not prevent good interpretation of trace element behaviour in the modelling of petrogenetic processes. In that case, it can be concluded that the 87% data points for Benchmark 1 and the 95% data points for Benchmark 2 fall within the +/- 50% lines. Additionally, a Pearson Chi-squared analysis was performed to add a statistical interpretation to the benchmarking. Following the results presented in Figure 4.3 and Figure 4.5 for the Pearson Chi-squared, it can be concluded that TEPM predict well the experimental data, with the exception of Ti, in the presented P, T and chemical conditions.

Accounting for the conditions of the experiments for Benchmark 1, namely, water-rich and peraluminous-felsic melts as well as the presence of accessory phases (Table 8), the outputs of TEPM are quite promising. The model performed well, despite the fact that the melt compositions are water rich, and range from intermediate to felsic, with several experiments reaching the peraluminous threshold (A/CNK > 1; c.f., Table 8), with both characteristics potentially affecting

the polymerisation state of the melt and hampering a proper portioning prediction (Nielsen and Dungan, 1983; Mysen et al, 1985, cf., Chapter 1.3) (Blundy and Wood, 2001; Green et al, 2000). This implies that the models that are based on the polymerisation state of the melts (e.g. amphibole) have been well calibrated. Furthermore, some minor titanium oxides occur in experiments altering the behaviour of Ti and HFSE5 in the system due to their high compatibility in oxides (Timm et al, 2011; Foley et al, 2000). Also, the oxidation state of the experiment is not taken into account in the model, (which may lead to further discrepancy for some elements like Eu that can change redox state from Eu^{3+} to Eu^{2+} affecting its compatibility in plagioclase).The trace element prediction allows to accurately determinate the misbehaviour of these elements.

Hence, the results suggest that (i) most of the trace elements behave according to their predictive models with acceptable misfit due to the other environmental parameters, and (ii) the models can be used for further numerical modelling involving amphibolite derived melt (e.g., intermediate to felsic melt) that minimise or neglect the effect of accessory phases.

The partial melting conditions for Benchmark 2 are optimal for trace element prediction (e.g., water free, intermediate composition of melt and absence of accessory phases). This allow TEPM to reproduce almost perfectly the experimental data in melt rich environment (e.g., 91wt% and 85wt%) with only two outliers, as discussed before. This suggests that (i) TEPM is able to capture trace elements signature induced by a small fraction of crystals and (ii) UHP and UHT conditions can be covered by the tool.

So despite various physical and chemical conditions explored in the benchmarking studies, TEPM reproduces their experimental data rather well. Provided that other partial melting experiments can be reproduced with the same level of accuracy, TEPM can be used in future modelling studies involving the 6 minerals described in this thesis, and provides a solid basis for forward modelling of the dynamic evolution of trace element signatures during melt genesis, differentiation and transport in a crustal or mantle environment.

4.5 Application: investigation of trace element behaviour in a P-T-X space

This section introduces a novel approach for trace element forward modelling during partial melting of an amphibolite by coupling TEPM and Perple_X. Amphibolites are of a significant scientific interest, since they are thought to be the main component of the lower continental crust (McDonough and Sun, 1995). Hence, they probably experience regular thermo-chemical anomalies from upper mantle in various potential geodynamic contexts, such as subduction zone settings or intraplate hotspots (Annen et al, 2006). For example, it is now widely accepted that the stacking of mantle wedge melts at the arc crust-mantle boundary implies two major processes. First, magma underplating generates large thermal anomalies, which destabilizes the bottom of

the crust. This induces a thickening of the crust by Melting, Assimilation, Segregation and Hybridisation mechanisms (and therefore referred to as the MASH zone, Hildreth and Morbath, 1988). Secondly, MASH processes in amphibolite are also thought to control the composition of the upper continental crust as well as the generation of long-lived plutonic bodies by differentiation of the mantle melts and the assimilation of the amphibolite crust inducing partial melting of the latter (Foley et al, 2002; Annen et al, 2006; Karakas et al, 2017). However, lower crustal magmatic processes are still a matter of significant debate (Ducea et al, 2017; Otamendi et al, 2012; Annen et al, 2006).

The following application will therefore focus on lower crustal conditions in arc systems (e.g., 0.5 to 1.5GPa and 973 to 1473°K) and explore the geochemical signatures generated by amphibolite partial melting, thereby ignoring any other MASH processes, such as the contribution of mantle derived melts.

A starting composition representing the lower crust composition (Qian and Hermann, 2013; Condie and Selverstone, 1999) is used in Perple_X and normalised to the NCFMASH system (Na, Ca,Fe, Mg, Al, Si, H), together with solution models calibrated for this P-T-X space (calibration can be found in Riel et al, in review). The starting composition can be found in Table 9. The initial concentration of trace elements C_i^0 is representative of the lower crust and is given by Rudnick and Gao (2003). The major compositions of the phases are calculated with Perple_X and are subsequently used by TEPM to predict the trace element composition via a modal batch melting equation (Eq.4.1). The results of the coupling give a full catalogue of trace element behaviour in a P-T space of lower crust partial melting. Note that, in nature, equilibrium batch melting is an unlikely process since a crystal grows or melts incrementally depending on the thermal state of the system. However, considering that Perple_X predicts the stable phase compositions on an equilibrium basis from a bulk starting composition at a given P and T, it is reasonable to assume that the use of Eq.4.1 is correct in this specific scenario.

Table 9: *Starting composition for major elements informed in Perple_X (from SiO_2 to H_2O, the units are in wt (%)) normalised from Condie and Selverstone (1999) and trace elements informed in TEPM (from Cs to Nb, the units are ppm) from Rudnick and Gao (2003):*

SiO_2(wt%)	48.55	Na_2O	2.35	Ba	259	Nd	11	Dy	3.1	Yb	1.5	Zr	68
Al_2O_3	15.22	H_2O	1	Sr	348	Sm	2.8	Y	16	Lu	0.5	U	0.2
FeO	8.15	*Cs(ppm)*	0.3	La	8	Eu	1.1	Ho	0.68	Sc	31	Th	1.2
MgO	6.77	Rb	11	Ce	20	Gd	3.1	Er	1.9	Ti	8000	Ta	0.6
CaO	8.9	K	6000	Pr	2.6	Tb	0.48	Tm	0.24	Hf	1.9	Nb	5

From the results, it is possible to make several observations such as evolution of the relative concentration of an element ($\frac{c_{calc}}{c_{ini}}$) according to the phase fractions, P-T grids of trace element

ratios in the system, P-T grids of one particular trace element behaviour in the system, P-T grids of variation of trace element behaviour in one particular phase, and so on. Here, we will focus on two types of such results.

First, the evolution of the relative concentration of two important elements in the system will be presented, namely Sr and Yb. This will be done on isothermal and isobaric sections. This allows investigating the detailed effect of dominant phases on the behaviour of the elements and will introduce the concept of dominant and controlling phases. Also, it allows constraining the effect of the modal composition.

Trace element signatures are often studied using the ratio of two elements thought to fractionate from one another in particular conditions. Therefore, a second study will explore three different important ratios for amphibolite system that are Dy/Yb, La/Yb and Sr/Y (Profeta et al, 2015; Davidson et al, 2007; Bouilhol et al, 2015; Smith, 2014; Chiaradia, 2015; Moyen and Stevens, 2006). Each of these ratios are normalised to their initial concentrations. A low value of Dy/Yb is usually interpreted to account for the presence of amphibole in the source (Davidson et al, 2007). A high value of La/Yb is interpreted to account for the presence of garnet in the source (Shen and Forsyth, 1995, van Westrenen and Draper, 2007). A low value of Sr/Y is interpreted to account for the presence of plagioclase in the source (Blundy and Wood, 1991; Chiaradia, 2015). Therefore, this study gives insight on the typical signature the melt and solid can have according to the degree of partial melting induced by the increase of temperature and the impact of major controlling phases in the system for each ratio.

4.5.1   Modal and chemical composition of computed products

First, the computed products of the Gibbs free energy minimization of Perple_X in term of major element composition are presented for the dehydration melting of a lower amphibolite crust. Figure 4.6 shows the misfit of Perple_X compare to Qian and Hermann (2013) data and add uncertainty on the accuracy of the output results. Figure 4.7 displays the modal composition of the stable phases, while Figure 4.8 displays the range of compositions for the computed phases, apart from amphibole which shows very little compositional variation and is, in its entire stable domain, Ca-hornblende.

Figure 4-6: *Left: Original grid calculated from Perple_X for the partial melting of an amphibolite in the NCFMASH system (See table 9 for starting composition). Right: Modal comparison between Qian and Hermann (2013) experiments and calibrated solid solutions used in Perple_X for different pressure and temperature (Riel et al., 2018).The circles represent the weight percent of phases at various pressure and temperature obtained in the experiments of Qian and Hermann (2013). The solid lines are the evolution of the modal composition while using the Perple_X models for the same condition of pressure, temperature and composiiton.The right hand side panels aim to show the misfit between experimental data and computed data that add uncertainty to the use of TEPM for trace element behaviour prediction. Note that more comparison between the calibrated Perple_X solid solutions and several others experimental data were performed and are shown in the supplementary materials of Riel et al (2018).*

Figure 4-7: *Results of computed modal composition in the amphibolite system by Perple_X. Top left plot: Melt fraction+ topology of the system. Other plots: indicate the amount of a specific phase, with the name of phases indicated on top of each plot. Colour bars indicate the modal fraction of stable phases in wt%.*
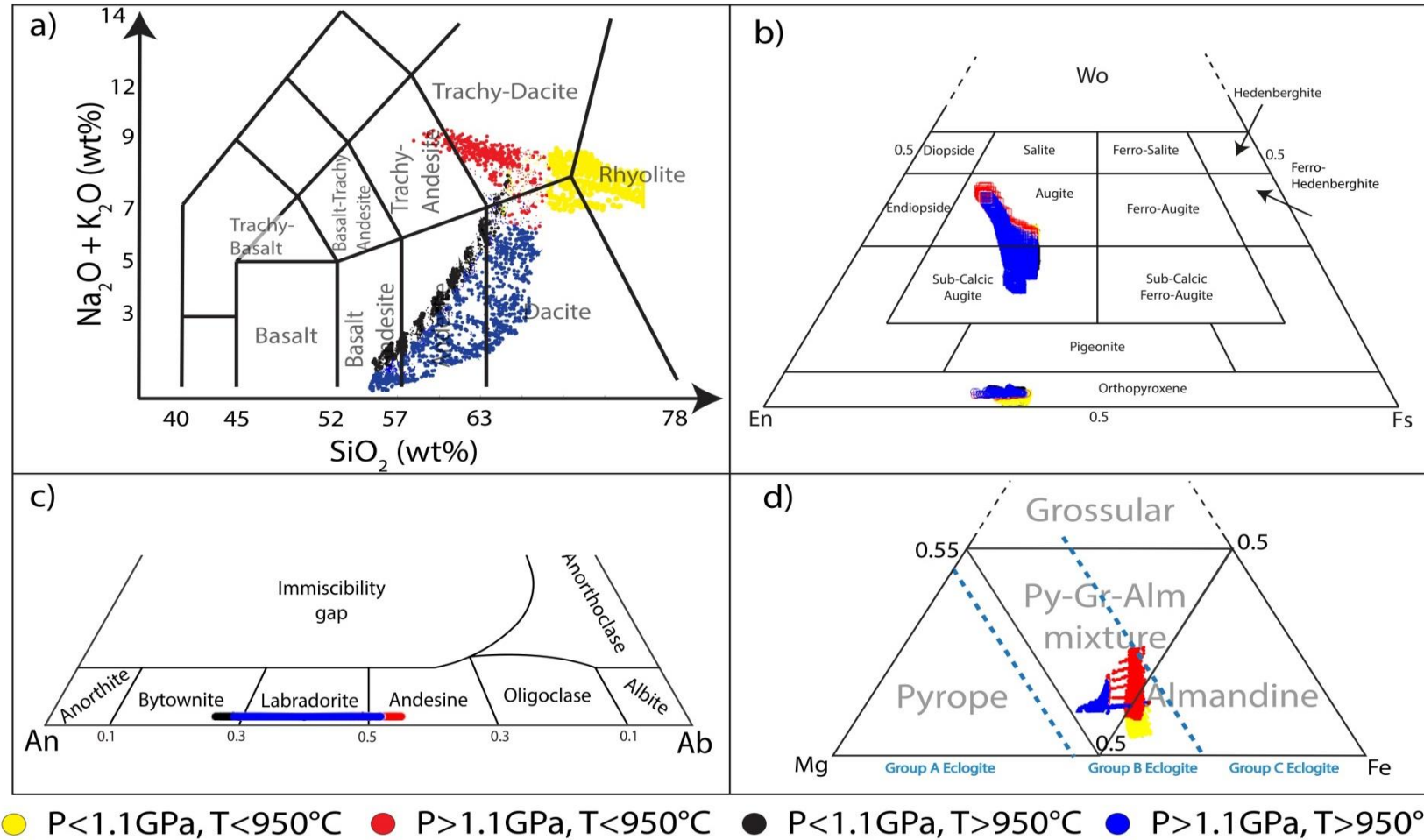
Figure 4-8: *Results for the computed compositional variation of stable phases given by Perple_X. Results are colour-coded according to the P-T condition, as indicated in the legend at the bottom.* **a)** *Melt composition ranging from rhyolitic at LT/LP to basalt andesite at HP/HT (see text).* **b)** *Range of pyroxene compositions. Cpx: Sub-calcic-augite to augite, Opx: enstatite.* **c)** *Range of plagioclase compositions. Bytownite (HP/HT) to andesine (HP/LT).* **d)** *Range of garnet composition: LT/LP almandine garnet. HT/HP and LT/HP are garnet mixtures.*

Melt fraction increases linearly with temperature until the right edge of the grid (Figure 4.7). Plagioclase is ubiquitous in the entire system but is more abundant at low pressure (LP, < 1.1GPa) forming gabbros-like products. Amphibole is stable at low temperature, forming opx-bearing amphibolite at LP and gt-bearing amphibolite at high pressure (HP, > 1.1GPa). Amphibole breaks down to give cpx + melt at ~940°C. Orthopyroxene is mainly present at LP and absent at HP and is a main component of the low-temperature gabbros (LT, < 940°C). Clinopyroxene is ubiquitous after amphibole breaks down and follows also the disappearing of orthopyroxene. Clinopyroxene forms pyroxenite-like products at high temperature (HT, > 940°C). Finally, garnet is present at HP and is concordant with the progressive decrease of plagioclase content in the system forming eclogites-like products.

Compositional variation in stable phases displayed in Figure 4.8 shows that the melt varies from basalt-andesite/dacitic at HT and evolves progressively to rhyolitic/(trachy)dacitic at LT. Pyroxene vary from sub-calcic augite to augite for clinopyroxene and remains enstatite-like for orthopyroxene. Plagioclase varies from bytownite at LP/HT to andesine at HP/LT. Finally garnet is mainly eclogite B with LP/LT garnet being almandine in composition. The almandine garnet is thought to have a special effect on trace element behaviour (van Westrenen and Draper, 2007; cf., Chapter3.5). This study will then neglect this effect and will consider the almandine garnet to behave like Py-Gr-Alm garnet mixture (cf., Figure 2.8).

4.5.2   Trace element in the melt and effect of dominant phases

Using the major element output from Perple_X, TEPM can now calculate trace element distributions. The first trace element application will display the evolution of the relative concentration of Yb and Sr according to both isothermal and isobaric sections. These two elements are thought to be controlled by the presence of gt, cpx and pl. These phases are important during amphibolite melting, and melt production in their stable domains have implications on crustal building (Profeta et al, 2015; Moyen and Stevens, 2006; Chiaradia, 2015; Davidson et al, 2007).

This application helps to understand of which stable phases apply a major control on the entire system. Also, the study of relative concentrations is useful for the investigation of the thresholds at which some controlling phases lose control in favour of others.

The isothermal sections are displayed on Figure 4.8. The conditions are P varies from 0 to 1.5 GPa and T=1000°C. In those conditions, pl is thought to control the system at low pressure (i.e., positive x-axis in Figure 4.9) and progressively disappear in favour of garnet at high pressure (negative x-axis, Figure 4.9) (cf., Figure 4.6). From these results, it is possible to observe different trends for Yb and Sr. For Yb, pl is the dominant phase at low pressure leading to an incompatible behaviour of Yb in the solid, so that Yb prefers to stay in the melt (e.g. melt Yb/Yb_N>1,Yb highly

incompatible in pl, see Chapter 3.1). If pressure rises and gt becomes stable in the system, the relative concentration of Yb drops critically until it becomes compatible in the solid (e.g., melt $Yb/Yb_N<1$, Yb highly compatible in garnet, cf., Chapter 3.5 and to some extent compatible in cpx, Chapter 3.3). It is interesting to point out that the behaviour of Yb becomes compatible in the solid while pl is still a dominant phase. It is possible to quantify the thresholds at which the effects of gt and cpx exceed the effect of plagioclase, which, in this case, is 0.04gt + 0.29cpx + 0.39pl at P=1.2GPa (Figure 4.9). For Sr, the trend is inversed from the one of Yb, and illustrates the compatible behaviour of Sr in plagioclase (cf., chapter 3.1). Here again, it is possible to quantify the threshold at which the effects of gt and cpx exceeds the effect of plagioclase. In this case, the threshold occurs at 0.27gt + 0.29cpx at 1.48GPa. It is interesting to note that, for Sr, it requires much more gt and cpx to blur the signature of pl on Sr.
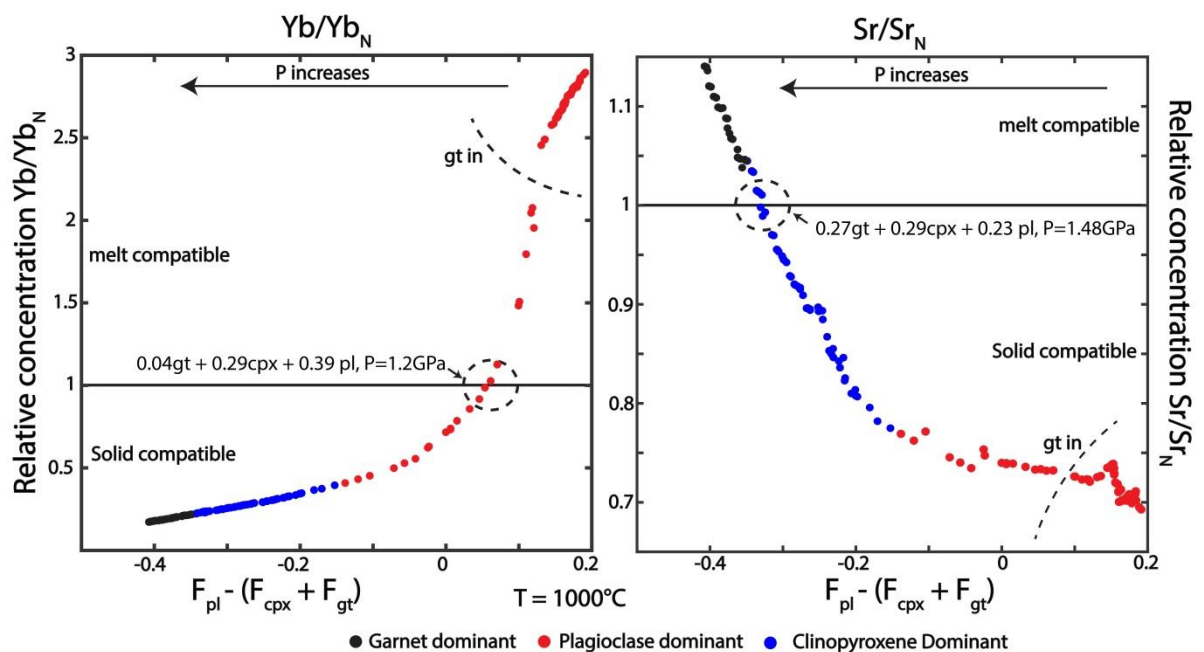
Figure 4-9: *Evolution of the relative concentration in the melt of two important elements (Yb and Sr) according to the modal variation of main controlling phases (plagioclase, clinopyroxene and garnet, see text) at T=1000C and P varies from 0 to 1.5 GPa. <u>Left:</u> This figure allows to observe the strong control of gt and cpx on the behaviour of Yb. Plagioclase effects on the signature of Yb is blurred when the modal composiiton of cpx and gt increases in the system although pl is still the main controlling phase <u>Right:</u> illustrates the strong control of pl on the behaviour of Sr. Plagioclase keeps control of the Sr behaviour at much higher pressure and modal composition than Yb.*

Figure 4.10 shows the evolution of the same elements but as a function of the amount of partial melting (e.g., melt fraction F_{melt}). Unlike Figure 4.9, the relative concentration profiles are made keeping pressure constant (at P=0.9, 1.1 and, 1.3 GPa) and varying temperature. Figure 4.10 displays the effect of amphibole out, gt out and increase/decrease of cpx and pl, respectively. For Sr, at lower temperature (T<~940°C) amphibole is an ubiquitous mineral that has a minor control on the behaviour of Sr. As such, the relative compatibility of Sr at low melt fraction ($F_{Melt}<0.05$) for

all pressures shows a melt compatible behaviour. But it is important to point out that the behaviour at low melt fraction is oversimplified by the batch melting equation (Eq.4.1) used in this study. Indeed, when F tends to 0, the relative concentration equates $C_i^N = \frac{1}{D_i^{wr}}$ (with C_i^N the relative concentration) so that the relative concentration is inversely proportional to the whole rock partition coefficient D_i^{wr}. At low melt fraction and high amphibole content $D_i^{wr} \sim D_i^{amph}$ as calculated by Eq.4.2, which explained the melt compatible behaviour of Sr at low melt fraction in Fig.4.10.
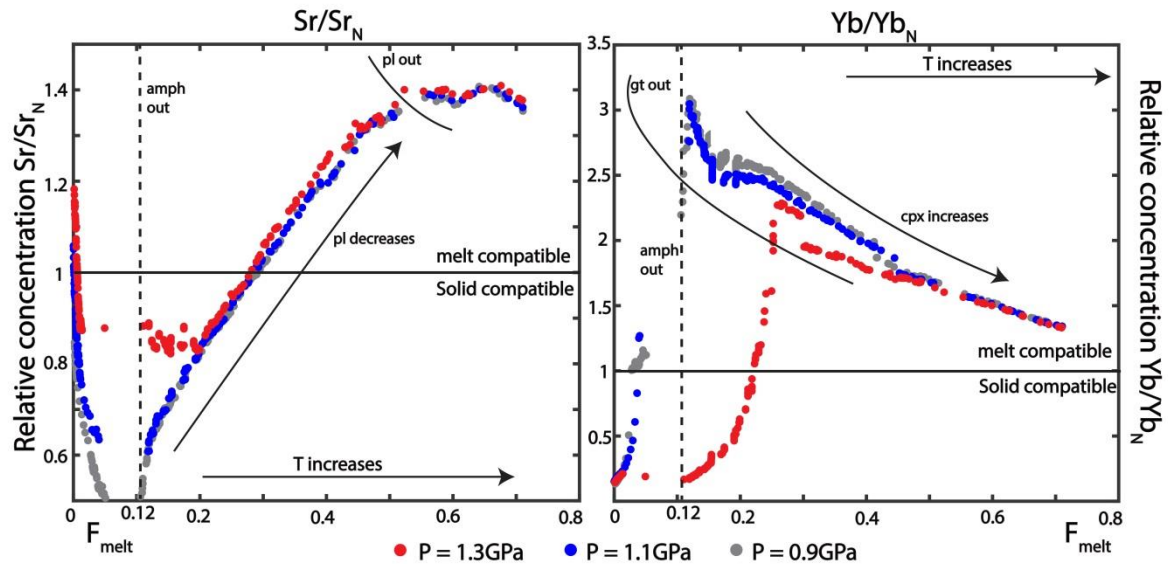
Figure 4-10: *Evolution of the relative concentration of two important elements (Yb (left) and Sr (right)) according to the variation of melt fraction when T varies and P=1.3GPa, P=1.1GPa and P=0.9GPa (see text for explanations).*

When F_{Melt}>0.05 the role of other phases is visible. Indeed, at low pressure the paragenesis is composed of plagioclase, which again leads to a relative compatibility of Sr in the solid. Note that the compatibility increases with the disappearance of amphibole and with the increase of plagioclase content. After amphibole disappears (amph out in Figure 4.10), the amount of cpx increases progressively whereas plagioclase decreases. This can be seen for Sr by a progressive decrease of compatibility until a plateau is reached meaning that pl is out of the system. At higher pressure (P=1.3GPa), the role of garnet can be seen by a relative concentration being constant, suggesting that the role of garnet compensate the one of pl until a threshold is reached (around F~0.2) to finally behave like the other profiles. For Yb, the ubiquitous amphibole at low temperature seems to retain the HREE, but the progressive amph breakdown decreases the Yb compatibility in the solid, except at higher pressure (P=1.3GPa) where garnet controls the budget of Yb. In that case, the disappearing of amph (amph out) has a "jump" effect on the behaviour of Yb whereby Yb becomes highly incompatible in the solid for lower pressure. For higher pressure, the control of garnet on the budget of Yb shows that it retains this element at much higher temperature and partial melting degree. Cpx controls the behaviour of Yb when garnet is absent.

It also shows how a higher degree of partial melting forms cpx, which is more suitable for HREE incorporation. Due to the control of cpx, Yb compatibility in the melt decreases progressively until the end of the model (T=1300°C, F_{Melt}=0.75) with values of Yb/Yb_N decreasing from 3.2 to 1.4.

The quantitative knowledge of the evolution of the relative concentration of an element is particularly useful to understand the systematic of exchange between the melt and the solid in a complex system. The results presented in this section show that, although some minerals have a strong impact on the behaviour of some trace elements, the apparent evolution of those trace elements in the melt is controlled by the modal composition of the system.

4.5.3   The ratio Dy/Yb

The normalised against initial concentration ratio $(\frac{Dy}{Yb})_N$ is thought to be controlled by amphibole that has more affinity for Dy than for Yb (Tiepolo et al, 1999; Tiepolo et al, 2000; Tiepolo et al, 2007, Dalpé and Baker, 2000) (see Annexe D for comparison between relative and absolute concentration). It is therefore used to trace the presence of amphibole in the source of amphibole derived magma. This, for example, has been successfully tested by some authors who suggested the presence of "cryptic" amphibole down in the source of arc lavas (Davidson et al, 2007; Laroque and Canil, 2010; Kratzmann et al, 2010). However, in some cases, Dy is ideally incorporated in clinopyroxene, creating similar signatures as amph, which suggests that cpx is a precursor to the creation of cryptic amphibole (Smith, 2014, Bouilhol et al, 2015b). Therefore, this study investigates the variation of $(\frac{Dy}{Yb})_N$ in the partial melting of an amphibolite in lower crustal conditions. The results are presented in Figure 4.10 in which solid and melt $(\frac{Dy}{Yb})_N$ ratio normalised to initial concentrations are shown. The reader is referred to Figure 4.6 and 4.7 to compare the modal proportion and the composition of phases with the P-T grids for Dy/Yb presented in this section.

In the melt, Figure 4.11 illustrates a number of aspects of the behaviour of $(\frac{Dy}{Yb})_N$. Firstly, at HP/LT conditions, amphibole is ubiquitous in garnet amphibolite. The melt fraction generated is rather small (e.g., <10wt%). The ratio $(\frac{Dy}{Yb})_N$ seems to be controlled by both the presence of amphibole and garnet. Indeed, Yb is more compatible in gt than Dy so that it increases the ratio greatly (e.g., more Dy in the melt). However, at these HP/LT conditions, amphibole counteracts the effect of gt since Dy is more compatible in this phase, which decreases the ratio (i.e., less Dy in the melt). This leads to a lower fractionation of these two elements with values around 2.5-3. Secondly, at HP/HT conditions, amphibole breaks down to give cpx + melt. Also garnet is a common phase. This gives an eclogitic assemblage. The melt fraction increases as temperature increases (cf., Figure 4.7). At these conditions, the effect of garnet on the ratio is clear. Indeed, the ratio is very high (e.g., >3.5), as Yb is depleted in the melt due to the high compatibility of this element in gt.

However, a progressive decrease of the ratio can be observed if temperature is increasing (e.g., from >3.5 to ~2). This can be correlated with the progressive increase of the cpx content in the assemblage, which suggests that cpx has a similar effect on the ratio as amphibole. Finally, the disappearance of garnet from the assemblages has a critical effect on the ratio. Indeed, values approximate 1-1.5 (e.g., blue areas in Figure 4.11). This illustrates, both at LT and HT in low pressure domains, that the ratio is controlled by the presence of amphibole and cpx only. In these P-T domains, Dy is almost as compatible in the melt as Yb, confirming the observation of Davidson et al (2007) and Smith (2014). Note the slight effect of pl on the Dy/Yb ratio after amph breaks down displayed by a small increase of the ratio. This effect is related to Yb being less compatible in pl than Dy due to the inverse trend of REE in this mineral (cf. Chapter 3.1; Figure 4.2). Therefore, although the melt is in equilibrium with amphibole, the role of the latter on the behaviour of $(\frac{Dy}{Yb})_N$ is often blurred by other major phases (e.g., cpx, gt, pl). This implies that not only the behaviour of trace elements in magmatic systems depends on partition coefficient but also on the fraction of minerals as argued in Chap.4.5.2 (Figure 4.7). Additionally, it can be inferred from these results that phases might play a major role in melt genesis and transfer although their trace elements signature is not recorded in upper crustal magmatic systems.

In the bulk solid part of Figure 4.11, several effects can also be shown. Firstly, while amphibole is still a main phase in the assemblage, the fraction of melt produced is rather small (<10wt%). Therefore, it is expected that the concentration in the solid of Yb and Dy is really close to the initial concentration (e.g., $(\frac{Dy}{Yb})_N \sim 1$). This can be observed in Figure 4.11 where amphibole is stable. Secondly, as the melt fraction increases, fractionation in the solid can be seen. At LP conditions, the increase in melting seems to be the main driver of fractionation between Dy and Yb. This relates to Figure 4.10 where the behaviour of Yb normalised to initial concentration is shown. Indeed, despite the fact that some phases can incorporate this element (e.g., cpx), Yb remains melt compatible until the end of the model that is T = 1300°C and P from 0 to 1.5GPa. Moreover, at HP/HT conditions, where gt is still stable and cpx+melt are the main stable phases in the system, the ratio $(\frac{Dy}{Yb})_N$ is the lowest in the solid. This also accounts for the effect of gt on Yb but the increase of melt fraction seems to amplify the effect of gt.
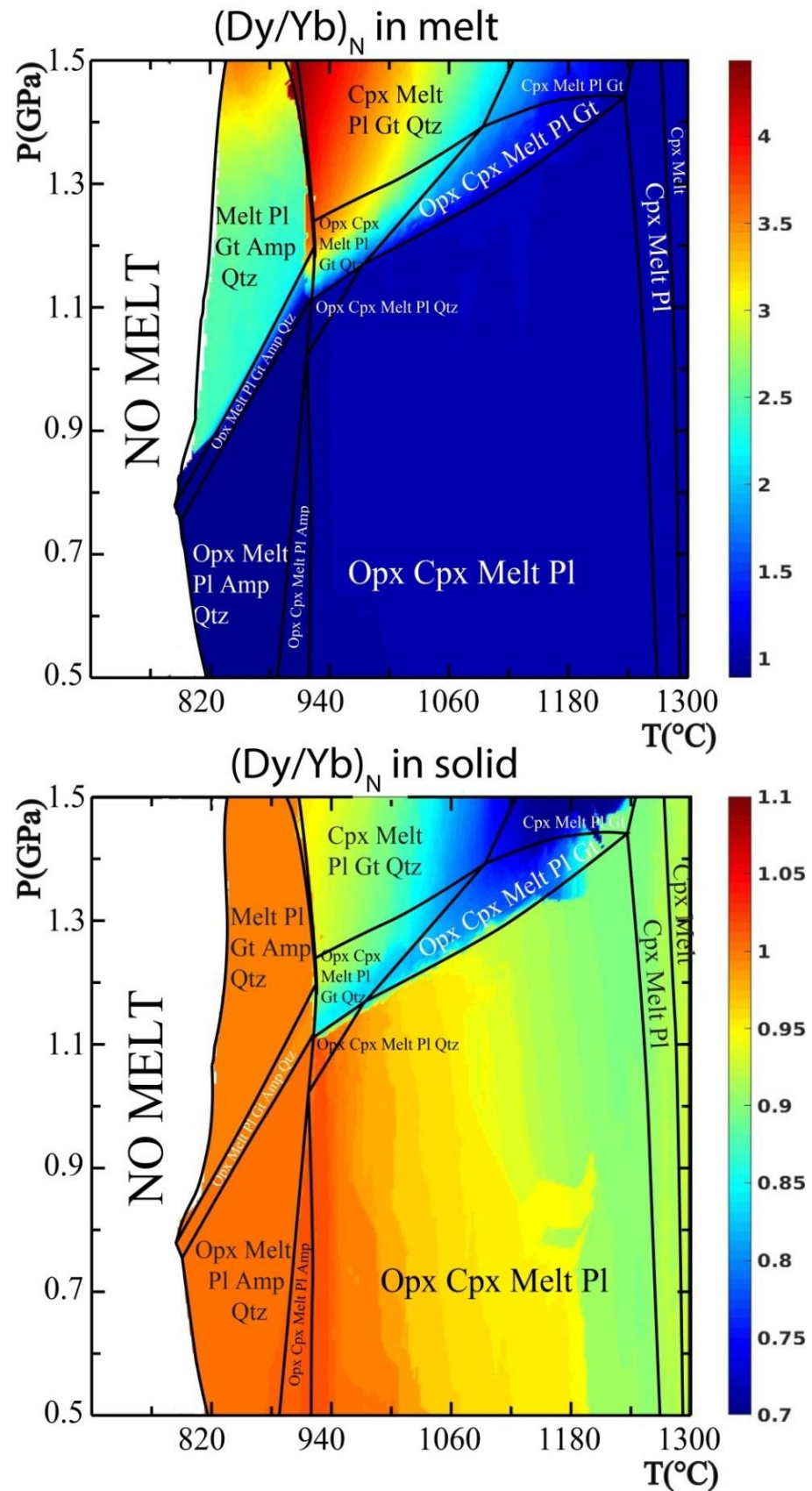
Figure 4-11: *P-T grids of $(\frac{Dy}{Yb})_N$ behaviour in an amphibolite system calculated from the coupling of TEPM and Perple_X. Top: $(\frac{Dy}{Yb})_N$ evolution in the melt (see text for explanations): Bottom: $(\frac{Dy}{Yb})_N$ evolution in the bulk solid (see text for explanations).*

4.5.4   The ratio La/Yb

The normalised against initial concentration ratio $(\frac{La}{Yb})_N$ is commonly used to determine the presence of garnet in the source (see Annexe D for comparison between relative and absolute concentration). Indeed, the HREE Yb is highly compatible in garnet whereas La is highly incompatible (cf., Chapter 3.5). The presence of garnet in the source of magma is therefore related to a depletion of HREE in the sample. Therefore, this study proposes to explore the variation of the La/Yb ratio in a similar manner as Dy/Yb. The results are presented Figure 4.12 and illustrate the variation of the normalised ratio La/Yb in the melt and solid. The reader is again referred to Figure 4.7 and 4.8 to compare the modal proportion and the composition of phases with the P-T grids for La/Yb presented in this section.

In the melt, Figure 4.12 also shows the dominant role of garnet on the ratio at HP conditions, with values reaching $\log_{10}$ (1.6-2), or 60-100. This due to the fact that La is incompatible in all phases and always prefers to remain in the melt and that Yb is highly compatible in gt as well as compatible in amph and cpx. Note again the noticeable decrease of the ratio as gt decreases leading to much lower values of Yb similar to gt-absent conditions (e.g., $\log_{10}$ (0-0.4) or 1-3), thus, suggesting again a modal control on the ratio La/Yb. Indeed, when gt is out at lower pressure, the fractionation of La for Yb is much less pronounced with values of $\log_{10}$ (0-0.4) or 1-3. This accounts for the role of pl that counterAct the role of cpx, meaning that La is more compatible in pl than in cpx and amph, while also Yb is more compatible in cpx and amph than in pl (cf. Chapter 3.1; Figure 4.3).

In the solid, the same conclusions as Dy/Yb can be drawn (Figure 4.12). Firstly, at low melt fraction, (i.e., amph present and LT) the fractionation is low as concentrations of La and Yb are close to the initial concentrations (i.e., $(\frac{La}{Yb})_N \sim 1$). However, the fractionation is more pronounced compared to Dy/Yb (with values of around 0.9-0.8) since La is much less compatible in the solid than Yb. Secondly, at LP and HT conditions, where amph breaks down, the increasing melt content and modal variations seem to control the behaviour of the elements. At HP/HT conditions, the effect of a melt increase is even more pronounced due to the presence of gt. This again relates to Figure 4.10 that shows the evolution of Yb_N versus melt fraction, in which Yb is behaving incompatibly in the solid until the end of the model that is T = 1300°C and P from 0 to 1.5GPa.

Figure 4-12: *P-T grids of $(\frac{La}{Yb})_N$ behaviour in an amphibolite system calculated from the coupling of TEPM and Perple_X. Top figure: $(\frac{La}{Yb})_N$ evolution in the melt on a log_{10} basis (see text for explanations): Bottom figure: $(\frac{La}{Yb})_N$ evolution in the bulk solid (see text for explanations).*

4.5.5   The ratio Sr/Y

The normalised against initial concentration ratio $(\frac{Sr}{Y})_N$ is commonly used to find the amount of plagioclase present in the source magma (see Annexe D for comparison between relative and absolute concentration). As stated before, Sr is compatible in plagioclase whereas Y has a similar behaviour to Yb, so that the ratio $(\frac{Sr}{Y})_N$ provides information on the plagioclase content in the system. The results are presented Figure 4.13 and show the variation of normalised $(\frac{Sr}{Y})_N$ in the melt and the solid. Once again, the reader is referred to Figure 4.7 and 4.8 to compare the modal proportion and the composition of phases with the P-T grids for $(\frac{Sr}{Y})_N$ presented in this section.

In the melt, Figure 4.12 displays a strong influence of plagioclase on the system. Plagioclase is a ubiquitous mineral in the entire grid with a mode ranging from 50wt% to 5-10wt% (see Figure 4.7) Firstly, the effect of pl is clearly observable at LP/HT conditions, where the ratio in the melt is very low while pl is the dominant phase (dark blue domains, Figure 4.13). This is because Sr is hosted by plagioclase and Y is solid incompatible. The ratio slowly increases as the pl fraction decreases and the cpx content rises. This due to a higher compatibility of Y in cpx than Sr. Secondly, at LP/LT conditions, amph slightly increases the ratio as this mineral incorporates more Y, so that the melt is more Y-depleted. Thirdly, while gt is a dominant phase at HP/LT conditions (red domains, Figure 4.13), the ratio increases considerably since this mineral controls the amount of Y leading to a highly depleted melt in Y. In addition, amph is also stable, and amplifies the Y-depletion in the melt. However, as seen in Figure 4.3, plagioclase also controls the relative concentration of Sr at HP and low melt fraction, so that this element is depleted in the melt. Therefore, at LT and HP conditions, the control of garnet, and to some extent that of amphibole, exceeds the control of plagioclase on the ratio $(\frac{Sr}{Y})_N$ by having a stronger impact on the Y content. Finally, at HP/HT conditions, as the fraction of gt decreases progressively at higher T and lower P, the melt progressively regains the pl signature with $(\frac{Sr}{Y})_N$ <1, which enhance the observation made on the effect of gt on this ratio.

Otherwise, in the bulk solid, similar observations than the other ratios can be done. On a first hand, although pl has a strong influence on the behaviour of Sr, the ratio in the solid increases as the melt and cpx fraction increases and the pl content decreases. This, again, recalls to Figure 4.10 that displays the evolution of the relative concentration of Sr and Yb vs the melt content. Yb having a similar behaviour than Y, it can be inferred that the effect of the increase of cpx content enrich the solid in Y. Inversely, the Sr content decreases in the solid as pl declines. However, this has for effect to increase the ratio Sr/Y until the relative concentration of Y is higher than the one of Sr. On another hand, the presence of gt at HP counterAct the one of pl so that the ratio $(\frac{Sr}{Y})_N$ remains close to one. Finally, low fraction of melt at LT neutralises the effect of pl in the bulk solid

for the reasons quoted before (e.g., in solid at low melt fraction, concentration are close to the initial concentration so that $(\frac{Sr}{Y})_N \sim 1$).
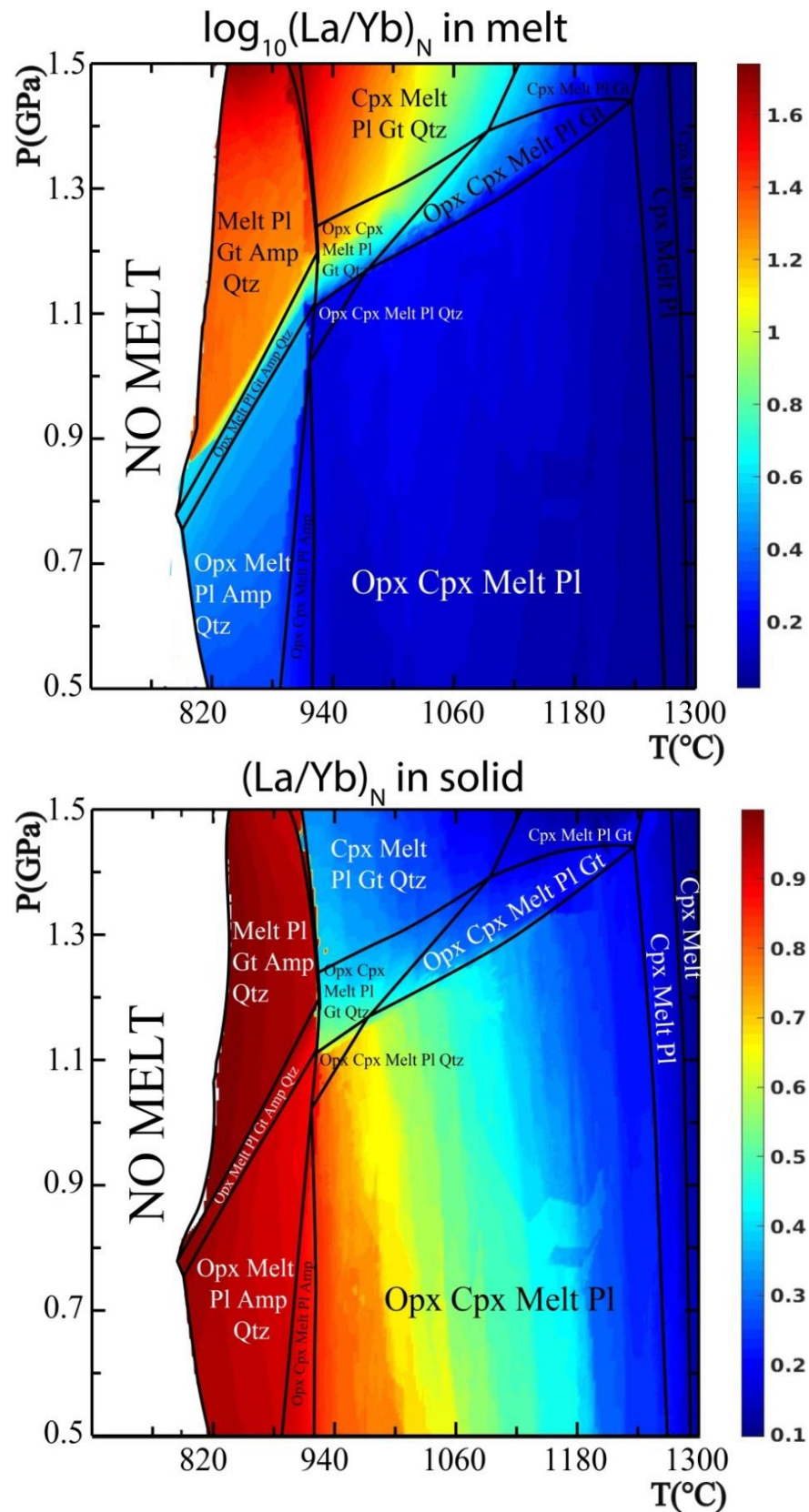

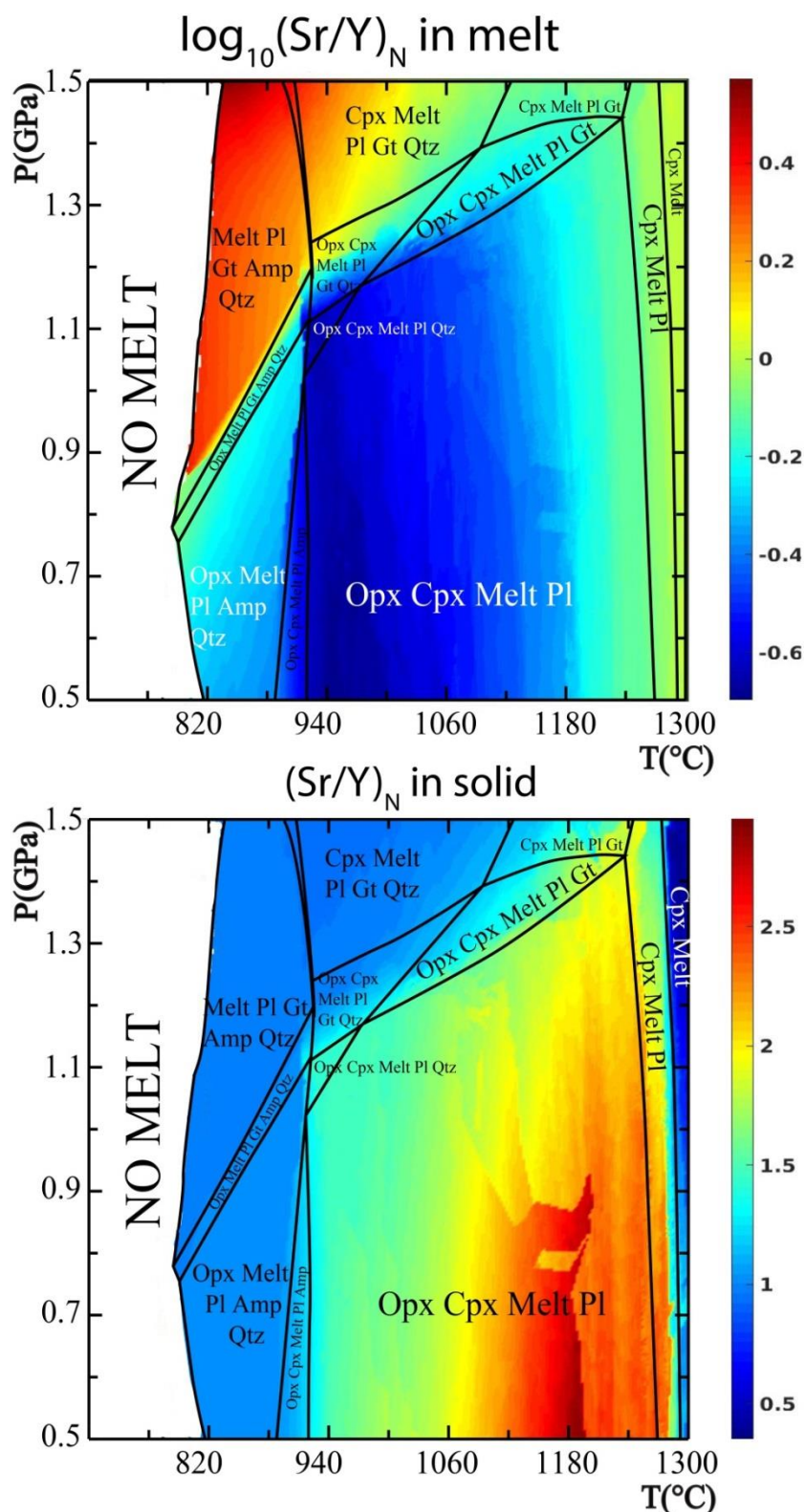**Figure 4-13:** *P-T grids of $(\frac{Sr}{Y})_N$ behaviour in an amphibolite system calculated from the coupling of TEPM and Perple_X. <u>Top figure:</u> $(\frac{Sr}{Y})_N$ evolution in the melt (see text for explanations): <u>Bottom figure:</u> $(\frac{Sr}{Y})_N$ evolution in the bulk solid (see text for explanations). Note that the vertical layering is due to numerical discrepancies from Perple_X and is not related to the use of TEPM.*

4.6 Discussion and Perspectives of application

This thesis presents a Trace Element Partitioning Modelling tool (TEPM) for forward modelling of trace elements in complex systems. Supported by the results of benchmarking, the prediction of trace element behaviour in the partial melting of lower amphibolite crust has been explored using TEPM coupled with Perple_X. A similar study using a peridotite composition is presented in Appendix A. The evolution of normalised Yb and Sr show that the (in)compatibility of the trace elements in the melt varies significantly according to the modal composition of the system and the controlling phases involved. Also, it can give the exact modal composition for which an element is compatible or incompatible in the partial melts by taking into account the effect of all the stable phases. The effect of controlling phases can be observed at a larger scale by using TEPM on the data provided by Perple_X for the entire P-T-X space. Different trace element ratios, important in the deciphering of magmatic processes, are presented. These provide information about the role of the assimilation of the amphibolite lower crust in continental building processes of arc settings (Davidson et al, 2007; Smith et al, 2014, Chiaradia, 2015). The amount of lower crust assimilation and the physical conditions at which the assimilation happens can be investigated by comparing natural data of differentiated products (e.g., granodiorite, tonalite) to the results shown in this study. This will be a subject of further studies.

Further development of a coupling between TEPM and geodynamical numerical codes of melt genesis and transfer will help to understand the effect of other MASH processes on the formation of upper crustal magmatic body. Indeed, the assimilation of the pre-existing mafic/ultramafic lower crust is still thought to be a minor process compared to the contribution of the differentiation of mantle derived mafic melt or the assimilation of metapelites in the mid- and upper crust (e.g. Ducea et al, 2017, Otamendi et al, 2012; Annen et al, 2006). The contribution of mantle derived mafic melts can be quantified using a two-phase flow numerical code simulating porous media flow in partially molten domain using Perple_X (e.g. Bouilhol et al. 2011; Riel et al, in review; McKenzie, 1984). In fact, field investigation in the remnant of arc sections around the world all show metre to kilometre scale intrusions of mafic bodies into more differentiated products (Daczko et al, 2016; Bouilhol et al.2011, Bouilhol et al, 2015; Otamendi et al, 2012; Jagoutz et al, 2006). This is consistent with mass transfer within the lower crust and is commonly attributed to porosity waves of melt migration (Bouilhol et al, 2011; Gerya and Burg, 2007). Hence, the future coupling with such numerical codes will offer a window into dynamic exchange between melt and solid in a porous media that will enable TEPM to capture the trace element signature of the different materials formed by the model.

As such, further improvement of TEPM is needed to quantify all the different melting reactions that define melt genesis, migration and emplacement. First of all, the modal batch melting equation for trace element modelling used so far is not able to model correctly a dynamic

evolution of stable phase modal proportions. Indeed, in nature, a crystal grows incrementally according to the thermal state of the system so that the appearance or disappearance of phases is not an instantaneous process. This is defined in the numerical models of porous flow by the interaction zone (Figure 1.1), in which the melt interact with a small fraction of solid only. One way to measure the progressive evolution of modal proportions is to use non-modal equations for trace element modelling (Shaw, 1970; Hertogen and Gijbels, 1976). Also, a particularity of pervasive processes is the ubiquitous presence of peritectic reactions. For example, the dehydration melting of amphibole gives clinopyroxene + melt so that the modal proportion of amphibole decreases, while that of clinopyroxene increases. Therefore, it is necessary to combine the two processes by using an equation of reactive melt flow for trace element (Reiners, 1998).

It is also shown with Benchmark 2 (Chapter 4.3) and in appendix A that TEPM is able to provide the trace element signature for peridotite partial melts in a similar manner as for an amphibolite system. Hence, the improvement listed above can also be applied to melting processes occurring at mid-ocean ridges (MOR). Indeed, partial melts from upwelling mantle in MORs is thought to be transferred via reactive melt flow through dunite channels thought to control the evolution of the peridotite partial melts to form the representative MOR basalts (MORB) (Suhr, 1999; Liand et al, 2010; Weatherley and Katz, 2012; Tirone et al, 2012; Akisawa et al, 2016). This is supported by field examples of dunite channels in the Oman ophiolite (Kelemen et al, 1995; Braun and Kelemen, 2002), or recent sea expeditions that directly sampled abyssal peridotites and associated MOR products (e.g., dunites, pyroxenites, gabbros) (Warren, 2016). Therefore, the use of TEPM coupled with a model of reactive melt flow might be able to contribute to the current discussion about the garnet signature typical of residual peridotites or MORB (i.e. the high La/Yb ratio) (Workman and Hart, 2005). Indeed, to explain such signatures, the depth of melting of the upwelling mantle is debated to start in the garnet lherzolite field (>85km; Salters and Hart, 1989; Hellebrand et al, 2002). However, this depth of melting would create too much partial melts to explain the current average MORB production (Robinson and Wood, 1998; Klemme and O'Neill; 2000). Some authors also argue that garnet pyroxenite or pyroxenite, stable at lower depths, may explain the La/Yb signature in MORB (Matzen et al, 2017; Blundy et al, 1998; Hirschmann and Stolper, 1996). Hence, the use of TEPM coupled with a numerical model of melt transfer would give new insights on the role of garnet in MOR processes.

In a similar manner and subject to further development, TEPM can be applied to other geological systems such as processes linked with slab dehydration involving partial melting of the mantle wedge (Bouilhol et al, 2015a), slab break-off (Magni et al, 2013, van Hunen and Allen, 2011) or slab penetration or stagnation in the transition zone (Agrusta et al, 2017) using numerical codes for large scale tectonic processes.

Conclusion

In conclusion, this thesis compiled predictive models of trace element partition coefficients for six key minerals in mafic to ultramafic magmatic processes (plagioclase, orthopyroxene, clinopyroxene, garnet, amphibole, olivine) and melts. The models are applicable to 28 different trace elements (Cs, Rb, K, Ba, Sr, REE + Y, Ti, Hf, Zr, U, Th, Ta, Nb). Two types of predictive models are used. First, the lattice strain model is explained and used throughout this thesis. Second, multiple regression analyses from the literature are used that propose predictive models of partition coefficient against multiple chemical/physical variables. In addition, this study derived predictive models for partition coefficients for Ti, Cs, Rb, K, Nb and Ta in garnet, as no such model is yet provided in the literature. Interesting relationships were found between the melt polymerisation and the behaviour of Ti in garnet. Rb and K exhbit dependency on the composition of the X site of garnet so that predictive models are fitted against the X-site composition. There are no extensive datasets of partition coefficients for Cs in garnet. This study proposes to use a representative constant. There is also no relationship between garnet composition or melt polymerisation for the behaviour of Nb and Ta. In that case, an weighted average is done on an extensive set of partition coefficient data (N~50). For amphibole, the models for REE of Tiepolo et al (2007) were fitted against the amount of SiO_2 in the melt, since the melt polymerisation can be described by a linear fit against SiO_2 in the melt. Moreover, in some cases, the predictive models of lattice strain parameters provided by the literature give inaccurate predictions of the trace element behaviour. In such cases, empirical correction factors are added to fit more accurately the data of this study.

The predictive models are compiled into a single code (TEPM), which is able to predict the concentration of trace elements during modal batch melting reactions. The stand-alone version of this tool predicts the behaviour of trace elements in complex melting reactions involving the different minerals explored in this thesis. This was done on partial melting experiments of an amphibolite starting composition and a dry-MORB eclogite. The conclusions of these tests are that, despite the limitations listed in this study (e.g., the effects of redox conditions or accessory phases are not incorporated), the tool is already able to capture essential chemical variations in the minerals and melts, which give acceptable results that can be used for further numerical modelling.

The numerical structure of the tool allows coupling with software that is able to define the modal and chemical compositions of stable phases in P-T-X environments (e.g., Perple_X). Coupled with such software, TEPM gives the trace element behaviour in an entire P-T-X space, which provides insights in trace element signatures of partial melts for specific geological systems. This is

particularly useful as it allows further coupling with numerical models of melt genesis, transfer and emplacement.

Bibliography

Adam, J., Green, T., 2006. Trace element partitioning between mica- and amphibole-bearing garnet lherzolite and hydrous basanitic melt: 1. Experimental results and the investigation of controls on partitioning behaviour. Contrib. to Mineral. Petrol. 152, 1–17. doi:10.1007/s00410-006-0085-4

Agrusta, R., Goes, S., van Hunen, J., 2017. Subducting-slab transition-zone interaction: Stagnation, penetration and mode switches, Earth and Planetary Science Letters. 464. 10-23 doi:10.1016/j.epsl.2017.02.005

Aigner-Torres, M., Blundy, J., Ulmer, P., Pettke, T., 2007. Laser Ablation ICPMS study of trace element partitioning between plagioclase and basaltic melts: An experimental approach. Contrib. to Mineral. Petrol. 153, 647–667. doi:10.1007/s00410-006-0168-2

Akizawa, N., Ozawa, K., Tamura, A., Michibayashi, K., Arai, S., R., M., P., C.S., 2016. Three-dimensional Evolution of Melting, Heat and Melt Transfer in Ascending Mantle beneath a Fast-spreading Ridge Segment Constrained by Trace Elements in Clinopyroxene from Concordant Dunites and Host Harzburgites of the Oman Ophiolite. J. Petrol. 57, 777–814. doi:10.1093/petrology/egw020

Alonso-Perez, R., Müntener, O., Ulmer, P., 2009. Igneous garnet and amphibole fractionation in the roots of island arcs: Experimental constraints on andesitic liquids. Contrib. to Mineral. Petrol. 157, 541–558. doi:10.1007/s00410-008-0351-8

Anderson, D.L., Anderson, O.L., 1970. Brief report: The bulk modulus-volume relationship for oxides. J. Geophys. Res. 75, 3494–3500. doi:10.1029/JB075i017p03494

Annen, C., Blundy, J.D., Sparks, R.S.J., 2006. The genesis of intermediate and silicic magmas in deep crustal hot zones. J. Petrol. 47, 505–539. doi:10.1093/petrology/egi084

Barth, M.G., Foley, S.F., Horn, I., 2002. Partial melting in Archean subduction zones: constraints from experimentally determined trace element partition coefficients between eclogitic minerals and tonalitic melts under upper mantle conditions. Precambrian Res. 113, 323–340. doi:10.1016/S0301-9268(01)00216-9

Baxter, E.F., Scherer, E.E., 2013. Garnet Geochronology: Timekeeper of Tectonometamorphic Processes. Elements. 9. 433-438

Beattie, P., 1994. Systematics and energetics of trace-element partitioning between olivine and silicate melts: Implications for the nature of mineral/melt partitioning. Chem. Geol. 117, 57–71. doi:10.1016/0009-2541(94)90121-X

Bédard, J.H., 2007. Trace element partitioning coefficients between silicate melts and orthopyroxene: Parameterizations of D variations. Chem. Geol. 244, 263–303. doi:10.1016/j.chemgeo.2007.06.019

Bédard, J.H., 2006. Trace element partitioning in plagioclase feldspar. Geochim. Cosmochim. Acta 70, 3717–3742. doi:10.1016/j.gca.2006.05.003

Bédard, J.H., 2005. Partitioning coefficients between olivine and silicate melts. Lithos. 83. 394-419 doi:10.1016/j.lithos.2005.03.011

Bennett, S.L., Blundy, J., Elliott, T., 2004. The effect of sodium and titanium on crystal-melt partitioning of trace elements. Geochim. Cosmochim. Acta 68, 2335–2347. doi:10.1016/j.gca.2003.11.006

Bhagavantam, S., Pantulu, P. V., 1963. Point defects and relaxation phenomena in crystals. Proc. Indian Acad. Sci. - Sect. A 58, 183–196. doi:10.1007/BF03046379

Bindeman, I.N., Davis, A.M., 2000. Trace element partitioning between plagioclase and melt: Investigation of dopant influence on partition behavior. Geochim. Cosmochim. Acta 64, 2863–2878. doi:10.1016/S0016-7037(00)00389-6

Bindeman, I.N., Davis, A.M., Drake, M.J., 1998. Ion microprobe study of plagioclase-basalt partition experiments at natural concentration levels of trace elements. Geochim. Cosmochim. Acta 62, 1175–1193.

Birle JD, Gibbs GV, Moore PB, Smith JV, 1968. Crystal structures of natural olivines. Am. Mineral. 53. 807-824.

Blundy, J., Wood, B., 2003. Partitioning of trace elements between crystals and melts. Earth Planet. Sci. Lett. 210, 383–397. doi:10.1016/S0012-821X(03)00129-8

Blundy, J., Wood, B., 1994. Prediction of crystal-melt partition coefficients from elastic moduli. Nature. 372, 452-454. doi:10.1038/372452a0

Blundy, J.D., Falloon, T.J., Wood, B.J., Dalton, J.A., 1995. Sodium partitioning between clinopyroxene and silicate melts. J. Geophys. Res. Solid Earth 100, 15501–15515. doi:10.1029/95JB00954

Blundy, J.D., Robinson, J.A.C., Wood, B.J., 1998. Heavy REE are compatible in clinopyroxene on the spinel lherzolite solidus. Earth Planet. Sci. Lett. 160, 493–504. doi:10.1016/S0012-821X(98)00106-X

Blundy, J.D., Wood, B.J., 2003. Mineral-melt partitioning of uranium, thorium, and their daughters. Rev. Mineral. Geochemistry 52, 59–123. doi:10.2113/0520059

Blundy, J.D., Wood, B.J., 1991. Crystal-chemical controls on the partitioning of Sr and Ba between plagioclase feldspar, silicate melts, and hydrothermal solutions. Geochim. Cosmochim. Acta 55, 193–209. doi:10.1016/0016-7037(91)90411-W

Bottazzi, P., Tiepolo, M., Vannucci, R., Zanetti, A., Brumm, R., Foley, S.F., Oberti, R., 1999. Distinct site preferences for heavy and light REE in amphibole and the prediction of Amph/L D REE. Contrib. to Mineral. Petrol. 137, 36–45. doi:10.1007/s004100050580

Bouilhol, P., Connolly, J.A.D., Burg, J.P., 2011a. Geological evidence and modeling of melt migration by porosity waves in the sub-arc mantle of Kohistan (Pakistan). Geology 39, 1091–1094. doi:10.1130/G32219.1

Bouilhol, P., Magni, V., van Hunen, J., Kaislaniemi, L., 2015. A numerical approach to melting in warm subduction zones, Earth and Planetary Science Letters. 411, 37-44. doi:10.1016/j.epsl.2014.11.043

Bouilhol, P., Schaltegger, U., Chiaradia, M., Ovtcharova, M., Stracke, A., Burg, J.P., Dawood, H., 2011b. Timing of juvenile arc crust formation and evolution in the Sapat Complex (Kohistan-Pakistan). Chem. Geol. 280, 243–256. doi:10.1016/j.chemgeo.2010.11.013

Bouilhol, P., Schmidt, M.W., Burg, J.-P.P., 2014. Magma transfer and evolution in channels within the arc crust: The pyroxenitic feeder pipes of Sapat (Kohistan, Pakistan). J. Petrol. 56, 1309–1342. doi:10.1093/petrology/egv037

Bowen, N.L., 1915. The Later Stages of the Evolution of the Igneous Rocks. J. Geol. 23, 1–91. doi:10.1086/622298

Bragg, W.L., Williams, E.J., 1934. The Effect of Thermal Agitation on Atomic Arrangement in Alloys. Proc. R. Soc. London. Ser. A, Contain. Pap. a Math. Phys. Character 145, 699–730. doi:10.2307/2935535

Braun, M.G., Kelemen, P.B., 2002. Dunite distribution in the Oman Ophiolite: Implications for melt flux through porous dunite conduits. Geochemistry, Geophys. Geosystems 3, 1–21. doi:10.1029/2001GC000289

Brice, J.C., 1975. Some thermodynamic aspects of the growth of strained crystals. J. Cryst. Growth 28, 249–253. doi:10.1016/0022-0248(75)90241-9

Brown, J.M., Angel, R.J., Ross, N.L., 2016. Elasticity of plagioclase feldspars. J. Geophys. Res. Solid Earth 121, 663–675. doi:10.1002/2015JB012736

Butler, J.R., Skiba, W., 1962. Strontium in plagioclase feldspars from four layered basic masses in Somalia.

Cameron, M., Papike, J.J., 1981. Structural and chemical variations in pyroxene. Am. Mineral. 66, 1–50.

Chao, E.C.T., Back, J.M., Minkin, J.A., Yinchen, R., 1992. Host-rock controlled epigenetic, hydrothermal metasomatic origin of the Bayan Obo REEFe-Nb ore deposit, Inner Mongolia, P.R.C. Appl. Geochemistry 7, 443–458. doi:10.1016/0883-2927(92)90005-N

Chiaradia, M., 2015. Crustal thickness control on Sr/Y signatures of recent arc magmas: an Earth scale perspective 5, 8115-8117.

Coleman, R.G., Lee, D.E., Beatty, L.B., Brannock, W.W., 1965. Eclogites and Eclogites: Their Differences and Similarities. Geol. Soc. Am. Bull. 76, 483. doi:10.1130/0016-7606(1965)76[483:EAETDA]2.0.CO;2

Condie, K.C., Selverstone, J., 1999. The Crust of the Colorado Plateau: New Views of an Old Arc. J. Geol. 107, 387–397. doi:10.1086/314363

Connolly, J.A.D., 2005. Computation of phase equilibria by linear programming: A tool for geodynamic modeling and its application to subduction zone decarbonation. Earth Planet. Sci. Lett. 236, 524–541. doi:10.1016/j.epsl.2005.04.033

Connolly, J.A.D., Schmidt, M.W., Solferino, G., Bagdassarov, N., 2009. Permeability of asthenospheric mantle and melt extraction rates at mid-ocean ridges. Nature 462, 209–212. doi:10.1038/nature08517

Daczko, N.R., Piazolo, S., Meek, U., Stuart, C.A., Elliott, V., 2016. Hornblendite delineates zones of mass transfer through the lower crust. Sci. Rep. 6, 31369. doi:10.1038/srep31369

Dalpé, C., Baker, R.D., Baker, D.R., 2000. Experimental investigation of large-ion-lithophile-element- , between calcic amphibole and basaltic melt : the effects of pressure and oxygen fugacity. Contrib. to Mineral. Petrol. 140, 233–250. doi:10.1007/s004100000181

Davidson, J., Turner, S., Handley, H., Macpherson, C., Dosseto, A., 2007. Amphibole "sponge" in arc crust? Geology 35, 787–790. doi:10.1130/G23637A.1

Dawson, J.B., Hinton, R.W., 2003. Trace-element content and partitioning in calcite, dolomite and apatite in carbonatite, Phalaborwa, South Africa. Mineral. Mag. 67, 921–930. doi:10.1180/0026461036750151

Deer, W.A., Howie, R.A., Zussman, J., Deer, W.A., 1963. Rock-forming minerals. 1 (1963). Ortho-and ring silicates. Longmans.

Dohmen, R., Blundy, J., 2014. A predictive thermodynamic model for element partitioning between plagioclase and melt as a function of pressure, temperature and composition. Am. J. Sci. 314, 1319–1372. doi:10.2475/09.2014.04

Dragovic, B., Samanta, L.M., Baxter, E.F., Selverstone, J., 2012. Using garnet to constrain the duration and rate of water-releasing metamorphic reactions during subduction: An example from Sifnos, Greece. Chem. Geol. 314, 9–22. doi:10.1016/j.chemgeo.2012.04.016

Drake, M.J., 1975. The oxidation state of europium as an indicator of oxygen fugacity. Geochim. Cosmochim. Acta 39, 55–64. doi:10.1016/0016-7037(75)90184-2

Drake, M.J., Weill, D.F., 1975. Partition of Sr, Ba, Ca, Y, Eu2+, Eu3+, and other REE between plagioclase feldspar and magmatic liquid: an experimental study. Geochim. Cosmochim. Acta 39, 689–712. doi:10.1016/0016-7037(75)90011-3

Draper, D.S., van Westrenen, W., 2007. Quantifying garnet-melt trace element partitioning using lattice-strain theory: assessment of statistically significant controls and a new predictive model. Contrib. to Mineral. Petrol. 154, 731–746. doi:10.1007/s00410-007-0235-3

Ducea, M., Saleeby, J., 1998. A Case for Delamination of the Deep Batholithic Crust beneath the Sierra Nevada, California. Int. Geol. Rev. 40, 78–93. doi:10.1080/00206819809465199

Ducea, M.N., Bergantz, G.W., Crowley, J.L., Otamendi, J., 2017. Ultrafast magmatic buildup and diversification to produce continental crust during subduction. Geology 45, 235–238. doi:10.1130/G38726.1

Ducea, M.N., Saleeby, J.B., 1998. The age and origin of a thick mafic?ultramafic keel from beneath the Sierra Nevada batholith. Contrib. to Mineral. Petrol. 133, 169–185. doi:10.1007/s004100050445

Dunn, T., Sen, C., 1994. Mineral/matrix partition coefficients for orthopyroxene, plagioclase, and olivine in basaltic to andesitic systems: A combined analytical and experimental study. Geochim. Cosmochim. Acta 58, 717–733. doi:10.1016/0016-7037(94)90501-0

Foley, S., Tiepolo, M., Vannucci, R., 2002. Growth of early continental crust controlled by melting of amphibolite in subduction zones. Nature 417, 837–840. doi:10.1038/nature00799

Foley, S.F., Barth, M.G., Jenner, G.A., 2000. Rutile/melt partition coefficients for trace elements and an assessment of the influence of rutile on the trace element characteristics of subduction zone magmas. Geochim. Cosmochim. Acta 64, 933–938. doi:10.1016/S0016-7037(99)00355-5

Frei, Dirk, Axel Liebscher, Gerhard Franz, Bernd Wunder, Stephan Klemme, and Jon Blundy. 2008. 'Trace Element Partitioning between Orthopyroxene and Anhydrous Silicate Melt on the Lherzolite Solidus from 1.1 to 3.2 GPa and 1,230 to 1,535C in the Model System Na2O--CaO--MgO--Al2O3--SiO2'. *Contributions to Mineralogy and Petrology* 157 (4). Springer-Verlag: 473–90. doi:10.1007/s00410-008-0346-5.

Fujimaki, H., 1986. Partition coefficients of Hf, Zr, and REE between zircon, apatite, and liquid. Contrib. to Mineral. Petrol. 94, 42–45. doi:10.1007/BF00371224

Gaetani, G.A., 2004. The influence of melt structure on trace element partitioning near the peridotite solidus. Contrib. to Mineral. Petrol. 147, 511–527. doi:10.1007/s00410-004-0575-1

Gaetani, G.A., Kent, A.J.R., Grove, T.L., Hutcheon, I.D., Stolper, E.M., 2003. Mineral/melt partitioning of trace elements during hydrous peridotite partial melting. Contrib. to Mineral. Petrol. 145, 391–405. doi:10.1007/s00410-003-0447-0

Geller, S., 1967. Crystal chemistry of the garnet. Zeitschrift fur Krist. - Cryst. Mater. 125, 1–47. doi:10.1524/zkri.1967.125.16.1

Gerya, T. V., Burg, J.-P., 2007. Intrusion of ultramafic magmatic bodies into the continental crust: Numerical simulation. Phys. Earth Planet. Inter. 160, 124–142. doi:10.1016/j.pepi.2006.10.004

Goldschmidt, V.M., 1937. The principles of distribution of chemical elements in minerals and rocks. The seventh Hugo Müller Lecture, delivered before the Chemical Society. J. Chem. Soc. 0, 655–673. doi:10.1039/jr9370000655

Green, E.C.R., White, R.W., Diener, J.F.A., Powell, R., Holland, T.J.B., Palin, R.M., 2016. Activity-composition relations for the calculation of partial melting equilibria in metabasic rocks. J. Metamorph. Geol. 34, 845–869. doi:10.1111/jmg.12211

Green, T.., Blundy, J.., Adam, J.., Yaxley, G.., 2000. SIMS determination of trace element partition coefficients between garnet, clinopyroxene and hydrous basaltic liquids at 2–7.5 GPa and 1080–1200°C. Lithos 53, 165–187. doi:10.1016/S0024-4937(00)00023-2

Hacker, B.R., 2008. H_2O subduction beyond arcs. Geochemistry, Geophys. Geosystems 9, 1-24. doi:10.1029/2007GC001707

Hart, S.R., Dunn, T., 1993. Experimental cpx/melt partitioning of 24 trace elements. Contrib. to Mineral. Petrol. 113, 1–8. doi:10.1007/BF00320827

Hauri, E.H., Wagner, T.P., Grove, T.L., 1994. Experimental and natural partitioning of Th, U, Pb and other trace elements between garnet, clinopyroxene and basaltic melts. Chem. Geol. 117, 149–166. doi:10.1016/0009-2541(94)90126-0

Hawthorne, F.C., Oberti, R., 2007. Amphibole: Crystal Chemistry. Rev. Mineral. Geochemistry 67, 1-54.

Hazen, R.M., Finger, L.W., 1979. Bulk modulus—volume relationship for cation-anion polyhedra. J. Geophys. Res. 84, 6723. doi:10.1029/JB084iB12p06723

Hebert, L.B., Montasi, L.G.J., 2010. Generation of permeability barriers during melt extraction at mid-ocean ridges. Geochemistry, Geophys. Geosystems 11, 1-17. doi:10.1029/2010GC003270

Hellebrand, E., Snow, J.E., Hoppe, P., Hofmann, a W., 2002. Garnet-field melting and late-stage refertilization in "residual" abyssal peridotites from the Central Indian Ridge. J. Petrol. 43, 2305–2338. doi:10.1093/petrology/43.12.2305

Hertogen, J., Gijbels, R., 1976. Calculation of trace element fractionation during partial melting. Geochim. Cosmochim. Acta 40, 313–322. doi:10.1016/0016-7037(76)90209-X

Herzberg, C., Zhang, J., 1996. Melting experiments on anhydrous peridotite KLB-1: Compositions of magmas in the upper mantle and transition zone. J. Geophys. Res. 101, 8271. doi:10.1029/96JB00170

Hildreth, W., Moorbath, S., 1988. Crustal contributions to arc magmatism in the Andes of Central Chile. Contrib. to Mineral. Petrol. 98, 455–489. doi:10.1007/BF00372365

Hill, E., Blundy, J.D., Wood, B.J., 2011. Clinopyroxene-melt trace element partitioning and the development of a predictive model for HFSE and Sc. Contrib. to Mineral. Petrol. 161, 423–438. doi:10.1007/s00410-010-0540-0

Hill, E., Wood, B.J., Blundy, J.D., 2000. The effect of Ca-Tschermaks component on trace element partitioning between clinopyroxene and silicate melt. Lithos 53, 203–215. doi:10.1016/S0024-4937(00)00025-6

Hirschmann, M.M., Stolper, E.M., 1996. A possible role for garnet pyroxenite in the origin of the "garnet signature" in MORB. Contrib. to Mineral. Petrol. 124, 185–208. doi:10.1007/s004100050184

Holland, T.J.B., Powell, R., 2011. An improved and extended internally consistent thermodynamic dataset for phases of petrological interest, involving a new equation of state for solids. J. Metamorph. Geol. 29, 333–383. doi:10.1111/j.1525-1314.2010.00923.x

Huggins, F.E., Virgo, D., Huckenholz, H.G., 1977. Titanium-containing silicate garnet; II, The crystal chemistry of melanites and schorlomites. Am. Mineral. 62.

Humphreys, E., 2009. Relation of flat subduction to magmatism and deformation in the western United States. Geol. Soc. Am. Mem. 204, 85–98. doi:10.1130/2009.1204(04)

Jagoutz, O., Kelemen, P.B., 2015. Role of Arc Processes in the Formation of Continental Crust. Annu. Rev. Earth Planet. Sci. 43, 363–404. doi:10.1146/annurev-earth-040809-152345

Jagoutz, O., Müntener, O., Burg, J.P., Ulmer, P., Jagoutz, E., 2006. Lower continental crust formation through focused flow in km-scale melt conduits: The zoned ultramafic bodies of the Chilas Complex in the Kohistan island arc (NW Pakistan). Earth Planet. Sci. Lett. 242, 320–342. doi:10.1016/j.epsl.2005.12.005

Jagoutz, O., Müntener, O., Schmidt, M.W., Burg, J.-P.P., 2011. The roles of flux- and decompression melting and their respective fractionation lines for continental crust formation: Evidence from the Kohistan arc. Earth Planet. Sci. Lett. 303, 25–36. doi:10.1016/j.epsl.2010.12.017

Jagoutz, O., Müntener, O., Ulmer, P., Pettke, T., Burg, J.-P., Dawood, H., Hussain, S., 2007. Petrology and Mineral Chemistry of Lower Crustal Intrusions: the Chilas Complex, Kohistan (NW Pakistan). J. Petrol. 48, 1895–1953. doi:10.1093/petrology/egm044

Jennings, E.S., Holland, T.J.B., 2015. A simple thermodynamic model for melting of peridotite in the system NCFMASOCr. J. Petrol. 56, 869–892. doi:10.1093/petrology/egv020

John, T., Klemd, R., Klemme, S., Pfänder, J.A., Hoffmann, J.E., Gao, J., 2011. Nb-Ta fractionation by partial melting at the titanite-rutile transition. Contrib. to Mineral. Petrol. 161, 35–45. doi:10.1007/s00410-010-0520-4

Johnson, K.T.M., 1998. Experimental determination of partition coefficients for rare earth and high-field-strength elements between clinopyroxene, garnet, and basaltic melt at high pressures. Contrib. to Mineral. Petrol. 133, 60–68. doi:10.1007/s004100050437

Karakas, O., Dufek, J., Mangan, M.T., Wright, H.M., Bachmann, O., 2017. Thermal and petrologic constraints on lower crustal melt accumulation under the Salton Sea Geothermal Field, Earth and Planetary Science Letters. 467, 10-17. doi:10.1016/j.epsl.2017.02.027

Kelemen, P.B., Shimizu, N., Dunn, T., 1993. Relative depletion of niobium in some arc magmas and the continental crust: partitioning of K, Nb, La and Ce during melt/rock reaction in the upper mantle. Earth Planet. Sci. Lett. 120, 111–134. doi:10.1016/0012-821X(93)90234-Z

Kelemen, P.B., Shimizu, N., Salters, V.J.M., 1995. Extraction of mid-ocean-ridge basalt from the upwelling mantle by focused flow of melt in dunite channels. Nature 375, 747–753. doi:10.1038/375747a0

Kinzler, R.J., Grove, T.L., 1992. Primary magmas of mid-ocean ridge basalts 1. Experiments and methods. J. Geophys. Res. 97, 6885. doi:10.1029/91JB02840

Klemme, S., Blundy, J.D., Wood, B.J., 2002. Experimental constraints on major and trace element partitioning during partial melting of eclogite. Geochim. Cosmochim. Acta 66, 3109–3123. doi:10.1016/S0016-7037(02)00859-1

Klemme, S., O'Neill, H.S., 2000. The near-solidus transition from garnet lherzolite to spinel lherzolite. Contrib. to Mineral. Petrol. 138, 237–248. doi:10.1007/s004100050560

Klemme, S., Prowatke, S., Hametner, K., Günther, D., 2005. Partitioning of trace elements between rutile and silicate melts: Implications for subduction zones. Geochim. Cosmochim. Acta 69, 2361–2371. doi:10.1016/j.gca.2004.11.015

Kovalenko, V.I., Kozlovsky, A.M., Yarmolyuk, V. V., 2009. Trace element ratios as indicators of source mixing and magma differentiation of alkali granitoids and basites of the Haldzan-Buregtey massif and the Haldzan-Buregtey rare-metal deposit, western Mongolia. Petrology 17, 158–177. doi:10.1134/S0869591109020040

Kratzmann, D.J., Carey, S., Scasso, R.A., Naranjo, J.-A., 2010. Role of cryptic amphibole crystallization in magma differentiation at Hudson volcano, Southern Volcanic Zone, Chile. Contrib. to Mineral. Petrol. 159, 237–264. doi:10.1007/s00410-009-0426-1

Kroll, H., Lueder, T., Schlenz, H., Kirfel, A., Vad, T., 1997. The Fe2+ ,Mg distribution in orthopyroxene: A critical assessment of its potential as a geospeedometer. Eur. J. Mineral. 9, 705–733. doi:10.1127/ejm/9/4/0705

Lallemand, S., Heuret, A., Boutelier, D., 2005. On the relationships between slab dip, back-arc stress, upper plate absolute motion, and crustal nature in subduction zones. Geochemistry, Geophys. Geosystems 6. doi:10.1029/2005GC000917

Landwehr, D., Blundy, J., Chamorro-Perez, E.M., Hill, E., Wood, B., 2001. U-series disequilibria generated by partial melting of spinel lherzolite. Earth Planet. Sci. Lett. 188, 329–348. doi:10.1016/S0012-821X(01)00328-4

Larocque, J., Canil, D., 2010. The role of amphibole in the evolution of arc magmas and crust: the case from the Jurassic Bonanza arc section, Vancouver Island, Canada. Contrib. to Mineral. Petrol. 159, 475–492. doi:10.1007/s00410-009-0436-z

Lasaga, A.C., 1981. Atomistic basis of kinetics: defects in minerals. Rev. Miner. (United States) 8, 261-316.

Law, K.M., Blundy, J.D., Wood, B.J., Ragnarsdottir, K. V., 2000. Trace element partitioning between wollastonite and silicate-carbonate melt. Mineral. Mag. 64, 651–661. doi:10.1180/002646100549670

Leake, B.E., Woolley, A.R., Arps, C.E.S., Birch, W.D., Gilbert, M.C., Grice, J.D., Hawthorne, F.C., Kato, A., Kisch, H.J., Krivovichev, V.G., Linthout, K., Laird, J., Mandarino, J., Maresch, W. V., Nickel, E.H., Rock, N.M.S., Schumacher, J.C., Smith, D.C., Stephenson, N.C.N., Ungaretti, L., Whittaker, E.J.W., Youzhi, G., 1997. Nomenclature of Amphibole: Report of the Subcommittee on Amphibole of the International Mineralogical Association Commission on New Minerals and Mineral Names. Mineral. Mag. 61, 295–321. doi:10.1180/minmag.1997.061.405.13

Liang, Y., Schiemenz, A., Hesse, M.A., Parmentier, E.M., Hesthaven, J.S., 2010. High-porosity channels for melt migration in the mantle: Top is the dunite and bottom is the harzburgite and lherzolite. Geophys. Res. Lett. 37, 1-5. doi:10.1029/2010GL044162

Lissenberg, C.J., MacLeod, C.J., 2016. A Reactive Porous Flow Control on Mid-ocean Ridge Magmatic Evolution. J. Petrol. 57, 2195–2220. doi:10.1093/cercor/bhw393

Lizarralde, D., Gaherty, J.B., Collins, J.A., Hirth, G., Kim, S.D., 2004. Spreading-rate dependence of melt extraction at mid-ocean ridges from mantle seismic refraction data. Nature 432, 744–747. doi:10.1038/nature03140

Luhr, J.F., Carmichael, I.S.E., 1980. The Colima Volcanic complex, Mexico. Contrib. to Mineral. Petrol. 71, 343–372. doi:10.1007/BF00374707

Lumpkin, G.R., Ribbe, P.H., Lumpkin, N.E., 1983. Composition, order-disorder and lattice parameters of olivine; determinative methods for Mg-Mn and Mg-Ca silicate olivine. Am. Mineral. 68.

Macdonald, K.C., 1982. Mid-Ocean Ridges: Fine Scale Tectonic, Volcanic and Hydrothermal Processes Within the Plate Boundary Zone. Annu. Rev. Earth Planet. Sci. 10, 155–190. doi:10.1146/annurev.ea.10.050182.001103

Magni, V., Faccenna, C., van Hunen, J., Funiciello, F., 2013. Delamination vs. break-off: the fate of continental collision. Geophys. Res. Lett. 40, 285–289. doi:10.1002/grl.50090

Mahood, G., Hildreth, W., 1983. Large partition coefficients for trace elements in high-silica rhyolites. Geochim. Cosmochim. Acta 47, 11–30. doi:10.1016/0016-7037(83)90087-X

Mallard, C., Coltice, N., Seton, M., Müller, R.D., Tackley, P.J., 2016. Subduction controls the distribution and fragmentation of Earth's tectonic plates. Nature 535, 140–143. doi:10.1038/nature17992

Matzen, A.K., Wood, B.J., Baker, M.B., Stolper, E.M., 2017. The roles of pyroxenite and peridotite in the mantle sources of oceanic basalts. Nat. Geosci. 10, 530-535.

McDade, P., Blundy, J.D., Wood, B.J., 2003. Trace element partitioning on the Tinaquillo Lherzolite solidus at 1.5GPa. Phys. Earth Planet. Inter. 139, 129–147. doi:10.1016/S0031-9201(03)00149-3

McDonough, W.F., Sun, S. s., 1995. The composition of the Earth. Chem. Geol. 120, 223–253. doi:10.1016/0009-2541(94)00140-4

McKenzie, D., 1984. The Generation and Compaction of Partially Molten Rock. J. Petrol. 25, 713–765. doi:10.1093/petrology/25.3.713

Megaw, H.D., Kempster, C.J.E., Radoslovich, E.W., 1962. The structure of anorthite, CaAl2Si2O8. II. Description and discussion. Acta Crystallogr. 15, 1017–1035.

Menard, T., Spear, F.S., 1996. Interpretation of plagioclase zonation in calcic pelitic schist, south Strafford, Vermont, and the effects on thermobarometry. Can. Mineral. 34, 133-146.

Mibe, K., Orihashi, Y., Nakai, S., Fujii, T., 2006. Element partitioning between transition-zone minerals and ultramafic melt under hydrous conditions. Geophys. Res. Lett. 33, L16307, 1-6. doi:10.1029/2006GL026999

Moresi, L., Gurnis, M., 1996. Constraints on the lateral strength of slabs from three-dimensional dynamic flow models. Earth Planet. Sci. Lett. 138, 15–28. doi:10.1016/0012-821X(95)00221-W

Morgan, J.W., Anders, E., 1980. Chemical composition of Earth, Venus, and Mercury. Proc. Natl. Acad. Sci. U. S. A. 77, 6973–6977. doi:10.1073/pnas.77.12.6973

Morra, G., Regenauer-Lieb, K., Giardini, D., 2006. Curvature of oceanic arcs. Geology 34, 877. doi:10.1130/G22462.1

Moyen, J.-F., Stevens, G., 2006. Experimental constraints on TTG petrogenesis: Implications for Archean geodynamics. American Geophysical Union, pp. 149–175. doi:10.1029/164GM11

Mysen, B.O., Toplis, M.J., 2007. Structural behavior of Al3+ in peralkaline, metaluminous, and peraluminous silicate melts and glasses at ambient pressure. Am. Mineral. 92, 933–946. doi:10.2138/am.2007.2334

Mysen, B.O., Virgo, D., Seifert, F.A., 1985. Relationships between properties and structure of aluminosilicate melts. Am. Mineral. 70, 88–105.

Mysen, B.O., Virgo, D., Seifert, F.A., 1982. The structure of silicate melts: Implications for chemical and physical properties of natural magma. 20, 353-383. Rev. Geophys. doi:10.1029/RG020i003p00353

Nandedkar, R.H., Hürlimann, N., Ulmer, P., Müntener, O., 2016. Amphibole-melt trace element partitioning of fractionating calc-alkaline magmas in the lower crust: an experimental study. Contrib. to Mineral. Petrol. 171, 71. doi:10.1007/s00410-016-1278-0

Nandedkar, R.H., Ulmer, P., Müntener, O., 2014. Fractional crystallization of primitive, hydrous arc magmas: An experimental study at 0.7 GPa. Contrib. to Mineral. Petrol. 167, 1–27. doi:10.1007/s00410-014-

1015-5

Narduzzi, F., Farina, F., Stevens, G., Lana, C., Nalini, H.A., 2017. Magmatic garnet in the Cordilleran-type Galiléia granitoids of the Araçuaí belt (Brazil): Evidence for crystallization in the lower crust. Lithos 282, 82–97. doi:10.1016/j.lithos.2017.02.017

Nasagawa, H., 1966. Trace element partition coefficient in ionic crystals. Science (80-.). 152, 767–769.

Nash, W.P., Crecraft, H.R., 1985. Partition coefficients for trace elements in silicic magmas. Geochim. Cosmochim. Acta 49, 2309–2322. doi:10.1016/0016-7037(85)90231-5

Nelson, S., Lindroth, D., Blake, R., 1989. Dielectric properties of selected minerals at 1 to 22 GHz. GEOPHYSICS 54, 1344–1349. doi:10.1190/1.1442596

Nielsen, R.L., 1985. A method for the elimination of the compositional dependence of trace element distribution coefficients. Geochim. Cosmochim. Acta 49, 1775–1779. doi:10.1016/0016-7037(85)90148-6

Nielsen, R.L., Beard, J.S., 2000. Magnetite-melt HFSE partitioning. Chem. Geol. 164, 21–34. doi:10.1016/S0009-2541(99)00139-4

Nielsen, R.L., Dungan, M.A., 1983. Low pressure mineral-melt equilibria in natural anhydrous mafic systems. Contrib. to Mineral. Petrol. 84, 310–326. doi:10.1007/BF01160284

Niu, Y., O'Hara, M.J., 2009. MORB mantle hosts the missing Eu (Sr, Nb, Ta and Ti) in the continental crust: New perspectives on crustal growth, crust-mantle differentiation and chemical structure of oceanic upper mantle. Lithos 112, 1–17. doi:10.1016/j.lithos.2008.12.009

Nter Suhr, G., 1999. Melt Migration under Oceanic Ridges: Inferences from Reactive Transport Modelling of Upper Mantle Hosted Dunites. J. Petrol. 40, 575–599.

Olin, P.H., Wolff, J.A., 2012. Partitioning of rare earth and high field strength elements between titanite and phonolitic liquid. Lithos 128–131, 46–54. doi:10.1016/j.lithos.2011.10.007

Olin, P.H., Wolff, J.A., 2010. Rare earth and high field strength element partitioning between iron-rich clinopyroxene and felsic liquids. Contrib. to Mineral. Petrol. 160, 761–775. doi:10.1007/s00410-010-0506-2

Onuma, N., Higuchi, H., Wakita, H., Nagasawa, H., 1968. Trace element partition between two pyroxene and the host lava. Earth Planet. Sci. Lett. 5, 47–51. doi:10.1016/S0012-821X(68)80010-X

Otamendi, J.E., Ducea, M.N., Bergantz, G.W., 2012. Geological, Petrological and Geochemical Evidence for Progressive Construction of an Arc Crustal Section, Sierra de Valle Fertil, Famatinian Arc, Argentina. J. Petrol. 53, 761–800. doi:10.1093/petrology/egr079

Papike, J.J., Cameron, M., 1976. Crystal chemistry of silicate minerals of geophysical interest. Rev. Geophys. 14,37-80 doi:10.1029/RG014i001p00037

Patiño Douce, A.E., Johnston, A.D., 1991. Phase equilibria and melt productivity in the pelitic system: implications for the origin of peraluminous granitoids and aluminous granulites. Contrib. to Mineral. Petrol. 107, 202–218. doi:10.1007/BF00310707

Pertermann, M., Hirschmann, M.M., Hametner, K., Gülnther, D., Schmidt, M.W., 2004. Experimental determination of trace element partitioning between garnet and silica-rich liquid during anhydrous partial melting of MORB-like eclogite. Geochemistry, Geophys. Geosystems 5, 2125. doi:10.1029/2003GC000638

Profeta, L., Ducea, M.N., Chapman, J.B., Paterson, S.R., Gonzales, S.M.H., Kirsch, M., Petrescu, L., DeCelles, P.G., 2015. Quantifying crustal thickness over time in magmatic arcs. Sci. Rep. 5, 17786. doi:10.1038/srep17786

Prowatke, S., Klemme, S., 2005. Effect of melt composition on the partitioning of trace elements between titanite and silicate melt. Geochim. Cosmochim. Acta 69, 695–709. doi:10.1016/j.gca.2004.06.037

Qian, Q., Hermann, J., 2013. Partial melting of lower crust at 10-15 kbar: Constraints on adakite and TTG

formation. Contrib. to Mineral. Petrol. 165, 1195–1224. doi:10.1007/s00410-013-0854-9

Rapp, R.P., Watson, E.B., Miller, C.F., 1991. Partial melting of amphibolite/eclogite and the origin of Archean trondhjemites and tonalites. Precambrian Res. 51, 1–25. doi:10.1016/0301-9268(91)90092-O

Reiners, P.W., 1998. Reactive melt transport in the mantle and geochemical signatures of mantle-derived magmas. J. Petrol. 39, 1039–1061. doi:10.1093/petrology/39.5.1039

Riel, N., Mercier, J., Weinberg, R., 2016. Convection in a partially molten metasedimentary crust? Insights from the El Oro complex (Ecuador). Geology 44, 31–34. doi:10.1130/G37208.1

Robinson, J.A.C., Wood, B.J., 1998. The depth of the spinel to garnet transition at the peridotite solidus. Earth Planet. Sci. Lett. 164, 277–284. doi:10.1016/S0012-821X(98)00213-1

Rudnick, R.L., Gao, S., 2003. Composition of the Continental Crust, in: Treatise on Geochemistry. Elsevier, pp. 1–64. doi:10.1016/B0-08-043751-6/03016-4

Salters, V.J.M., Hart, S.R., 1989. The hafnium paradox and the role of garnet in the source of mid-ocean-ridge basalts. Nature 342, 420–422. doi:10.1038/342420a0

Salters, V.J.M., Longhi, J., 1999. Trace element partitioning during the initial stages of melting beneath mid-ocean ridges. Earth Planet. Sci. Lett. 166, 15–30. doi:10.1016/S0012-821X(98)00271-4

Salters, V.J.M., Longhi, J.E., Bizimis, M., 2002. Near mantle solidus trace element partitioning at pressures up to 3.4 GPa. Geochemistry, Geophys. Geosystems 3, 1–23. doi:10.1029/2001GC000148

Sen, C., Dunn, T., 1994. Dehydration melting of a basaltic composition amphibolite at 1.5 and 2.0 GPa: implications for the origin of adakites. Contrib. to Mineral. Petrol. 117, 394–409. doi:10.1007/BF00307273

Shannon, R.D., 1976. Revised effective ionic radii and systematic studies of interatomic distances in halides and chalcogenides. Acta Crystallogr. Sect. A 32, 751–767. doi:10.1107/S0567739476001551

Shaw, D.M., 1970. Trace element fractionation during anatexis. Geochim. Cosmochim. Acta 34, 237–243. doi:10.1016/0016-7037(70)90009-8

Shen, Y., Forsyth, D.W., 1995. Geochemical constraints on initial and final depths of melting beneath mid-ocean ridges. J. Geophys. Res. Solid Earth 100, 2211–2237. doi:10.1029/94jb02768

Siret, D., Poulet, T., Regenauer-Lieb, K., Connolly, J.A.D., 2009. PreMDB, a thermodynamically consistent material database as a key to geodynamic modelling. Acta Geotech. 4, 107–115. doi:10.1007/s11440-008-0065-0

Sisson, 1991. Pyroxene-high silica rhyolite trace element partition coeficients measured by ion microprobe. Geochim. Cosmochim. Acta. 55. 1575-1585. doi:10.1016/0016-7037(91)90129-S

Smith, D.J., 2014. Clinopyroxene precursors to amphibole sponge in arc crust. Nat. Commun. 5, 4329. doi:10.1038/ncomms5329

Smyth, J.R., 1973. An Orthopyroxene Structure Up to 850°C. Am. Mineral. 58, 636–648.

Sobolev, A. V., Hofmann, A.W., Nikogosian, I.K., 2000. Recycled oceanic crust observed in ghost plagioclase within the source of Mauna Loa lavas. Nature 404, 986–990. doi:10.1038/35010098

Sorbadere, F., Médard, E., Laporte, D., Schiano, P., 2013. Experimental melting of hydrous peridotite-pyroxenite mixed sources: Constraints on the genesis of silica-undersaturated magmas beneath volcanic arcs. Earth Planet. Sci. Lett. 384, 42–56. doi:10.1016/j.epsl.2013.09.026

Stimpfl, M., Ganguly, J., Molin, G., 2005. Kinetics of Fe2+-Mg order-disorder in orthopyroxene: Experimental studies and applications to cooling rates of rocks. Contrib. to Mineral. Petrol. 150, 319–334. doi:10.1007/s00410-005-0016-9

Stimpfl, M., Ganguly, J., Molin, G., 1999. Fe2+-Mg order-disorder in orthopyroxene: Equilibrium fractionation between the octahedral sites and thermodynamic analysis. Contrib. to Mineral. Petrol. 136, 297–309. doi:10.1007/s004100050540

Sun, C., Liang, Y., 2013a. Distribution of REE and HFSE between low-Ca pyroxene and lunar picritic melts around multiple saturation points. Geochim. Cosmochim. Acta 119, 340–358. doi:10.1016/j.gca.2013.05.036

Sun, C., Liang, Y., 2013b. The importance of crystal chemistry on REE partitioning between mantle minerals (garnet, clinopyroxene, orthopyroxene, and olivine) and basaltic melts. Chem. Geol. 358, 23–36. doi:10.1016/j.chemgeo.2013.08.045

Sun, C., Liang, Y., 2012. Distribution of REE between clinopyroxene and basaltic melt along a mantle adiabat: Effects of major element composition, water, and temperature. Contrib. to Mineral. Petrol. 163, 807–823. doi:10.1007/s00410-011-0700-x

TEPLEY, F.J., DAVIDSON, J.P., TILLING, R.I., ARTH, J.G., 2000. Magma Mixing, Recharge and Eruption Histories Recorded in Plagioclase Phenocrysts from El Chichón Volcano, Mexico. J. Petrol. 41, 1397–1411. doi:10.1093/petrology/41.9.1397

Thompson, R.M., Downs, R.T., 2008. The crystal structure of diopside at pressure to 10 GPa. Am. Mineral. 93, 177–186. doi:10.2138/am.2008.2684

TIEPOLO, M., BOTTAZZI, P., FOLEY, S.F., OBERTI, R., VANNUCCI, R., ZANETTI, A., 2001. Fractionation of Nb and Ta from Zr and Hf at Mantle Depths: the Role of Titanian Pargasite and Kaersutite. J. Petrol. 42, 221–232. doi:10.1093/petrology/42.1.221

Tiepolo, M., Oberti, R., Zanetti, A., Vannucci, R., Foley, S.F., 2007. Trace-Element Partitioning Between Amphibole and Silicate Melt. Rev. Mineral. Geochemistry 67, 417–452. doi:10.2138/rmg.2007.67.11

Tiepolo, M., Vannucci, R., Bottazzi, P., Oberti, R., Zanetti, A., Foley, S., 2000. Partitioning of rare earth elements, Y, Th, U, and Pb between pargasite, kaersutite, and basanite to trachyte melts: Implications for percolated and veined mantle. Geochemistry, Geophys. Geosystems 1,. doi:10.1029/2000GC000064

Tiepolo, M., Vannucci, R., Oberti, R., Foley, S., Bottazzi, P., Zanetti, A., 2000. Nb and Ta incorporation and fractionation in titanian pargasite and kaersutite: crystal–chemical constraints and implications for natural systems. Earth Planet. Sci. Lett. 176, 185–201. doi:10.1016/S0012-821X(00)00004-2

Tiepolo, M., Zanetti, A., Oberti, R., 1999. Detection, crystal-chemical mechanisms and petrological implications of [6] Ti^ 4^+ partitioning in pargasite and kaersutite. Eur. J. Mineral. 11, 345–354.

Tirone, M., Sen, G., Morgan, J.P., 2012. Petrological geodynamic modeling of mid-ocean ridges. Phys. Earth Planet. Inter. 190, 51–70. doi:10.1016/j.pepi.2011.10.008

Tuff, J., Gibson, S.A., 2007. Trace-element partitioning between garnet, clinopyroxene and Fe-rich picritic melts at 3 to 7 GPa. Contrib. to Mineral. Petrol. 153, 369–387. doi:10.1007/s00410-006-0152-x

Turcotte , Donald L., and Gerald Schubert. Geodynamics. Cambridge Univ. Press, 2014.

Van Breemen, O., Hawkesworth, C.J., 1980. Sm-Nd isotopic study of garnet and their metamorphic host rocks. Earth Environ. Sci. Trans. R. Soc. Edinburgh 71, 97–102.

van Hunen, J., van den Berg, A.P., Vlaar, N.J., 2002. On the role of subducting oceanic plateaus in the development of shallow flat subduction. Tectonophysics 352, 317–333. doi:10.1016/S0040-1951(02)00263-9

van Keken, P.E., Hacker, B.R., Syracuse, E.M., Abers, G.A., 2011. Subduction factory: 4. Depth-dependent flux of H $_2$ O from subducting slabs worldwide. J. Geophys. Res. 116, B01401. doi:10.1029/2010JB007922

Van Westrenen, W., Allan, N.L., Blundy, J.D., Purton, J.A., Wood, B.J., 2000. Atomistic simulation of trace element incorporation into garnet-comparison with experimental garnet-melt partitioning data. Geochim. Cosmochim. Acta 64, 1629–1639. doi:10.1016/S0016-7037(00)00336-7

van Westrenen, W., Blundy, J.D., Wood, B.J., 2001. High field strength element/rare earth element fractionation during partial melting in the presence of garnet: Implications for identification of mantle heterogeneities. Geochemistry, Geophys. Geosystems 2, 7. doi:10.1029/2000GC000133

van Westrenen, W., Blundy, J.D., Wood, B.J., 1999. Crystal-chemical controls on trace element partitioning between garnet and anhydrous silicate melt. Am. Mineral. 84, 838-842. doi:10.2138/am-1999-5-618

Van Westrenen, W., Blundy, J.D., Wood, B.J., 2000. Effect of Fe2+ on garnet-melt trace element partitioning: Experiments in FCMAS and quantification of crystal-chemical controls in natural systems. Lithos 53, 189–201. doi:10.1016/S0024-4937(00)00024-4

van Westrenen, W., Draper, D.S., 2007. Quantifying garnet-melt trace element partitioning using lattice-strain theory: New crystal-chemical and thermodynamic constraints. Contrib. to Mineral. Petrol. 154, 717–730. doi:10.1007/s00410-007-0222-8

Van Westrenen, W., Wood, B., Blundy, J.D., 2001. A predictive thermodynamic model of garnet-melt trace element partitioning. Contrib. to Mineral. Petrol. 142, 219–234. doi:10.1007/s004100100285

Viete, D.R., Hermann, J., Lister, G.S., Stenhouse, I.R., 2011. The nature and origin of the Barrovian metamorphism, Scotland: diffusion length scales in garnet and inferred thermal time scales. J. Geol. Soc. London. 168, 115–132. doi:10.1144/0016-76492009-087

Walter, M.J., 1998. Melting of garnet peridotite and the origin of komatiite and depleted lithosphere. J. Petrol. 39, 29–60. doi:10.1093/petrology/39.1.29

Wang, L., Moon, N., Zhang, Y., Dunham, W.R., Essene, E.J., 2005. Fe-Mg order-disorder in orthopyroxene. Geochim. Cosmochim. Acta 69, 5777–5788. doi:10.1016/j.gca.2005.08.011

Warren, J.M., 2016. Global variations in abyssal peridotite compositions. Lithos. 248-251, 193-219. doi:10.1016/j.lithos.2015.12.023

Weatherley, S.M., Katz, R.F., 2012. Melting and channelized magmatic flow in chemically heterogeneous, upwelling mantle Theme: Geochemical Heterogeneities in Oceanic Island Basalt and Mid-ocean Ridge Basalt Sources: Implications for Melting Processes and Mantle Dynamics. Geochem. Geophys. Geosyst 13, 0–18. doi:10.1029/2011GC003989

Weill, D.F., Drake, M.J., 1973. Europium Anomaly in Plagioclase Feldspar: Experimental Results and Semiquantitative Model. Science . 180, 1059-1060.

White, J.C., 2003. Trace-element partitioning between alkali feldspar and peralkalic quartz trachyte to rhyolite magma. Part II: Empirical equations for calculating trace-element partition coefficients of large-ion lithophile, high field-strength, and rare-earth elements. Am. Mineral. 88, 330-337.

White William M. Geochemistry. Wiley-Blackwell, 2007.

Wilke, M., Behrens, H., 1999. The dependence of the partitioning of iron and europium between plagioclase and hydrous tonalitic melt on oxygen fugacity. Contrib. to Mineral. Petrol. 137, 102–114. doi:10.1007/s004100050585

Williams, M.L., Dumond, G., Mahan, K., Regan, S., Holland, M., 2014. Garnet-forming reactions in felsic orthogneiss: Implications for densification and strengthening of the lower continental crust, Earth and Planetary Science Letters. 405, 207-219. doi:10.1016/j.epsl.2014.08.030

Wolf, M.B., Wyllie, P.J., 1994. Dehydration-melting of amphibolite at 10 kbar: the effects of temperature and time. Contrib. to Mineral. Petrol. 115, 369–383. doi:10.1007/BF00320972

Wood, B.J., Banno, S., 1973. Garnet-orthopyroxene and orthopyroxene-clinopyroxene relationships in simple and complex systems. Contrib. to Mineral. Petrol. 42, 109–124. doi:10.1007/BF00371501

Wood, B.J., Blundy, J.D., 2013. Trace Element Partitioning: The Influences of Ionic Radius, Cation Charge, Pressure, and Temperature, in: Treatise on Geochemistry: Second Edition. Elsevier. 3, 421–448. doi:10.1016/B978-0-08-095975-7.00209-6

Wood, B.J., Blundy, J.D., 2001. The effect of cation charge on crystal–melt partitioning of trace elements. Earth Planet. Sci. Lett. 188, 59–71. doi:10.1016/S0012-821X(01)00294-1

Wood, B.J., Blundy, J.D., 1997. A predictive model for rare earth element partitioning between clinopyroxene and anhydrous silicate melt. Contrib. to Mineral. Petrol. 129, 166–181. doi:10.1007/s004100050330

Wood, B.J., Blundy, J.D., Robinson, J.A.C., 1999. The role of clinopyroxene in generating U-series disequilibrium during mantle melting. Geochim. Cosmochim. Acta 63, 1613–1620. doi:10.1016/S0016-7037(98)00302-0

Wood, B.J., Trigila, R., 2001. Experimental determination of aluminous clinopyroxene–melt partition coefficients for potassic liquids, with application to the evolution of the Roman province potassic magmas. Chem. Geol. 172, 213–223. doi:10.1016/S0009-2541(00)00259-X

Workman, R.K., Hart, S.R., 2005. Major and trace element composition of the depleted MORB mantle (DMM), Earth and Planetary Science Letters. 231, 53-72. doi:10.1016/j.epsl.2004.12.005

Yao, L., Sun, C., Liang, Y., 2012. A parameterized model for REE distribution between low-Ca pyroxene and basaltic melts with applications to REE partitioning in low-Ca pyroxene along a mantle adiabat and during pyroxenite-derived melt and peridotite interaction. Contrib. to Mineral. Petrol. 164, 261–280. doi:10.1007/s00410-012-0737-5

Zanetti, A., Tiepolo, M., Oberti, R., Vannucci, R., 2004. Trace-element partitioning in olivine: Modelling of a complete data set from a synthetic hydrous basanite melt. Lithos 75, 39–54. doi:10.1016/j.lithos.2003.12.022

Zellmer, G.F., Sparks, R.S.J., Hawkesworth, C.J., Wiedenbeck, M., 2003. Magma Emplacement and Remobilization Timescales Beneath Montserrat: Insights from Sr and Ba Zonation in Plagioclase Phenocrysts. J. Petrol. 44, 1413–1431. doi:10.1093/petrology/44.8.1413

Zimmer, M., Kröner, A., Jochum, K.P., Reischmann, T., Todt, W., 1995. The Gabal Gerf complex: A precambrian N-MORB ophiolite in the Nubian Shield, NE Africa. Chem. Geol. 123, 29–51. doi:10.1016/0009-2541(95)00018-H

Zou, H., Reid, M.R., 2001. Quantitative modeling of trace element fractionation during incongruent dynamic melting. Geochim. Cosmochim. Acta 65, 153–162. doi:10.1016/S0016-7037(00)00505-6

Appendix A: Investigation of trace element behaviour in a P-T-X space:

Application to the partial melting of a dry KLB-1 peridotite.

A composition of a dry KLB-1 peridotite (Jennings and Holland, 2015) is implemented in Perple_X to model the melt and residue composition of the partial melting of a peridotite. The primitive mantle trace element composition is used as the initial trace element composition (McDonough and Sun, 1995). This allows investigating the behaviour of trace element behaviour in MOR like conditions (P is from 0 to 5GPa, T is from 1000 to 1700°C).

Figure A.1 displays the modal composition of the partial melting of the KLB-1 peridotite. The assemblages are mainly composed of ol at HT/LP with minor spinel. Increasing pressure creates more complex mineral assemblages. The first mineral of interest to appear during increasing pressure is opx. At higher pressure, cpx and gt appear. The mineral pl is stable at LT and LP and is a minor phase with a modal composition that is not exceeding 10wt%.

Figure A.2 shows the evolution of the ratio La/Yb normalised to the initial concentration ($(\frac{La}{Yb})_N$). Since ol is the major mineral at equilibrium with the melt, the fractionation of La from Yb is really low at HT/LP with ratio values close to one. However, while gt and cpx appear, Yb favours the solid phase and fractionates from La. The fractionation of Yb from La can also be seen in the residual solid. The P-T domain whereby gt and cpx are stable displays a greater fractionation signature between La and Yb. The P-T domain whereby ol is the dominant phase shows a ratio approaching 0 that indicates that ol incorporate really small amount of these elements.

Figure A.3 shows the evolution of the ratio Lu/Hf normalised to the initial concentration ($(\frac{Lu}{Hf})_N$). As for the $(\frac{La}{Yb})_N$, the P-T domain whereby ol is the dominant phases impedes the melt to have a fractionation signature for the $(\frac{Lu}{Hf})_N$ ratio. Inversely, the P-T domain whereby gt and cpx are stable shows different signatures. At HP/HT, gt and cpx are the controlling phases on the ratio $(\frac{Lu}{Hf})_N$. This is marked in the partial melts by a relatively high value of $(\frac{Lu}{Hf})_N$ (e.g., 1.1 to 1.2) meaning that Hf is retained in the solid phase. Inversely, while gt is out at lower T and lower P, the signature changes with Lu being preferentially retained in the solid phase ($(\frac{Lu}{Hf})_N < 1$). In the solid, the more complex paragenesis (i.e., cpx+opx+gt+ol+melt) retained large proportion of Lu ($(\frac{Lu}{Hf})_N \gg 1$).
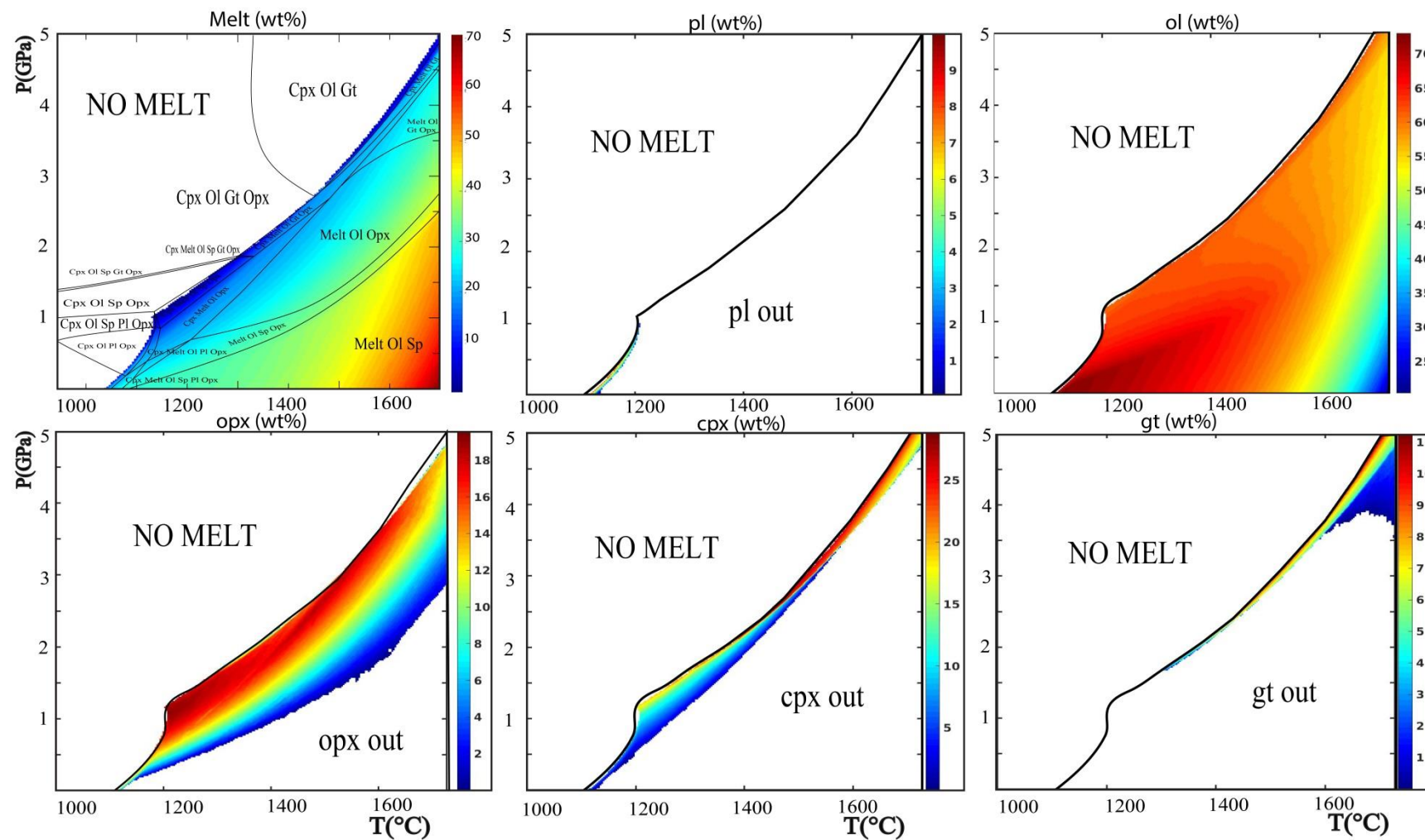
Figure A. 1: Computed modal composition of stable phases from Perple_X. Top left: Modal proportion of melt + topology of the entire system. Others: Modal fraction of stable phases. Colour bars indicate the modal composition of phases in wt%

Figure A. 2: *P-T grids of $(\frac{La}{Yb})_N$ behaviour in a peridotite system calculated from the coupling of TEPM and Perple_X. <u>Top:</u> $(\frac{La}{Yb})_N$ evolution in the melt (see text for explanations). <u>Bottom:</u> $(\frac{La}{Yb})_N$ evolution in the bulk solid (see text for explanations).*
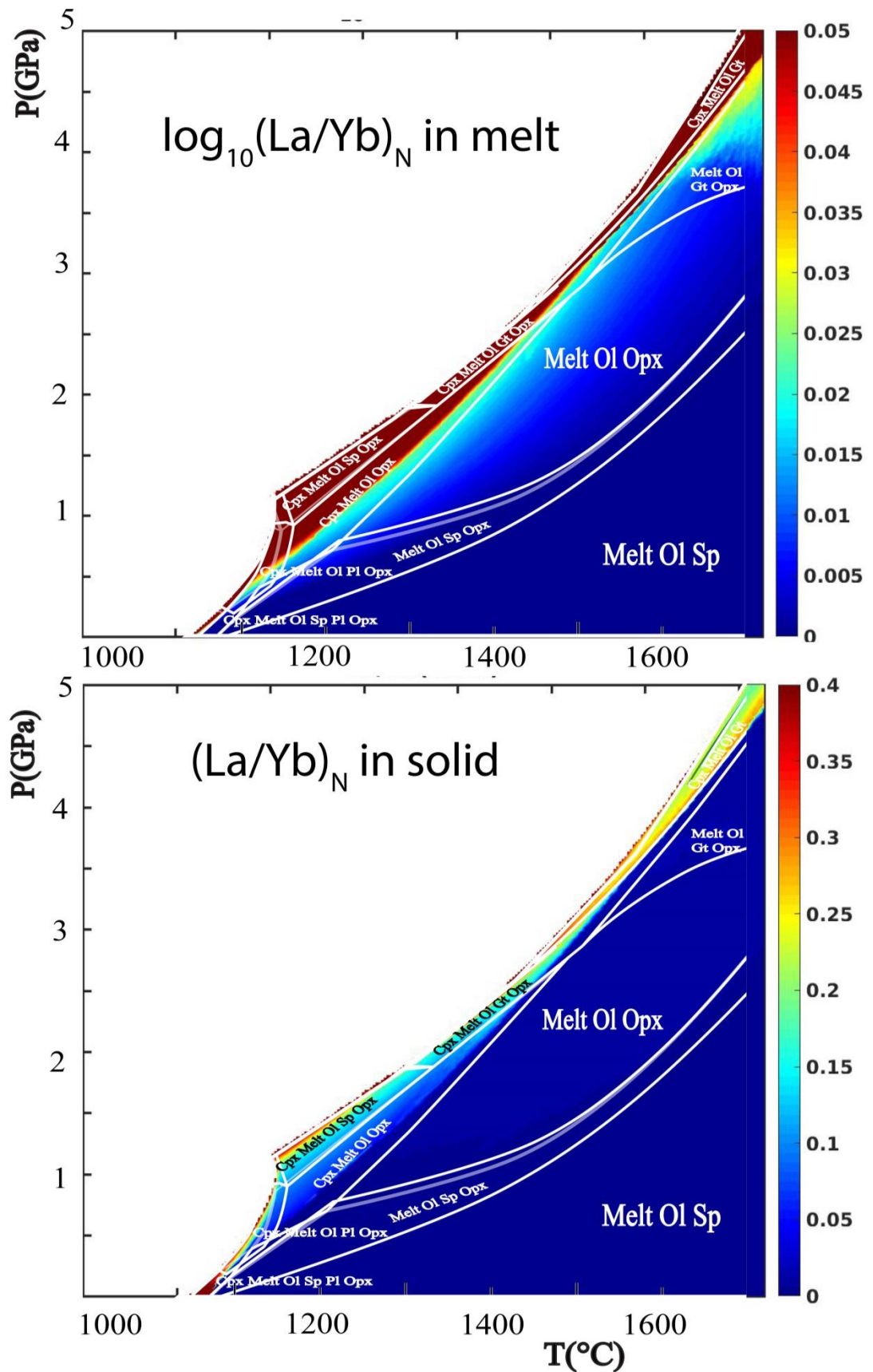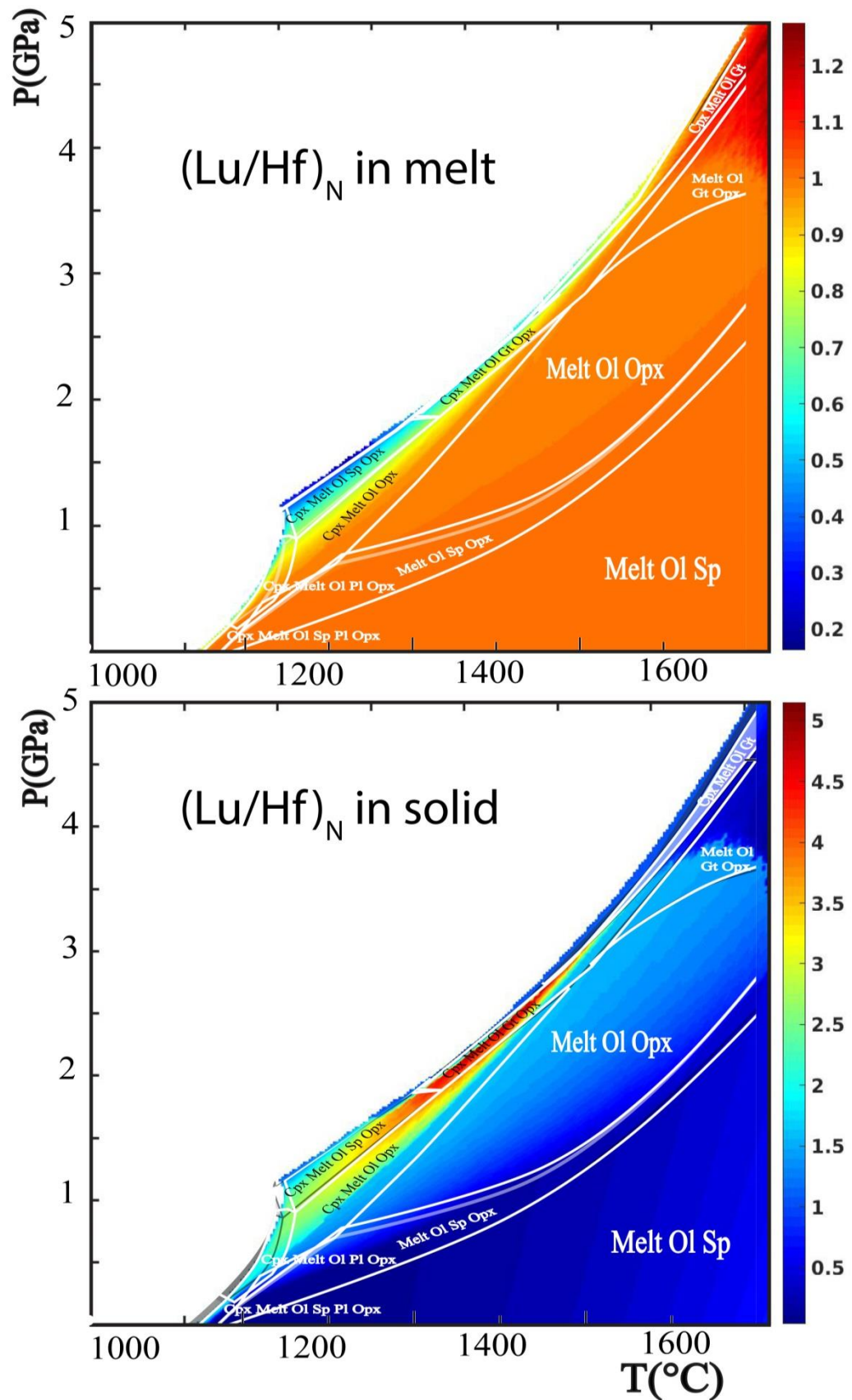
Figure A. 3: P-T grids of $(\frac{Lu}{Hf})_N$ behaviour in a peridotite system calculated from the coupling of TEPM and Perple_X. <u>Top:</u> $(\frac{Lu}{Hf})_N$ evolution in the melt (see text for explanations): <u>Bottom:</u> $(\frac{Lu}{Hf})_N$ evolution in the bulk solid (see text for explanations).

Appendix B: Example of input spreadsheet for TEPM: Major composition of experimental products of Qian and Hermann (2013)

Solid Phases	Experiment flags	T(K)	P(GPa)	SiO2	TiO2	Al2O3	FeOtot	MnO	MgO	CaO	Na2O	K2O	H2O	Total	Fraction	Name_exp
Melt	1	1273	1.00	67.67	1.27	15.30	2.79	0.05	1.39	4.17	3.13	1.94	13.80	99.66	13.00	C3081
Pl	1	1273	1.00	55.55	0.23	26.96	0.83	0.00	0.29	10.17	4.93	0.42	0.00	99.38	48.00	C3081
Cpx	1	1273	1.00	50.45	1.45	6.30	9.38	0.00	13.53	18.10	0.70	0.00	0.00	99.91	22.00	C3081
Opx	1	1273	1.00	52.48	0.57	4.76	17.38	0.00	23.00	1.82	0.36	0.00	0.00	100.37	17.00	C3081
Melt	2	1173	1.25	64.47	1.01	18.24	3.21	0.01	1.73	5.34	3.56	1.31	9.20	99.75	39.00	C3124
Amph	2	1173	1.25	41.51	3.49	15.52	11.36	0.00	12.61	10.17	2.33	0.00	0.00	96.99	20.00	C3124
Pl	2	1173	1.25	51.37	0.13	30.62	0.48	0.00	0.17	12.92	3.58	0.00	0.00	99.27	10.00	C3124
Cpx	2	1173	1.25	50.05	1.17	6.58	8.92	0.00	13.41	19.29	0.65	0.00	0.00	100.07	18.00	C3124
Gt	2	1173	1.25	39.46	1.38	21.37	18.52	0.00	11.61	7.43	0.07	0.00	0.00	99.84	11.00	C3124
Opx	2	1173	1.25	51.46	0.42	6.22	17.64	0.00	21.90	1.56	0.22	0.01	0.00	99.43	2.00	C3124
Melt	3	1073	1.50	71.87	0.32	16.00	1.75	0.02	0.59	4.56	2.56	1.12	10.20	99.86	27.00	C3171
Amph	3	1073	1.50	44.58	1.69	15.81	12.54	0.00	10.86	11.18	1.96	0.00	0.00	98.62	62.00	C3171
Gt	3	1073	1.50	37.68	0.93	21.03	22.03	0.00	6.12	9.96	0.17	0.00	0.00	97.92	2.00	C3171
Pl	3	1073	1.50	54.00	0.05	29.23	0.27	0.00	0.00	11.77	4.46	0.13	0.00	99.91	9.00	C3171
Melt	4	1173	1.00	66.72	0.79	16.72	3.29	0.03	1.23	4.44	3.07	1.63	13.00	99.66	27.00	C3179
Amph	4	1173	1.00	43.63	2.16	13.61	11.71	0.00	13.31	10.26	2.10	0.31	0.00	97.08	24.00	C3179
Cpx	4	1173	1.00	51.45	0.68	3.87	10.08	0.00	13.61	18.80	0.54	0.00	0.00	99.02	12.00	C3179
Opx	4	1173	1.00	50.94	0.36	4.05	20.67	0.00	21.05	1.68	0.21	0.00	0.00	98.96	10.00	C3179
Pl	4	1173	1.00	51.69	0.00	30.27	0.35	0.00	0.10	13.02	3.85	0.00	0.00	99.30	27.00	C3179
Melt	5	1073	1.00	70.14	0.22	14.81	1.17	0.00	0.57	3.87	3.64	1.28	20.80	100.02	23.00	C3161
Amph	5	1073	1.00	45.77	1.72	13.18	12.49	0.00	11.77	11.17	1.76	0.34	0.00	98.21	61.00	C3161
Pl	5	1073	1.00	50.23	0.09	31.62	0.82	0.00	0.24	14.51	2.34	0.14	0.00	100.13	16.00	C3161
Melt	6	1073	1.25	71.23	0.29	14.74	1.64	0.07	0.51	2.75	2.73	2.12	19.40	99.87	14.00	C3180
Amph	6	1073	1.25	43.20	1.92	13.86	14.80	0.00	11.04	10.06	1.86	0.32	0.00	97.04	64.00	C3180

Appendix B: Continued

Solid Phases	Experiment flags	T(K)	P(GPa)	SiO2	TiO2	Al2O3	FeOtot	MnO	MgO	CaO	Na2O	K2O	H2O	Total	Fraction	Name_exp
Pl	6	1073	1.25	55.32	0.00	27.73	0.25	0.00	0.08	10.06	5.52	0.16	0.00	99.15	22.00	C3180
Melt	7	1273	1.25	64.00	1.65	17.73	3.02	0.01	2.30	5.77	3.53	1.49	6.10	99.89	33.00	C3136
Cpx	7	1273	1.25	49.37	1.31	7.86	8.01	0.00	14.16	18.41	0.63	0.00	0.00	99.73	20.00	C3136
Opx	7	1273	1.25	50.89	0.54	6.83	16.59	0.00	23.28	1.70	0.23	0.00	0.00	100.06	17.00	C3136
Pl	7	1273	1.25	52.07	0.37	28.53	0.97	0.00	0.44	12.20	3.63	0.25	0.00	98.46	30.00	C3136
Melt	8	1173	1.35	63.71	0.95	18.48	3.77	0.02	1.94	6.38	2.75	0.96	8.30	99.68	44.00	C3221
Gt	8	1173	1.35	39.10	1.07	21.45	19.69	0.00	9.39	8.94	0.16	0.00	0.00	99.91	25.00	C3221
Amph	8	1173	1.35	43.49	1.84	14.42	11.54	0.00	13.33	10.76	2.27	0.37	0.00	98.01	18.00	C3221
Cpx	8	1173	1.35	50.92	0.80	5.96	7.56	0.00	13.03	20.19	0.69	0.00	0.00	99.14	13.00	C3221
Melt	9	1173	1.50	64.37	0.83	17.72	3.33	0.03	1.44	5.37	3.37	1.07	14.50	99.68	40.00	C3162
Gt	9	1173	1.50	39.06	1.25	21.10	19.79	0.00	10.20	8.68	0.18	0.00	0.00	100.47	30.00	C3162
Amph	9	1173	1.50	43.06	2.08	16.20	12.08	0.00	12.30	10.54	2.35	0.38	0.00	98.99	10.00	C3162
Cpx	9	1173	1.50	51.00	1.14	10.26	7.53	0.00	10.27	17.60	1.13	0.00	0.00	99.05	20.00	C3162
Melt	10	1273	1.50	64.59	1.15	17.61	3.36	0.02	1.53	5.33	4.02	1.26	3.40	99.01	44.00	C3052
Gt	10	1273	1.50	39.31	1.37	21.49	17.72	0.00	11.93	7.32	0.11	0.00	0.00	99.48	30.00	C3052
Cpx	10	1273	1.50	50.73	1.19	10.00	6.78	0.00	11.84	17.78	1.43	0.00	0.00	99.91	26.00	C3052
Melt	11	1273	1.50	59.89	1.47	18.91	4.87	0.01	3.20	7.03	3.24	0.93	3.40	99.67	59.00	C3217
Gt	11	1273	1.50	40.44	0.69	22.40	15.92	0.00	13.73	6.97	0.10	0.00	0.00	100.23	21.00	C3217
Cpx	11	1273	1.50	50.95	0.86	6.43	6.12	0.00	14.34	19.48	0.80	0.00	0.00	98.97	20.00	C3217
Melt	12	1323	1.50	57.86	1.44	19.88	5.36	0.03	3.55	7.79	3.10	0.85	2.90	99.94	69.00	C3123
Cpx	12	1323	1.50	48.58	1.12	11.22	6.35	0.00	13.13	18.08	0.85	0.00	0.00	99.33	24.00	C3123
Opx	12	1323	1.50	50.46	0.44	9.73	12.95	0.00	24.23	1.80	0.33	0.00	0.00	99.94	7.00	C3123

Appendix C: Prediction of trace element behaviour for Benchmark 1:

The following appendix provides complementary data for Benchmark 1. Figure C.1, C.4 and C.6 displays the composition of the major phases in Qian and Hermann (2013). Figure C.2, C.3, C.5 and C.7 display examples of the trace element partition coefficients predicted by TEPM. Since these figures are examples, only the partition coefficients predicted from the LSM are displayed. The other predicted partition coefficients from multiple regression analyses are available upon request.
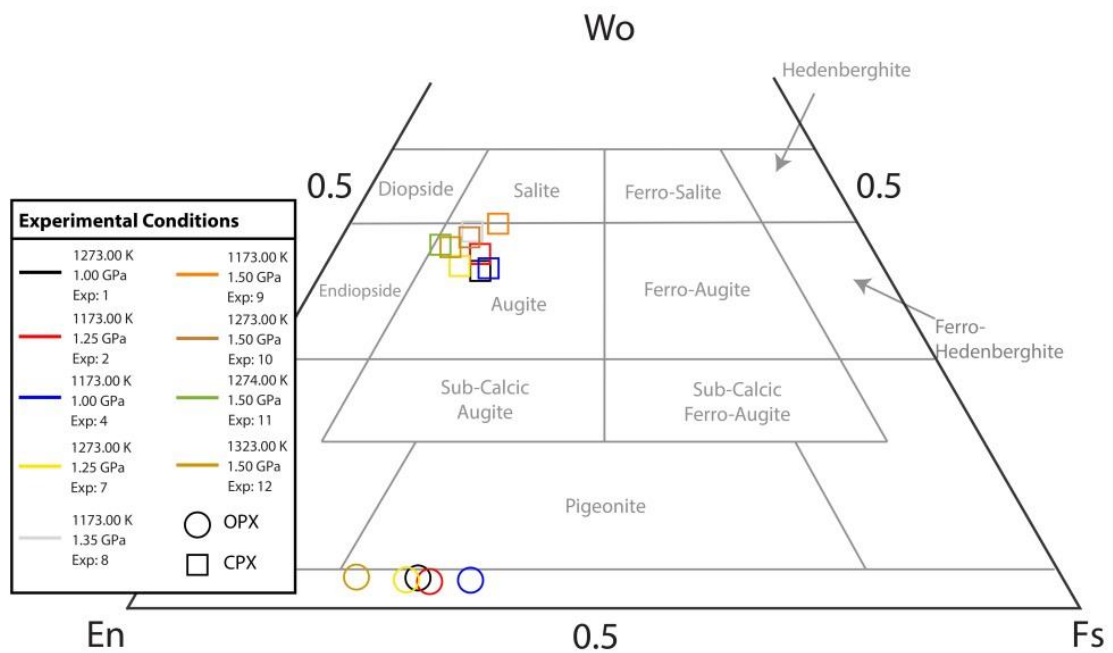
Figure C. 1: pyroxene range of composition within the experimental products of Qian and Hermann (2013)
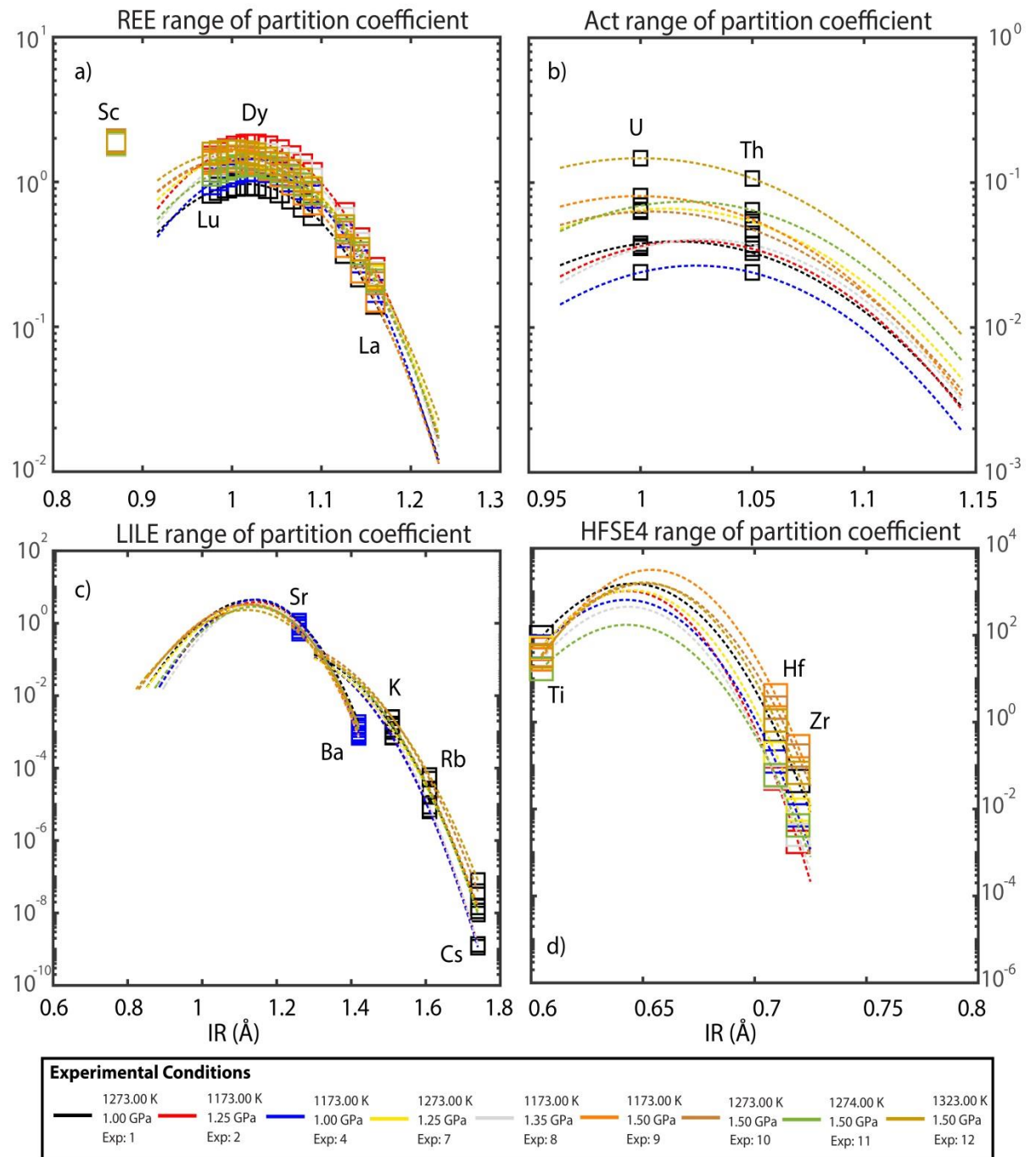
Figure C. 2: *Trace element behaviour in the experimental cpx of Qian and Hermann (2013)*
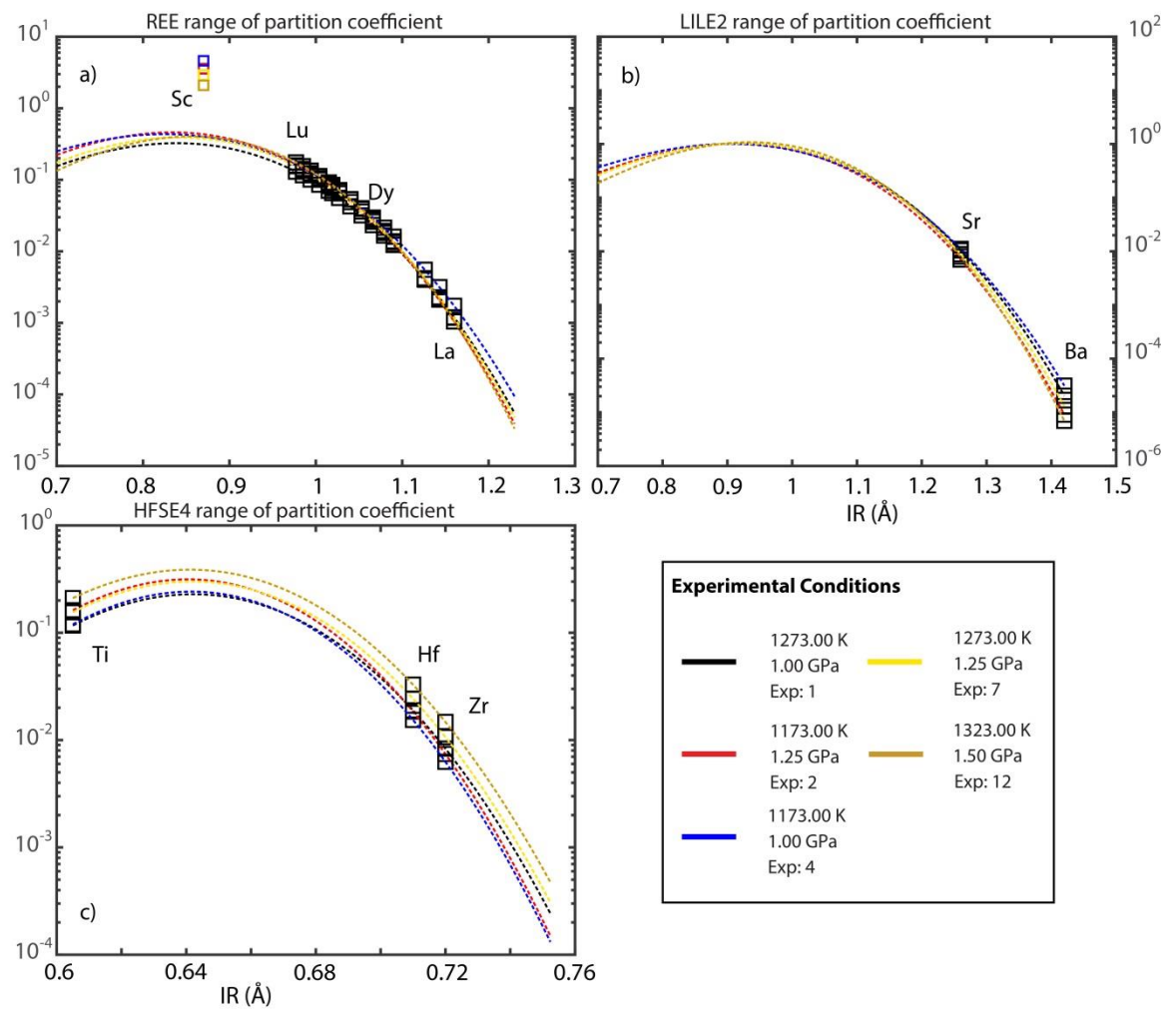
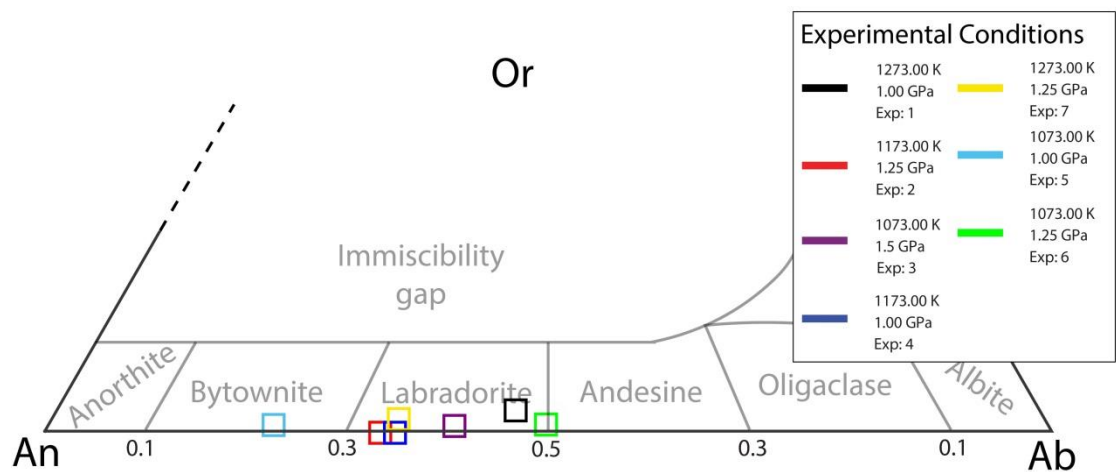*Figure C. 3: Trace element behaviour in the experimental opx of Qian and Hermann (2013)*

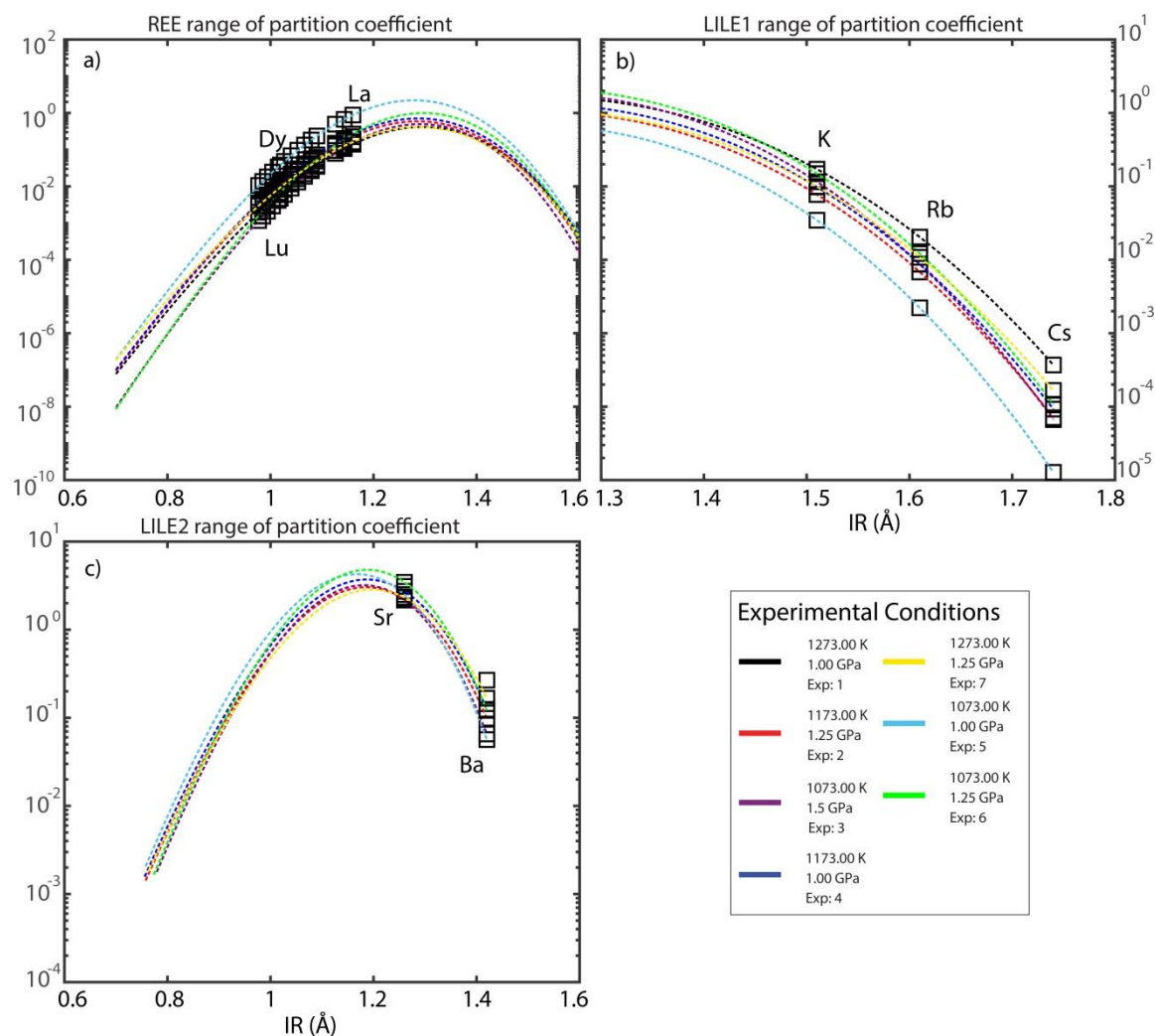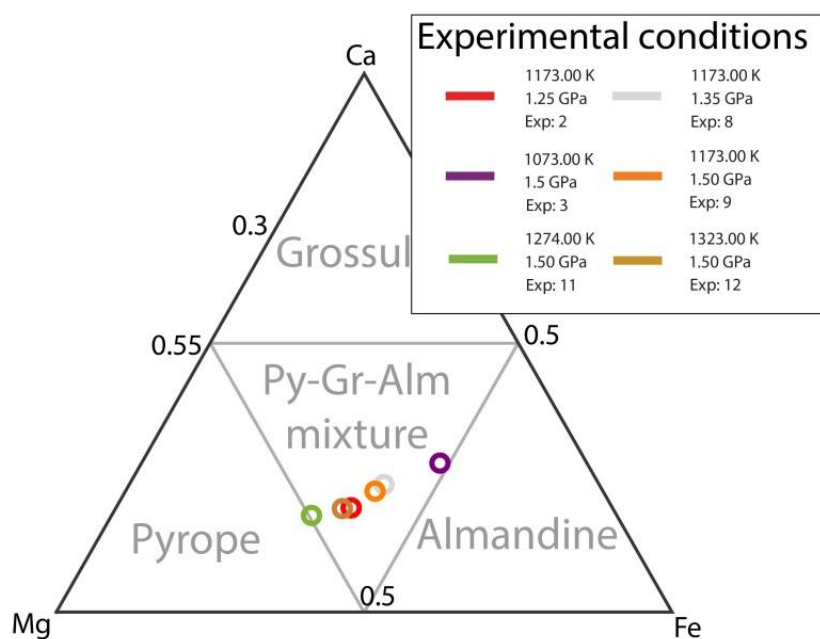**Figure C. 4:** *pl range of composition within the experimental products of Qian and Hermann (2013)*

Figure C. 5: *Trace element behaviour in the experimental pl of Qian and Hermann (2013)*

Figure C. 6: *gt range of composition within the experimental products of Qian and Hermann (2013)*
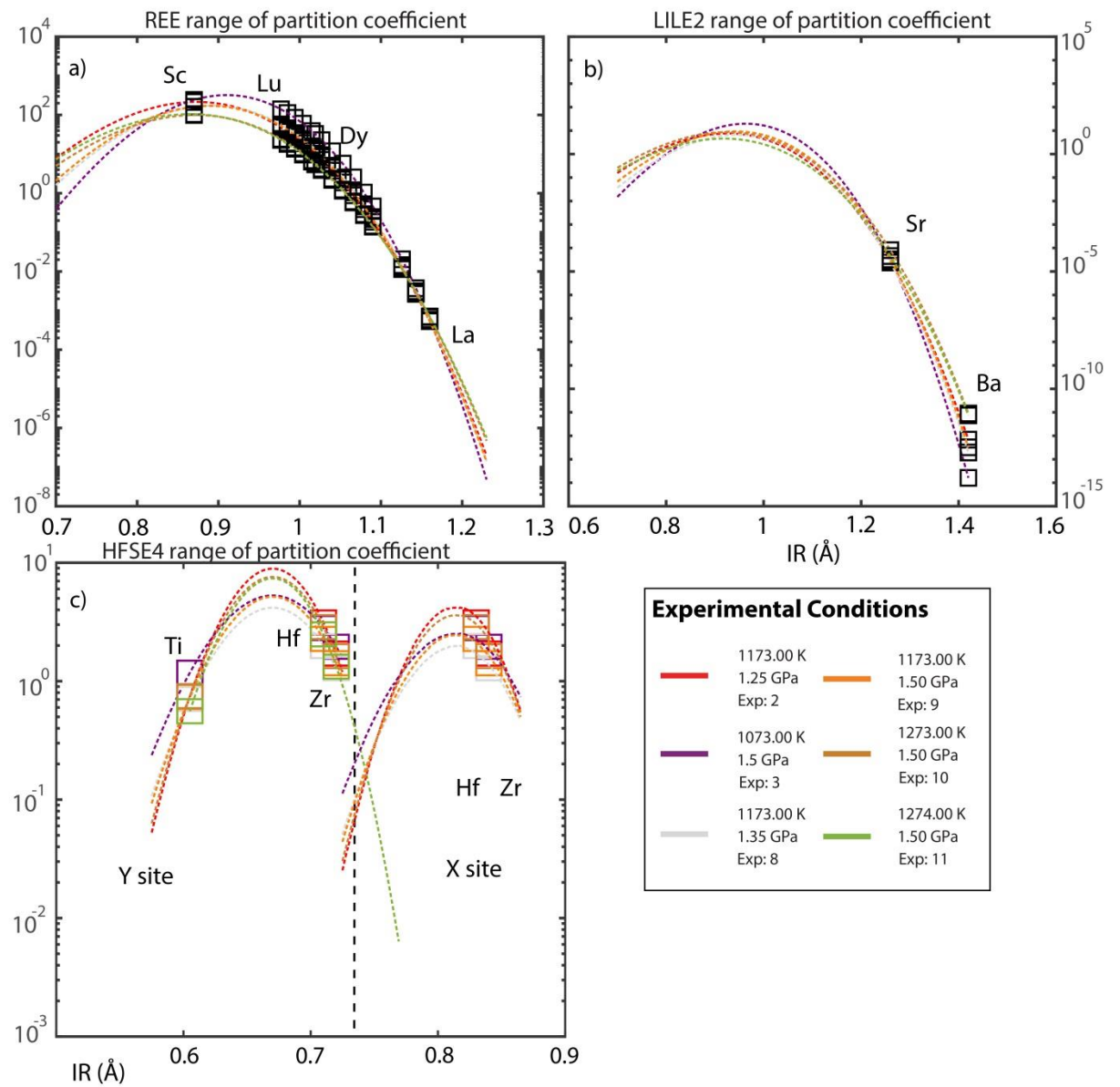
Figure C. 7: Trace element behaviour in the experimental gt of Qian and Hermann (2013)

Appendix D: Prediction of trace element behaviour for Benchmark 2

The following appendix provides complementary data for Benchmark 2. Table D.1 is the major and modal composition of the experimental products. Figure D.1 and D.3 display the composition of the major phases in Pertermann et al (2004). Figure D.2 and D.4 display examples of the trace element partition coefficients predicted by TEPM. Since these figures are examples, only the partition coefficients predicted from the LSM are displayed. The other predicted partition coefficients from multiple regression analyses are available upon request.

Table D. 1: Major element composition of experimental products of Pertermann et al (2004):

| Solid Phases	T(K)	P(Gpa)	SiO2	TiO2	Al2O3	FeOt	MnO	MgO	CaO	Na2O	K2O	H2O	Total	Fraction
Melt	1663	2.9	55.65	5.68	15.21	6.6	0.05	6.31	7.12	3.84	0.53	0	100.99	91
Melt	1613	3	54.28	5.62	17.89	5.33	0.07	2.88	8	3.8	0.53	0	98.4	85
Cpx	1663	2.9	50.19	2.34	12.51	6.4	0.08	11.16	12.74	3.17	0.01	0	98.6	8
Cpx	1613	3	47.71	2.5	19.87	4.79	0.05	7.13	14.18	3.51	0.01	0	99.75	10
Gt	1663	2.9	40.25	1.43	22.63	13.6	0.24	15.14	6.27	0.15	0	0	99.71	1
Gt	1613	3	39.16	1.67	22.25	14.61	0.22	12.77	8.49	0.16	0	0	99.33	4
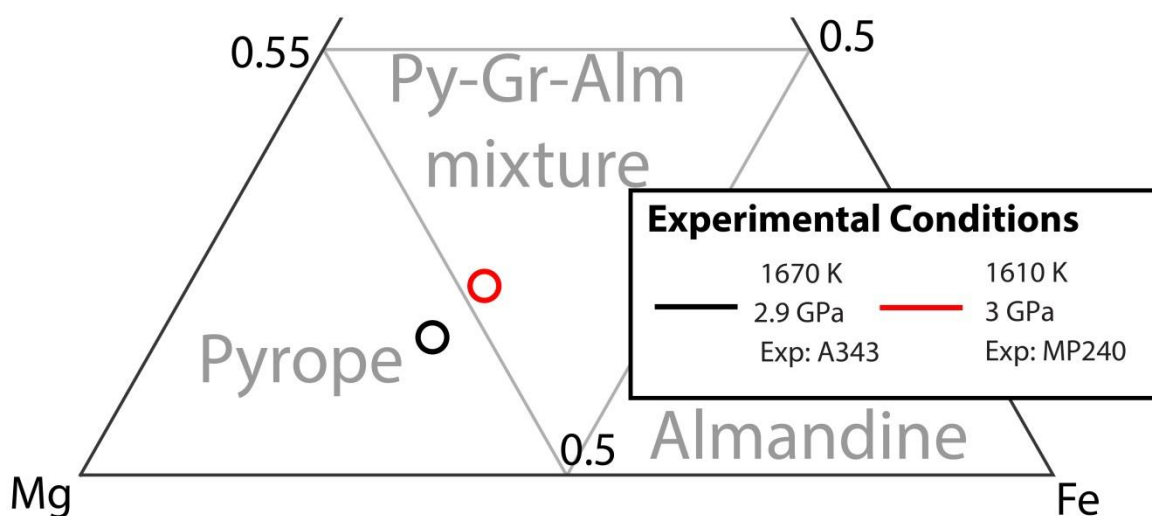
Figure D. 1: gt range of composition within the experiments of Pertermann et al (2004)
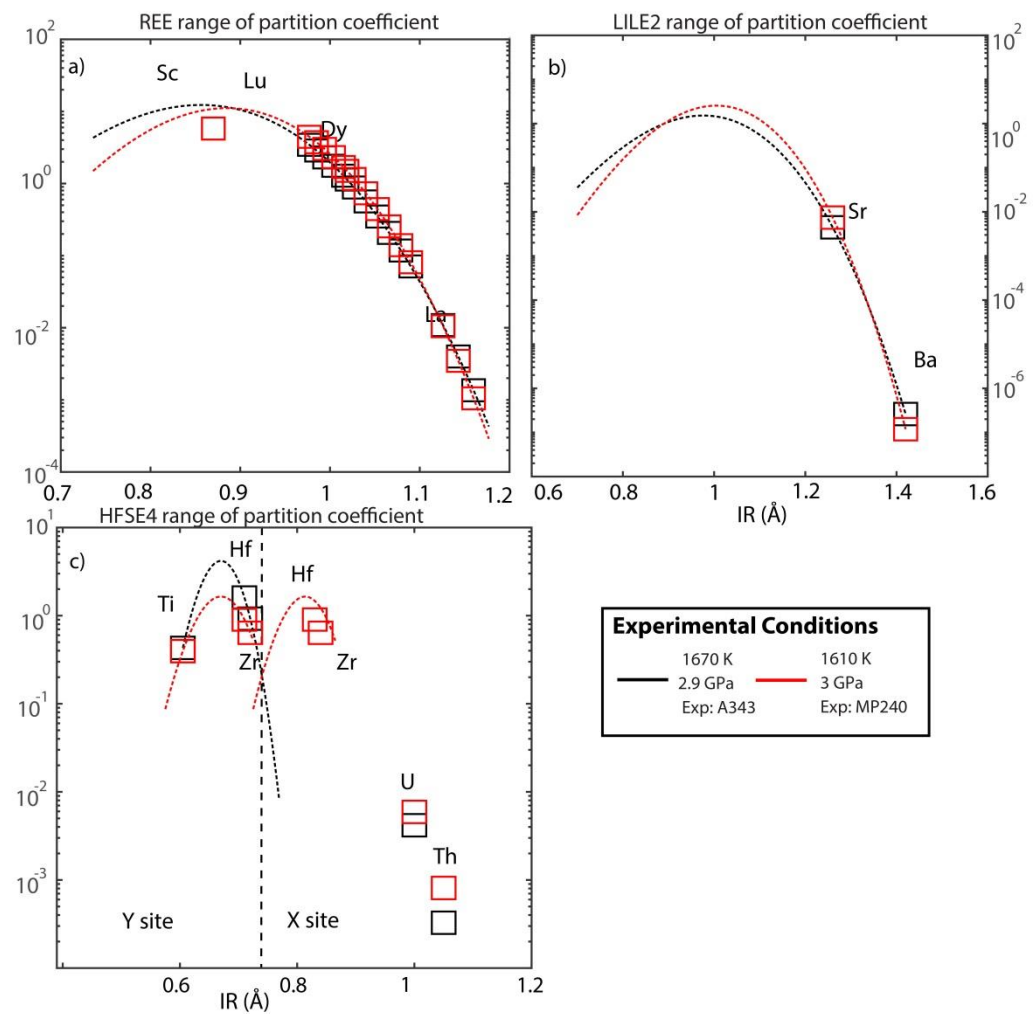
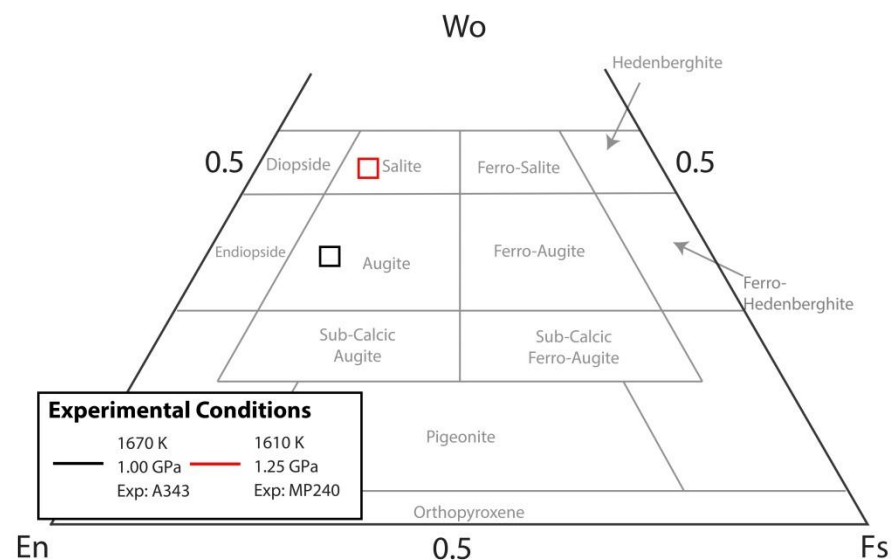***Figure D. 2:*** *Trace element behaviour in the experimental garnet of Pertermann et al (2004)*

Figure D. 3: *cpx range of composition within the experiments of Pertermann et al (2004)*
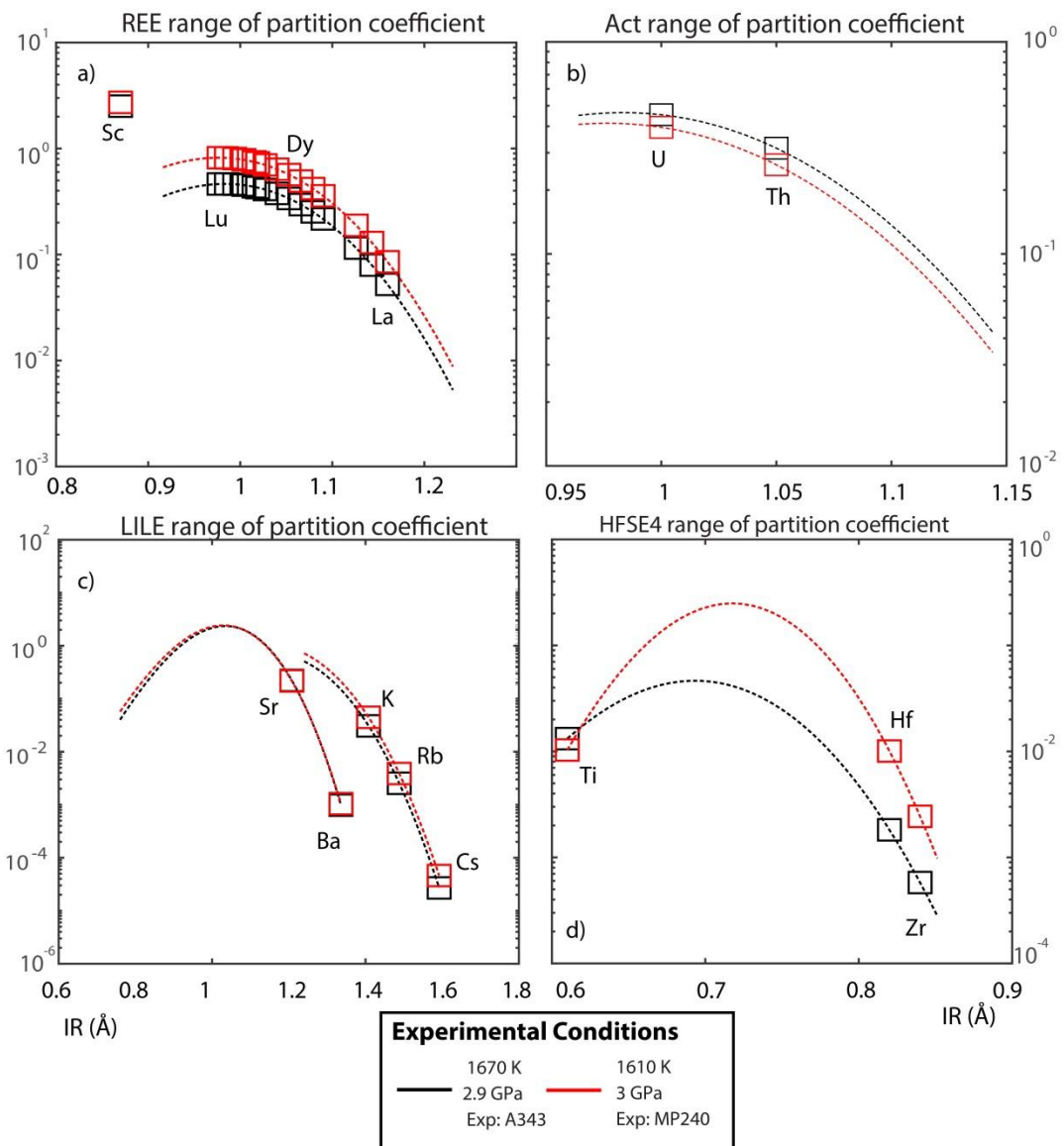
Figure D. 4: *Trace element behaviour in the experimental garnet of Pertermann et al (2004)*